

New Insights into Nucleation

Pressure Trace Measurements and the First Small Angle X-ray Scattering Experiments in a Supersonic Laval Nozzle

Inaugural - Dissertation

zur
Erlangung des Doktorgrades
der Mathematisch-Naturwissenschaftlichen Fakultät
der Universität zu Köln

vorgelegt von

David Ghosh
geboren in Neu Delhi, Indien

Köln 2007

Berichterstatter: Prof. Dr. Reinhard Strey, Universität zu Köln
PD Dr. Thomas Kraska, Universität zu Köln
Prof. Dr. Barbara E. Wyslouzil, The Ohio State University

Tag der mündlichen Prüfung: 06.11.2007

*Many years ago as a small child I stood on a brick wall,
the wall was huge compared to me,
and barbed wire was lying right in front of the wall.
It was a huge jump to make it across the barbed wire.
I was not alone on the wall,
there were other children from my neighborhood.
I was the youngest and therefore the smallest and weakest.
They all jumped from the wall across the barbed wire.
They dared me to jump.
I knew I wouldn't make it.
Yet I was not scared.
I jumped.
I didn't make it and landed in the barbed wire.
I didn't shed a single tear.
Today I carry the scares with pride.*

*Even today I take every hurdle, fear no fear,
and the saying "once bitten, twice shy" is left unheard.
I am growing, the wall is shrinking,
and so is the gap with the barbed wire.*

Abstract

Homogeneous nucleation rates of the n -alcohols and the n -alkanes have been determined by combining information from two sets of supersonic Laval nozzle expansion experiments under identical conditions. The nucleation rates $J = N / \Delta t_{J_{\max}}$ for the n -alcohols are in the range of $1 \cdot 10^{17} < J / \text{cm}^{-3} \text{s}^{-1} < 5 \cdot 10^{17}$ for the temperatures $207 \leq T / \text{K} \leq 249$, the nucleation rates for the n -alkanes lie in the range of $5 \cdot 10^{15} < J / \text{cm}^{-3} \text{s}^{-1} < 2 \cdot 10^{18}$ for the temperatures $143 \leq T / \text{K} \leq 215$. For the first time it is shown that the nucleation rate is not only a function of the supersaturation and temperature but clearly also sensitive to the expansion rate during supersonic nozzle expansion. A good agreement between the experimental results and those available in literature is found by applying *Hale's* scaling formalism [Hale, B., Phys. Rev. A **33**, 4256 (1986); Hale, B., Metall. Trans. A **23**, 1863 (1992)]. The scaling parameters from this work are also in good agreement with those shown by *Rusyniak et al.* [Rusyniak, M., M. S. El-Shall, J. Phys. Chem. B **105**, 11873 (2001)] and *Brus et al.* [Brus, D., V. Ždímal F. Stratmann, J. Chem Phys. **124**, 164306 (2006)]. In the first experiment static pressure measurements were conducted for the n -alkanes to determine the condensible partial pressure, temperature, supersaturation, characteristic time, and the expansion rate corresponding to the maximum nucleation rate. Characteristic times in the range of $13 \leq \Delta t_{J_{\max}} / \mu\text{s} \leq 34$ were found. In the second set of experiments, the first flow rate resolved Small Angle X-ray Scattering experiments are conducted to determine the particle number density for both substance classes. Particle number densities in the range of $1 \cdot 10^{12} < N / \text{cm}^{-3} < 5 \cdot 10^{12}$ and $1 \cdot 10^{11} < N / \text{cm}^{-3} < 3 \cdot 10^{12}$ for the n -alcohols and n -alkanes are found, respectively. Additionally, by analyzing the radially averaged scattering spectrum, information on the mean radius and the width of the size distribution of the aerosols is obtained. Mean radii for the n -alcohols in the range of $4 < \langle r \rangle / \text{nm} < 10$ and for the n -alkanes in the range of $5 < \langle r \rangle / \text{nm} < 31$ are found. The variations of the mean radius and the width of the size distribution with the flow rate and growth time, the systematic changes with increasing carbon chain length within one class of compounds, as well as the difference in behavior of these parameters between the n -alkanes and the n -alcohols deepen the knowledge of the growth behavior of nano-aerosols formed during supersonic nozzle experiments.

Kurzzusammenfassung

Die homogenen Keimbildungsraten von n -Alkoholen und n -Alkanen werden mit Hilfe zweier Sätze von Laval-Überschalldüsen-Experimenten unter identischen Bedingungen bestimmt. Die Keimbildungsraten $J = N / \Delta t_{J_{\max}}$ von n -Alkoholen sind in der Größenordnung von $1 \cdot 10^{17} < J / \text{cm}^{-3} \text{s}^{-1} < 5 \cdot 10^{17}$ für Temperaturen von $143 \leq T / \text{K} \leq 215$, die Keimbildungsraten von den n -Alkanen liegen in der Größenordnung von $5 \cdot 10^{15} < J / \text{cm}^{-3} \text{s}^{-1} < 2 \cdot 10^{18}$ für Temperaturen zwischen $207 \leq T / \text{K} \leq 249$. Zum ersten Mal konnte gezeigt werden, dass die Keimbildungsrate nicht nur eine Funktion von Übersättigung und Temperatur, sondern eindeutig auch abhängig von der Expansionsrate während der Überschalldüsen-Experimente ist. Eine gute Übereinstimmung zwischen den experimentellen Ergebnissen und denen aus der Literatur konnte durch Anwendung von *Hale's* Skalierungsformalismus [Hale, B., Phys. Rev. A **33**, 4256 (1986); Hale, B., Metall. Trans. A **23**, 1863 (1992)] gefunden werden. Die Skalierungsparameter dieser Arbeit stimmen ebenso gut mit denen von *Rusyniak et al.* [Rusyniak, M., M. S. El-Shall, J. Phys. Chem. B **105**, 11873 (2001)] und *Brus et al.* [Brus, D., V. Ždímal F. Stratmann, J. Chem Phys. **124**, 164306 (2006)] überein. Im ersten Satz von Experimenten werden statische Druckmessungen für die n -Alkane durchgeführt, um den kondensierbaren Partialdampfdruck, die Temperatur, die Übersättigung, die charakteristische Zeit und die Expansionsrate korrespondierend zu der maximalen Keimbildungsrate zu bestimmen. Charakteristische Zeiten in der Größenordnung von $13 \leq \Delta t_{J_{\max}} / \mu\text{s} \leq 34$ wurden ermittelt. Im zweiten Satz von Experimenten werden die ersten flussratenaufgelöste Kleinwinkel-Röntgenstreuexperimente durchgeführt, um die Teilchenzahldichte beider Substanzklassen zu bestimmen. Teilchenzahldichten in der Größenordnung von $1 \cdot 10^{12} < N / \text{cm}^{-3} < 5 \cdot 10^{12}$ und $1 \cdot 10^{11} < N / \text{cm}^{-3} < 3 \cdot 10^{12}$ werden für die n -Alkohole sowie die n -Alkane gefunden. Zusätzlich werden durch die Analyse des radial gemittelten Streuspektrums Informationen bezüglich des mittleren Radiuses und der Breitenverteilung der Aerosole erlangt. Mittlere Radien werden für die n -Alkohole in der Größenordnung von $4 < \langle r \rangle / \text{nm} < 10$ und für die n -Alkane in der Größenordnung von $5 < \langle r \rangle / \text{nm} < 31$ detektiert. Die Änderungen des mittleren Radiuses und der Breitenverteilung mit Flussrate und Wachstumszeit, das systematische Verhalten mit steigender Kohlenstoffkettenlänge innerhalb einer Substanzklasse sowie die Änderung im Verhalten dieser Parameter bei n -Alkanen und n -Alkoholen vertieft das Verständnis vom nano-Aerosolwachstumsverhalten während Überschalldüsen-Experimenten.

Table of Contents

List of Important Symbols	V
1 Introduction	9
1.1 Condensation and Nucleation	9
1.2 Task Description	15
2 Theory of Phase Transitions and Vapor to Liquid Nucleation	17
2.1 Phase Transitions	17
2.2 The <i>Ehrenfest</i> Classification of Phase Transitions	19
2.3 The Influence of the Temperature Dependent Heat Capacity on the Nucleation Temperature	23
2.4 Classical Nucleation Theory by <i>Becker</i> and <i>Döring</i>	26
3 Experimental Setup	33
3.1 Pressure Trace Measurements	33
3.2 Small Angle X-ray Scattering Experiments	38
4 Data Analysis	43
4.1 Pressure Trace Measurement	43
4.1.1 Effective Area Ratio	43
4.1.2 Rescaling for the Effective Throat Position for the Condensing Flow	44
4.1.3 Flow Profiles	45
4.1.4 Maximum Nucleation Conditions and Characteristic Time	48
4.2 Small Angle X-ray Scattering Experiments	49
4.2.1 X-ray Scattering Length Density	49
4.2.2 Scattering of <i>n</i> -Alkane Aerosols	49
4.2.3 Scattering of <i>n</i> -Alcohol Aerosols	50
5 Fundamental Basics during Supersonic Nozzle Expansion Experiments	53
5.1 Flow Profiles	53
5.2 The Flow Rate of the Condensible Species	56
5.3 The Stagnation Temperature	58
5.4 The Effect of Carrier Gas	59
6 Results and Discussion	63
6.1 Small Angle X-ray Scattering of <i>n</i> -Alcohol Droplets	63
6.2 The Effect of Temperature Dependent Heat Capacity on the Nucleation Temperature and the Critical Supersaturation	80
6.3 <i>n</i> -Alkane Pressure Trace Measurements	82
6.4 <i>n</i> -Alkane SAXS Measurements	90
7 Summary and Outlook	107
7.1 Summary	107
7.2 Outlook	109
Appendix	111
A.1 Chemicals	111
A.2 <i>n</i> -Alcohol Parameters	112

A.3	<i>n</i> -Alkane Parameters	114
A.4	<i>n</i> -Alcohol SAXS Results	116
A.5	<i>n</i> -Alcohol Nucleation Rates	120
A.6	<i>n</i> -Alkane Pressure Trace Measurements and Nucleation Rates	122
A.7	<i>n</i> -Alkane SAXS Measurements	126
	References	129
	Acknowledgements	135
	Erklärung (Statement)	137
	Lebenslauf (Curriculum vitae)	139

List of Important Symbols

Latin characters

a	local speed of sound
da	differential of local speed of sound
A	area
A^*	area of throat
A/A^*	area ratio
dA	differential of area
$d(A/A^*)/dx$	opening angle
B	parameter
c_p	molar constant pressure heat capacity of vapor
c_v	molar constant volume heat capacity of vapor
$c_p(T)$	molar constant pressure heat capacity of vapor as a function of temperature
$c_v(T)$	molar constant volume heat capacity of vapor as a function of temperature
c_{p0}	stagnation molar constant pressure heat capacity of vapor
$c_{p,Ar}$	molar constant pressure heat capacity of vapor argon
$c_{p,alkane}$	molar constant pressure heat capacity of vapor alkane
c_{pl}	constant pressure heat capacity of liquid
C_0	scaling parameter
d	differential
D	parameter
E	Energy
E_m	molar energy
dE_m	differential of molar energy
f	function
$g(x)$	condensate mass fraction profile
g_∞	initial condensate mass fraction
G_m	molar <i>Gibbs</i> energy / chemical potential
$G_{m,g}$	molar <i>Gibbs</i> energy of gas / chemical potential of gas
$G_{m,l}$	molar <i>Gibbs</i> energy of liquid / chemical potential of liquid
ΔG^*	<i>Gibbs</i> energy of critical cluster
h_{Planck}	Planck's quantum of action
h	specific heat
H_m	molar enthalpy
ΔH_{vap}	heat of vaporization
$I(q)$	scattering length intensity
I_{incoh}	incoherent scattering intensity
J	nucleation rate
J_{exp}	experimental nucleation rate
J_{theory}	theoretical nucleation rate
J_{exp}^{max}	maximum experimental nucleation rate
J_{theory}^{max}	maximum theoretical nucleation rate
k	<i>Boltzmann</i> constant
K	kinetic pre-exponential factor
$L(T)$	latent heat of condensate per unit mass
\dot{m}	molar flow rate
\dot{m}_v	mass flow rate of condensate

\dot{m}_i	mass flow rate of carrier gas
\dot{m}_i^0	stagnation mass flow rate of condensible
M	Mach number
dM	differential of Mach number
n^*	number of molecules in critical cluster
N	particle number density
N_A	Avogadro constant
N_l	number density of monomers
p	pressure
$p(x)$	pressure profile
p_0	stagnation pressure
p^*	pressure at throat
p_c	critical pressure
$p_{J_{\max}}$	partial pressure of condensible corresponding to maximum nucleation rate
p_{exp}	expansion pressure
$p^{\infty}(T)$	equilibrium vapor pressure
\dot{p}/p_0	expansion rate
dp	differential of pressure
$\hat{\partial}p$	infinitesimal differential of pressure
P	polydispersity index
q	scattering vector
Q	heat added per unit mass
$Q_{rev,m}$	reversible molar energy in form of heat
r^*	radius of the critical cluster
$\langle r \rangle$	mean radius
$\langle r^3 \rangle$	third moment of radius
r_{SL}	scattering length radii
R	universal gas constant
S	supersaturation (in separately noted cases: entropy)
S_0	stagnation supersaturation (in separately noted cases: stagnation entropy)
$S_{J_{\max}}$	supersaturation corresponding to maximum nucleation rate
S_m	molar entropy
S_{exp}	expansion entropy
t	time
dt	differential of time
t_{tof}	time of flight
t_D	thickness of diffuse interface
T	temperature
dT	differential of temperature
T_0	stagnation temperature
T_c	critical temperature
T_{exp}	expansion temperature
$\hat{\partial}T$	infinitesimal differential of temperature
$T_{J_{\max}}$	temperature corresponding to maximum nucleation rate
$\Delta t_{J_{\max}}$	characteristic time corresponding to maximum nucleation rate
$T(x)$	temperature profile
u	local velocity
du	differential of local velocity
$u(x)$	velocity profile

$\langle u \rangle$	mean velocity
$u(i)$	velocity at position i
u^*	velocity at throat
v_l	molecular volume
V_m	molar volume
$w(g)$	weight mass fraction of condensate
$w_0(g)$	stagnation weight mass fraction of condensate
W_m	molar work
x	position in the nozzle in respect to throat position
dx	differential of position in the nozzle
y_0	initial mole fraction of condensate
Z	atomic number

Greek characters

∂	infinitesimal differential
γ	isentropic expansion coefficient
γ_0	stagnation isentropic heat capacity
$\gamma(T)$	isentropic expansion coefficient as function of temperature
$d\gamma$	differential of isentropic expansion coefficient
$\partial\gamma$	infinitesimal differential of isentropic expansion coefficient
ϕ	volume fraction
κ_T	compressibility
λ	wave length
μ	molecular weight
μ_0	stagnation molecular weight
μ_v	molecular weight of condensate
μ_i	molecular weight of carrier gas
ρ	density of vapor
ρ_0	stagnation density of vapor
ρ^*	density of vapor at throat
$\rho(x)$	density profile of vapor
ρ_{NZ}	gas density at nucleation zone
ρ_{VV}	gas density at viewing volume
ρ_l	density of liquid
ρ_{SLD}	scattering length density
$\Delta\rho_{SLD}$	contrast factor
$\rho_{droplet}$	scattering length density of droplet
ρ_{gas}	scattering length density of carrier gas
σ	width of distribution function
σ_{ST}	surface tension
θ	scattering angle
Ω	surface entropy per molecule

1 Introduction

1.1 Condensation and Nucleation

The galaxy, the planet, and we ourselves consist of matter. Everyday we are exposed to different materials, e.g. water, cloth, metal, wood..., but also to different type of states of one material/substance, e.g. gaseous, liquid and solid. The different states of one material are in a dynamical equilibrium with each other, thus, liquids and gases constantly evaporate and condense. Despite the tremendous presence of materials / substances in their different states and our natural behavior to this exposure, it is up to date not fully understood how phase transitions function within the dynamics of this equilibrium.

Vapor phase condensation plays an essential role in many natural and industrial processes including cloud formation and the separation of water and hydrocarbons from natural gas. The first stage of condensation is nucleation, the formation of the initial microscopic fragments of the stable phase from the meta-stable mother phase. Further growth and aging build up the macroscopic phase (Figure 1.1). From these three phenomena, nucleation is the least well understood and hardest to predict, because the initial fragments are very small, meta-stable and short-lived.

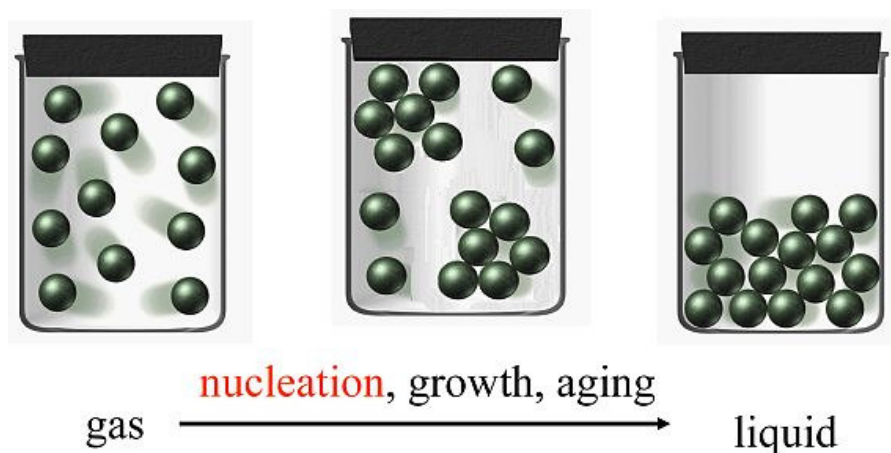


Figure 1.1: Schematic figure of the phase transition from gas to liquid.

It is important to distinguish between two types of nucleation. Homogeneous nucleation is nucleation in the absence of any foreign surfaces or particles, while heterogeneous nucleation occurs in the presence of foreign surfaces and particles. Even though most condensation processes in nature are initiated by heterogeneous nucleation, it is important to understand the much simpler homogeneous nucleation process first.

Even though there have been many theoretical approaches, such as the Classical Nucleation Theory (CNT) by *Becker* and *Döring*¹ or also more recent approaches like EMLD-DNT,² which try to describe homogeneous nucleation quantitatively, it is still not a trivial task to predict the nucleation rate correctly. Deviations of several orders of magnitude between theoretical predictions and experimentally determined nucleation rates are common. In some cases these deviations are attributed to the fact that the new phase is a supercooled liquid whose physical properties are uncertain. In other cases the problem is assumed to stem from theories that do not account for the complex intermolecular potentials of the molecules of experimental interest.

Whenever experimental results are compared to theoretical predictions it is evident that most theories fail to describe a set of experiments in a wide temperature range. For example, *Wölk* and *Strey*³ showed that CNT is able to predict the measured H₂O nucleation rates at 240 K accurately, however, shows a disparate temperature dependency. While the theory predicts too high rates for high temperatures, the isotherms lie too low at low temperatures. Such a disparate temperature trend has also been observed for other substances such as *n*-nonane⁴ and for the homologous series of *n*-alcohols starting from 1-methanol to 1-hexanol.⁵ Surprisingly, even for molecules like argon, where the intermolecular potentials are well known, discrepancies between theoretical and measured nucleation rates of 16 to 26 orders of magnitude have been observed.⁶ Additionally, a similar disparate temperature dependency is found.

Comparisons between theory and experiment are enhanced by measurements made over a wide range of nucleation rates, temperatures, and supersaturations. Figure 1.2 exhibits the range of nucleation rates for numerous experimental devices.⁷ For example, in the *dif-*

¹ Becker and Döring, 1935.

² Reguera and Reiss, 2004b; Reguera and Reiss, 2004a.

³ Wölk and Strey, 2001.

⁴ Wagner and Strey, 1984.

⁵ Strey, Wagner, and Schmeling, 1986; Biet, 1998; Iland *et al.*, 2004b.

⁶ Iland, 2004a.

⁷ For a review of nucleation experiments see Strey, Wagner, and Schmeling, 1986; Heist and He, 1994; Laaksonen, Talanquer, and Oxtoby, 1995.

*fusion cloud chamber*⁸ the fog accumulation of a liquid between two different tempered plates is investigated. In case of the *laminar diffusion cloud chamber*⁹ a vapor flows from a warm liquid filled tube into a cold tube in which condensation takes place. In *supersonic nozzles*¹⁰ and *wave tubes*¹¹ a gas mixture can be expanded. Here, the nucleation is detected by a deviation in the pressure profile or also by light scattering, respectively. These experimental apparatuses initially only detect the onset conditions, i.e. the conditions at which newly built droplets can already be detected. In case of the *supersonic nozzle Khan et al.*¹² have developed a method, by which the maximum nucleation conditions can be derived. The maximum nucleation conditions are not sensitive to the experimental detection method, and thus, not system specific. One of the key parameters of the nucleation phenomenon is the nucleation rate J , the number of clusters/aerosols formed per unit volume and time. With the *single piston expansion chamber* developed by Allard and Kassner,¹³ the nucleation rate can be directly measured by expanding a gas mixture and simply counting the particle number density. In the *nucleation pulse chamber*,¹⁴ the particle number density is determined by evaluating the *Mie*¹⁵ scattering signal, while the characteristic time, the time associated to the formation of the clusters/aerosols, is determined by analyzing the width of the expansion pulse. The ratio of both properties yields the nucleation rate J . The *shock tube*¹⁶ and the *pulse expansion wave tube*¹⁷ are built in a manner that the pressure wave itself is pulsed. This enables direct measurements of the nucleation rate J . However, since most experimental devices can access only a limited range of nucleation rates (< 3 – 5 orders of magnitude (Figure 1.2)), data from many different experimental setups must be combined to stringently test theoretical predictions. The existing discrepancies between theoretical predictions and experimental nucleation results, as well as between experimental results themselves, make it evident that further reliable data sets of nucleation experiments are indispensable.

⁸ Katz, 1970; Heist and Reiss, 1973; Hung, Krasnopoler, and Katz, 1989.

⁹ Anisimov *et al.*, 1998; Lihavainen and Viisanen, 2001a.

¹⁰ Wegener, 1966; Wyslouzil *et al.*, 1994.

¹¹ Peters and Paikert, 1989.

¹² Khan *et al.*, 2003.

¹³ Allard and Kassner, 1965.

¹⁴ Wagner and Strey, 1981; Strey, Wagner, and Viisanen, 1994.

¹⁵ Wagner, 1985.

¹⁶ Peters, 1982; Peters, 1983.

¹⁷ Looijmans and van Dongen, 1997.

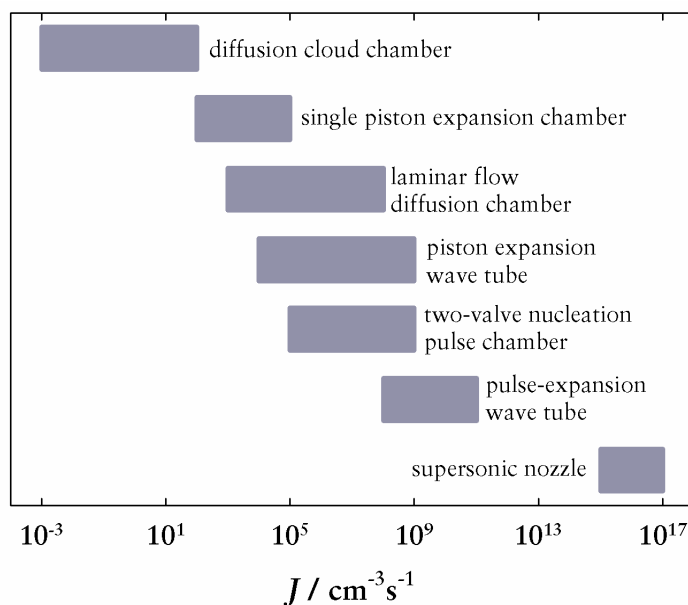


Figure 1.2: Different vapor-liquid nucleation experiments and their respective measuring window (details and references: see text).¹⁸

The *n*-alcohols and the *n*-alkanes form two classes of compounds that are accessible to most experimental devices, and they have the further advantage that, in most nucleation experiments, condensation occurs at temperatures far above the triple point where the physical properties are well known. In 1995 at the workshop of *Nucleation Experiments - State of the Art and Future Development* in Prague the nucleation community chose *n*-pentanol in helium as carrier gas at temperatures of 240 K, 250 K, and 260 K as the best compound with suitable temperatures for a series of individual experiments on homogeneous nucleation.¹⁹ The goal was to measure nucleation rates spanning a range of $J \sim 20 \text{ cm}^{-3} \text{ s}^{-1}$ orders of magnitude.

Since it is important for chemical engineering processes to understand and to be able to predict systematic trends for a homologous series of substances the investigation on *n*-pentanol has been extended by many groups and the nucleation properties for the homologous series of *n*-alcohols have been further investigated.²⁰ During an overseas research project from June – October 2003 in the Aerosol Laboratories of Prof. B. E. Wyslouzil at the Worcester Polytechnic Institute the nucleation behavior of

¹⁸ Figure according to Iland, 2004a.

¹⁹ Smolík and Wagner, 1996.

²⁰ Kacker and Heist, 1985; Strey, Wagner, and Schmeling, 1986; Viisanen and Strey, 1994; Strey, Viisanen, and Wagner, 1995; Hruby, Viisanen, and Strey, 1996; Luijten, Baas, and van Dongen, 1997; Viisanen, Wagner, and Strey, 1998; Zdimal and Smolik, 1998; Rudek *et al.*, 1999; Anisimov *et al.*, 2000; Graßmann and Peters, 2000; Lihavainen, Viisanen, and Kulmala, 2001b; Graßmann and Peters, 2002; Schmitt and Doster, 2002; Iland *et al.*, 2004b; Brus *et al.*, 2005; Brus, Zdimal, and Stratmann, 2006.

the n -alcohols ($C_iH_{2i+1}OH$, $i = 3 - 5$) was investigated by conducting pressure trace measurements in a *supersonic nozzle* apparatus. The results of these experiments are the temperature $T_{J_{\max}}$, condensible partial pressure $p_{J_{\max}}$, supersaturation $S_{J_{\max}}$, and characteristic time $\Delta t_{J_{\max}}$ corresponding to the maximum nucleation rate. Our promising results led to a publication where a detailed discussion of Figure 1.3 is given.²¹

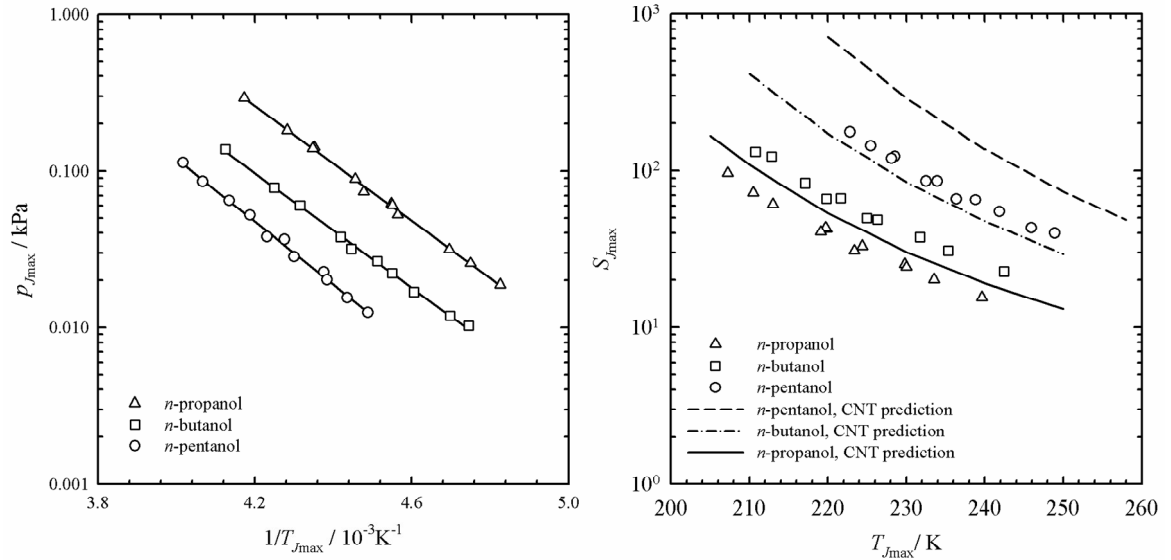


Figure 1.3: The pressure vs. the inverse temperature (left) and the supersaturation vs. the temperature (right) corresponding to the maximum nucleation rate. The solid, dashed dotted, and the dashed line in the right figure represent the predictions of Classical Nucleation Theory for $J = 5 \cdot 10^{16} \text{ cm}^{-3} \text{ s}^{-1}$ for n -propanol, n -butanol, and n -pentanol, respectively. A detailed discussion of these figures is given in *Gharibeh et al.*²¹

However, since the nucleation rate J is defined as

$$J(S, T) = \frac{N}{\Delta t_{J_{\max}}} \frac{\rho_{NZ}}{\rho_{VV}}, \quad (1.1)$$

and we had not measured the particle number density N in our supersonic nozzle, we could only estimate the nucleation rate J based on the values of N measured for H_2O , D_2O , and $H_2O - D_2O$ aerosols using Small Angle Neutron Scattering (SANS) in the identical nozzle.²² In equation (1.1) the ratio ρ_{NZ} / ρ_{VV} accounts for the change in gas density between the region where the particles were formed – the nucleation zone (NZ) – and the region where the particle number density was measured – the viewing volume (VV) – and is

²¹ Gharibeh *et al.*, 2005.

²² Kim *et al.*, 2004.

available from the pressure trace measurements. The motivation of this work is to characterize the missing variable, the particle number density N , via the first Small Angle X-ray Scattering experiments in a Laval supersonic nozzle, and thus to determine the nucleation rate J .

Another interesting substance class closely related to the n -alcohols are the n -alkanes. The n -alkanes play an essential role in the petrochemical industry during production, separation, transport, and handling of oil and natural gas. Natural gas containing mainly methane but also water and long chained hydrocarbons, like the n -alkanes, is found at high pressures beneath the earth surface in large cavities and other hollow rock formations. This gas mixture is passed through throttling valves and pipelines. Here, the gas undergoes a pressure drop. Consequently, nucleation of the long chained hydrocarbons takes place. This process can be used as a separation and purification process. Understanding the nucleation processes of long chained n -alkanes, for example in supersonic nozzles, can help engineers build more efficient pipeline systems with more sophisticated separation techniques. During the prior mentioned overseas research project, the first preliminary pressure trace measurements of n -nonane (Table 8.5 values with asterisk) were performed in a supersonic nozzle. These results promised interesting nucleation behavior. This motivated to extend the investigation on the nucleation and growth behavior of the homologous series of n -alkanes (C_iH_{2i+2} , $i = 7 - 10$).

1.2 Task Description

The task of the present work was to determine the homogeneous nucleation behavior of *n*-alcohols ($C_iH_{2i+1}OH$, $i = 3 - 5$) and *n*-alkanes (C_iH_{2i+2} , $i = 7 - 10$) during supersonic nozzle expansion. For this, three experimental projects were assigned.

First, the particle number density of the *n*-alcohol ($C_iH_{2i+1}OH$, $i = 3 - 5$) aerosols at flow rates similar to the preceding publication²³ had to be determined by Small Angle X-ray Scattering experiments. Combining the particle number densities with the characteristic time obtained from the earlier thermodynamic measurements²³ reveals information on the nucleation rate in supersonic nozzles. Additionally, the mean radius and the width of the size distribution function had to be determined from the SAXS measurements.

Second, by conducting pressure trace measurements of the *n*-alkanes (C_iH_{2i+2} , $i = 7 - 10$) information on the partial pressure, temperature, supersaturation, expansion rate, and the characteristic time corresponding to the maximum nucleation rate had to be obtained. Due to the higher complexity of the molecules, the temperature dependency of the constant pressure heat capacity had to be imbedded into the data analysis technique.

Third and final, the particle number density of the *n*-alkane (C_iH_{2i+2} , $i = 7 - 10$) aerosols had to be determined by Small Angle X-ray Scattering experiments. Again, combining the particle number densities with the characteristic time obtained from the pressure trace measurements yields information on the nucleation rate in supersonic nozzles. Additionally, the mean radius and the width of the size distribution function had to be determined.

²³ Gharibeh *et al.*, 2005.

2 Theory of Phase Transitions and Vapor to Liquid Nucleation

As this work deals with the gas to liquid phase transition, the condensation, a brief review of the theoretical basics needed to understand phase transition is presented in this chapter. After a short summary of the fundamentals for phase transitions²⁴ (Chapter 2.1), the *Ehrensfest*²⁴ classifications for phase inversions are summarized in chapter 2.2. Chapter 2.3 discusses the importance of treating the heat capacity for complex molecules in a temperature dependent manner during expansion experiments.²⁵ And finally, the Classical Nucleation Theory is given in chapter 2.4.²⁶

2.1 Phase Transitions²⁴

Before starting this chapter with well known thermodynamic facts, I would like to address the reader with a simple question: Why is equilibrium water at 1.00 atm and 373.14 K a liquid, however, at 1.00 atm and 373.16 K a vapor? Why does such a minor change in temperature make such a significant difference in structure and thermophysical properties?

The answer to this question is related to the fact that the free *Gibbs* energy of a system at equilibrium conditions always strives for a minimum. Figure 2.1 illustrates schematically the molar free *Gibbs* energy (chemical potential) of liquid and gaseous water as a function of temperature at 1.00 atm. If at a given temperature one phase has a lower chemical potential (solid line) than that of any other phase (dashed line), the system can lower its molar free *Gibbs* energy by relaxing into the thermodynamical stable phase. For example, at temperatures below 373.15 K the chemical potential of the liquid phase is lower than that of the vapor phase, thus, under equilibrium conditions we will find liquid water. If the temperature is increased above 373.15 K, also only slightly, the chemical potential of the vapor phase is lower than that of the liquid phase, and thus, if we allow the

²⁴ Wedler, 1997; Atkins, 1998; Mortimer, 2000.

²⁵ Witte and Tatum, 1994.

²⁶ Becker and Döring, 1935.

system to rest until equilibrium is reached we shall observe that a phase transition has taken place, i.e. we will find gaseous water.

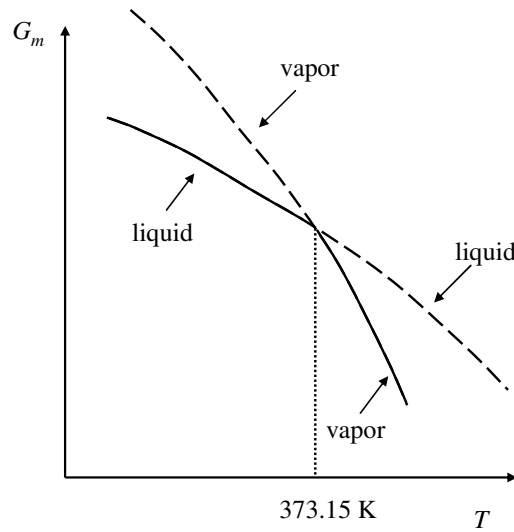


Figure 2.1: The molar *Gibbs* energy of water vs. the temperature near the liquid-vapor phase transition. The minimization of the molar *Gibbs* energy determines the stable phase (solid line) compared to the meta-stable state (dashed line) at a given temperature.

In order to fully understand Figure 2.1 it is important to review the following basic thermodynamic relationship

$$\left(\frac{\partial G_m}{\partial T}\right)_p = -S_m. \quad (2.1)$$

Here G_m is the molar free *Gibbs* energy, and S_m the molar entropy. The molar entropy of gaseous water is greater than that of liquid water, and thus, the slope of the gaseous curve in Figure 2.1 is more negative than the slope of the liquid. The intercept of the liquid and the gaseous curve is the equilibrium vapor pressure at 313.15 K. Above this temperature, the gaseous curve lies lower than the liquid curve, thus, the vapor is the stable phase (solid line), and the liquid is the meta-stable phase (dashed line). Below the normal boiling temperature, the liquid is stable (solid line), and the gaseous phase is meta-stable.

Figure 2.1 can also be understood by the following basic thermodynamic relationship

$$G_m = H_m - TS_m. \quad (2.2)$$

At a constant temperature, it is possible to minimize the molar free *Gibbs* energy G_m by either lowering the enthalpy H_m or by increasing S_m . The latter has a stronger influence at

high temperatures compared to low temperatures, as it is proportional to the temperature T . Thus, the phase of higher molar entropy is the stable phase at high temperatures. In contrast, the phase of lower molar enthalpy is the stable phase at low temperatures. The temperature of coexistence is the temperature at which these terms balance each other.

It is also possible to induce phase transitions by varying the pressure at a given temperature. Figure 2.2 illustrates the free *Gibbs* energy of liquid and gaseous water as a function of pressure at 373.15 K. The slope to fit the tangent of the curve is given by

$$\left(\frac{\partial G_m}{\partial p}\right)_T = V_m. \quad (2.3)$$

The molar volume V_m of the gas is greater than that of the liquid phase, and thus, the gaseous curve has a steeper slope than the liquid curve. At 373.15 K and pressures greater than 1.00 atm the liquid phase is stable and the gas is meta-stable. However, at 373.15 K and pressures less than 1.00 atm the gaseous phase is stable and the liquid is meta-stable.

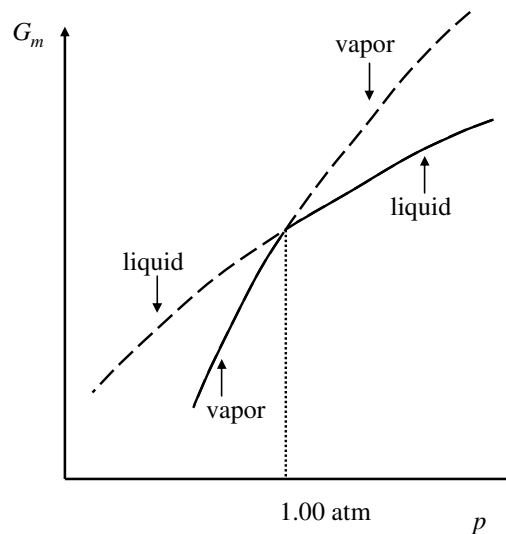


Figure 2.2: The molar *Gibbs* energy of water vs. the pressure near the liquid-vapor phase transition. The minimization of the *Gibbs* energy determines the stable phase (solid line) compared to the meta-stable state (dashed line) at a given pressure.

2.2 The *Ehrenfest* Classification of Phase Transitions²⁷

Many different types of phase transitions, such as vaporization, condensation, freezing,

²⁷ Wedler, 1997; Atkins, 1998; Mortimer, 2000.

melting, fusion, and less common examples of solid-solid, conducting-superconducting, and fluid-superfluid transitions can be found in nature and industrial processes. *Paul Ehrenfest* proposed a method to classify these different types of phase transitions into categories such as first-order phase transitions, second-order phase transitions, and λ -phase transitions.

During a first-order phase transition the *Gibbs* energy exhibits a cusp at the phase transition (Figure 2.3, top left and right). Further, at least one of the first derivatives of the molar *Gibbs* energy, i.e. the molar volume or the molar entropy, is discontinuous at the phase transition (Figure 2.3, center left and right). Usually both qualities are discontinuous. There are some few exceptions, such as the transition between ice IV and ice VII, where only one of the first derivatives of the molar *Gibbs* energy will be discontinuous. Furthermore, due to the discontinuity of the molar volume or the molar entropy, the second derivatives of the *Gibbs* energy,

$$\left(\frac{\partial^2 G_m}{\partial T^2}\right)_p = -\left(\frac{\partial S_m}{\partial T}\right)_p = -\frac{c_p}{T}, \quad (2.4)$$

$$\left(\frac{\partial^2 G_m}{\partial p^2}\right)_T = -\left(\frac{\partial V_m}{\partial p}\right)_T = -V_m \kappa_T, \quad (2.5)$$

the heat capacity or the compressibility, must show a singularity. Figure 2.3, bottom left and right exhibits the constant pressure heat capacity as a function of temperature and the compressibility as a function of pressure in the vicinity of the phase transition. The infinite value of the heat capacity during a first-order phase transition corresponds to the fact that a finite amount of heat produces an infinitesimal change in temperature as one phase is converted into the other phase. The physical reason is that heating drives the phase transition rather than raising the temperature of the substance, e.g. boiling water stays at the same temperature even though heat is being supplied. The infinite value of the compressibility corresponds to the fact that a finite volume change occurs as one phase is converted into the other while the pressure only changes infinitesimal. All common phase transitions such as vaporization, condensation, freezing, and melting are first-order phase transitions. These first-order phase transitions are often initiated by nucleation. Density fluctuations in the mother phase furnish microscopic small clusters of the new phase. Once these clusters exceed a certain critical size further growth and aging build the new macroscopic phase.

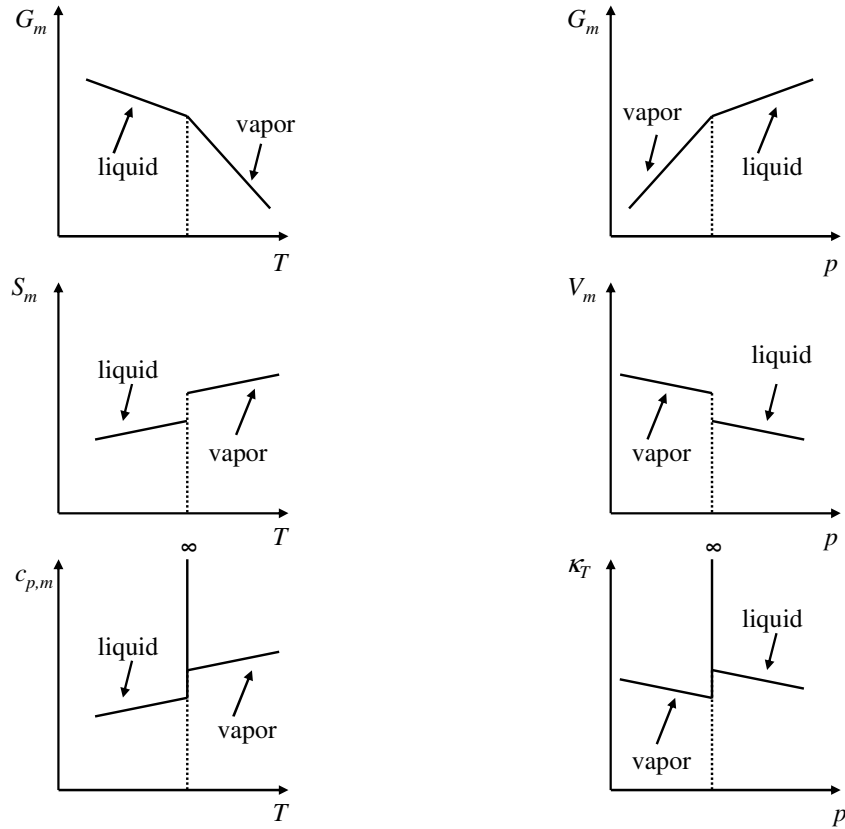


Figure 2.3: The changes in physical properties during first-order phase transitions.

During second-order phase transitions both of the first derivatives of the molar *Gibbs* energy are continuous, however, at least one of the second derivatives is discontinuous, but does not show a singularity. A continuous slope of the molar *Gibbs* energy on either side of the phase transition implies that the volume, entropy, and hence the enthalpy do not change during the phase transition (Figure 2.4). Second-order phase transitions are not common. An example is the conducting-superconducting transition in metals at low temperatures.

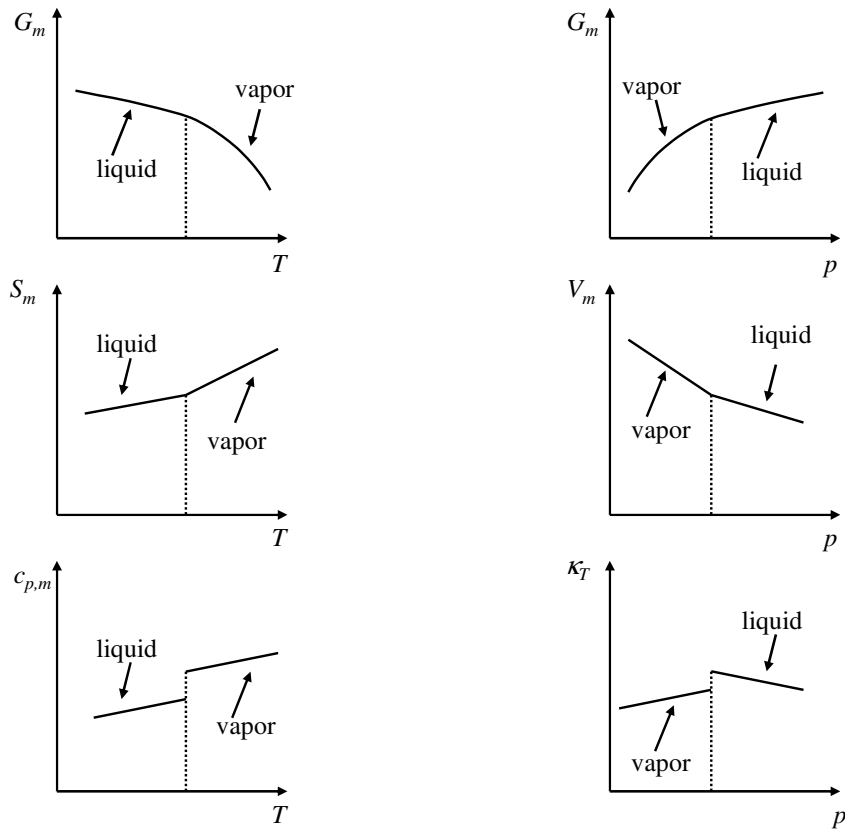


Figure 2.4: The changes in physical properties during second-order phase transitions.

A λ -phase transition is a transition that is not a first-order phase transition, yet, the heat capacity becomes infinite at the phase transition. Typically during λ -phase transitions the heat capacity rises smoothly towards infinity well before the transition instead of rising abruptly at the phase transition as in first-order phase transitions. Figure 2.5 exhibits the shape of the heat capacity curve as a function of the temperature. The term λ -phase transition is due to the resemblance of the behavior of the temperature dependent heat capacity with the Greek letter λ . An example of a λ -phase transition includes order-disorder phase transitions in solid metal alloys, e.g. β -brass, the onset of ferromagnetism, and the fluid-superfluid transition of helium.

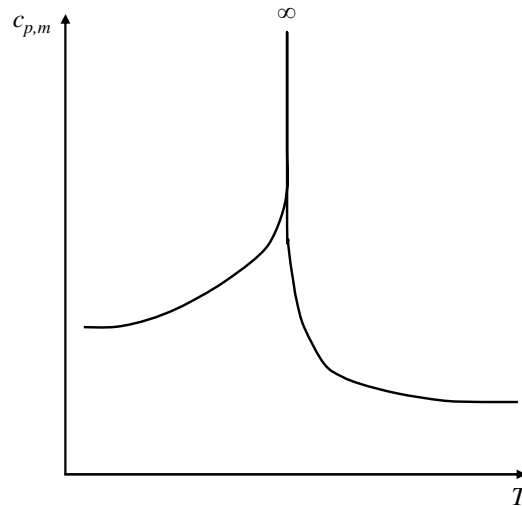


Figure 2.5: The behavior of the constant pressure heat capacity as a function of the temperature during λ -phase transitions.

2.3 The Influence of the Temperature Dependent Heat Capacity on the Nucleation Temperature²⁸

Phase transitions are induced by varying at least one of the field variables, i.e. pressure or temperature in such a manner that the state of the substance varies from the former stable state into a meta-stable state. This meta-stable state then relaxes into an under the new conditions stable state. This work examines the gas to liquid phase transition, the condensation. In this field of research it is not unusual to perform an expansion of a gas, as also conducted in this work, by which rapid cooling is achieved. The decrease of pressure is accompanied by a decrease in temperature. In the following the influence of the temperature dependency of the heat capacity for a gas mixture consisting of a condensible species (n -alkane, $c_p(T)$) and a carrier gas (argon; $c_p = \text{const}$) is investigated on the compressible flow relations.

If the constant pressure heat capacity for the investigated n -alkane is given by

$$c_{p,alkane} = D_1 + D_2T + D_3T^2, \quad (2.6)$$

the constant pressure heat capacity of the carrier gas by

$$c_{p,Ar} = B, \quad (2.7)$$

and if the n -alkane–argon mixture contains an initial mole fraction y_0 of the n -alkane, then

²⁸ Witte and Tatum, 1994.

the total heat capacity of the mixture is

$$c_p = y_0(D_1 + D_2T + D_3T^2) + (1 - y_0)B. \quad (2.8)$$

The first law of thermodynamics

$$\delta Q_{rev,m} + \delta W_m = dE_m \quad (2.9)$$

and the definition of entropy

$$\delta Q_{rev,m} = TdS_m \quad (2.10)$$

along with the thermodynamic relation

$$\delta W_m = -pdV_m \quad (2.11)$$

yields

$$TdS_m = dE_m + pdV_m. \quad (2.12)$$

Here $Q_{rev,m}$ is the reversible molar energy transferred to a system in form of heat, W_m is the molar work done on a system, and dE_m is the resulting change in the molar energy. The molar entropy is given by S_m , and $-pdV_m$ is the expansion work. The definition of molar enthalpy H_m is

$$H_m = E_m + pV_m. \quad (2.13)$$

The total differential of the molar enthalpy gives

$$dH_m = dE_m + pdV_m + V_m dp. \quad (2.14)$$

Combining equation (2.12) and equation (2.14) yields

$$TdS_m = dH_m - V_m dp. \quad (2.15)$$

For a thermally perfect gas the relation

$$dH_m = c_p dT \quad (2.16)$$

is valid. Here c_p is the constant pressure heat capacity. The substitution of equation (2.16) into equation (2.15) and the definition of the specific volume $\rho = 1 / v$ results in

$$dS_m = c_p \frac{dT}{T} - \frac{1}{\rho} \frac{dp}{T}. \quad (2.17)$$

Substituting the equation of state $p = \rho RT$ yields

$$dS_m = c_p \frac{dT}{T} - R \frac{dp}{p}. \quad (2.18)$$

Integrating equation (2.18) along the pathway of Figure 2.6 gives

$$\int_{S_0}^{S_{\text{exp}}} dS_m = \int_{T_0}^{T_{\text{exp}}} \frac{c_p}{T} dT + \int_{p_0}^{p_{\text{exp}}} -\frac{R}{p} dp \quad (2.19)$$

$$S_{\text{exp}} - S_0 = \int_{T_0}^{T_{\text{exp}}} \frac{c_p}{T} dT - R \ln\left(\frac{p_{\text{exp}}}{p_0}\right).$$

For the isentropic path from the stagnation state (subfix 0) to the final state of expansion (subfix exp.) $S_0 - S_{\text{exp}} = 0$ is valid and thus

$$0 = \int_{T_0}^{T_{\text{exp}}} \frac{c_p}{T} dT - R \ln\left(\frac{p_{\text{exp}}}{p_0}\right). \quad (2.20)$$

The analytical expression for this equation with a temperature dependent heat capacity according to equation (2.8) is given by

$$0 = y_0 D_1 \ln\left(\frac{T_{\text{exp}}}{T_0}\right) + y_0 D_2 (T_{\text{exp}} - T_0) + \frac{y_0 D_3}{2} (T_{\text{exp}}^2 - T_0^2) + (1 - y_0) B \ln\left(\frac{T_{\text{exp}}}{T_0}\right) - R \ln\left(\frac{p_{\text{exp}}}{p_0}\right). \quad (2.21)$$

To solve this equation for the coefficient T_{exp} a numerical method, e.g. root bracketing, or a mathematical program, e.g. Wolfram Mathematica[®] can be used.

The approximation $c_p = \text{const.}$ yields the following

$$0 = c_p \int_{T_0}^{T_{\text{exp}}} \frac{1}{T} dT - R \ln\left(\frac{p_{\text{exp}}}{p_0}\right)$$

$$0 = c_p \ln\left(\frac{T_{\text{exp}}}{T_0}\right) - R \ln\left(\frac{p_{\text{exp}}}{p_0}\right) \quad (2.22)$$

$$R \ln\left(\frac{p_{\text{exp}}}{p_0}\right) = c_p \ln\left(\frac{T_{\text{exp}}}{T_0}\right)$$

$$\frac{T_{\text{exp}}}{T_0} = \frac{p_{\text{exp}}}{p_0}^{R/c_p}.$$

The coefficient R/c_p can be rewritten by

$$\gamma = \frac{c_p}{c_v} = \frac{c_p}{c_p - R}$$

$$\begin{aligned} c_p \gamma - c_p &= R\gamma \\ c_p (\gamma - 1) &= R\gamma \end{aligned} \tag{2.23}$$

$$\begin{aligned} c_p &= \frac{R\gamma}{(\gamma - 1)} \\ \frac{R}{c_p} &= \frac{(\gamma - 1)}{\gamma}. \end{aligned}$$

Inserting equation (2.23) into equation (2.22) yields the *Poisson* equation

$$T_{\text{exp}} = T_0 \left(\frac{P_{\text{exp}}}{P_0} \right)^{(\gamma-1)/\gamma}. \tag{2.24}$$

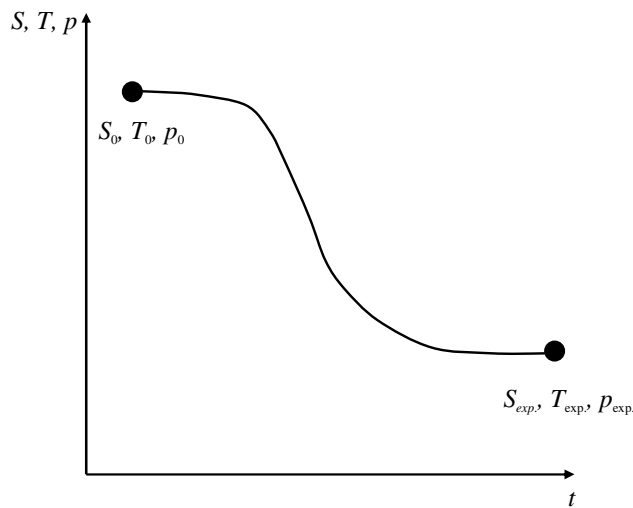


Figure 2.6: The expansion path from the initial entropy S_0 , temperature T_0 , and pressure p_0 to the final expansion entropy S_{exp} , temperature T_{exp} , and pressure p_{exp} .

For earlier *n*-nonane measurements available in literature the effect of treating the heat capacity in a temperature dependent manner (equation (2.21)) compared to a constant value (equation (2.24)) of $\gamma = c_p / c_v = 1.1$ is analyzed in chapter 6.2.

2.4 Classical Nucleation Theory by *Becker* and *Döring*

The first theoretical approach to homogeneous nucleation was given by *Volmer* and *Weber*

in 1926.²⁹ Both alluded to the theory of curved surfaces developed by *Gibbs* during 1876 / 1878 and emphasized that the stability of a supersaturated gas is a question of kinetics. *Farkas*³⁰ developed a new model in 1927, which was the basis for many following theories. *Becker* and *Döring*³¹ used this model to develop a simple analytical expression for the nucleation rate J as a function of the temperature T and the supersaturation S . This theory is called Classical Nucleation Theory (CNT).

The Classical Nucleation Theory uses three basic approximations: First, the liquid droplet is considered as a homogeneous and incompressible sphere with a sharp interface. Second, a cluster consisting of only a few molecules has the same thermo-physical properties as its macroscopic bulk liquid phase. This is referred to as the “capillarity approximation”. The advantage of using this approximation is that the nucleation rate J can be calculated by using macroscopic properties for the nano-cluster, e.g. the cluster has the surface tension, the density, and the vapor pressure of the bulk flat liquid. Third and final, the vapor is ideal.

For the Classical Nucleation Theory *Becker* and *Döring*³¹ used a *Boltzmann* approach to describe the nucleation rate J

$$J = K \cdot \exp(-\Delta G^*/kT). \quad (2.25)$$

Here ΔG^* is the *Gibbs* energy of formation for the critical cluster, k the *Boltzmann* constant, T the temperature, and K the pre-exponential factor.

The *Gibbs* energy ΔG^* of the critical cluster is derived by thermodynamic relations. For a newly built critical cluster consisting of n molecules out of the mother gas phase, n molecules change their chemical potential G_m , additionally a new spherical surface with the surface tension σ_{ST} of a droplet with the radius r needs to be built up. Thus, the *Gibbs* energy of the critical cluster is given by

$$\Delta G = n\Delta G_m + 4\pi r^2 \sigma_{ST}. \quad (2.26)$$

The change in the chemical potential from the gas phase $G_{m,g}$ to the liquid phase $G_{m,l}$ is

$$\Delta G_m = G_{m,l} - G_{m,g} = -kT \ln S. \quad (2.27)$$

Here S is the supersaturation which is the ratio of the actual vapor pressure to the equilibrium vapor pressure at the given temperature. The first approximation of the Classical Nucleation Theory, i.e. the cluster is spherical, gives us the number of molecules in the criti-

²⁹ Volmer and Weber, 1926.

³⁰ Farkas, 1927.

³¹ Becker and Döring, 1935.

cal cluster

$$n = \frac{4\pi r^3}{3v_l}. \quad (2.28)$$

Here v_l is the molecular volume in the liquid. By including equations (2.27) and (2.28) into (2.26) the following equation is obtained for the *Gibbs* energy

$$\Delta G = -\frac{4\pi r^3}{3v_l}kT \ln S + 4\pi r_n^2 \sigma_{ST}. \quad (2.29)$$

In Figure 2.7 the free enthalpy of cluster formation is shown as a function of the cluster radius. Here we can distinguish between two cases: First, the saturation being lower than one, meaning that the vapor pressure of the nucleating substance is lower than its equilibrium vapor pressure at the given temperature. In this case the first part of equation (2.29) generates positive values. Thus, the *Gibbs* free enthalpy rises to an infinite value. The barrier which needs to be overcome in order for nucleation to occur is infinitely high. Therefore, nucleation cannot take place in subsaturated systems. And in the second case, the saturation is higher than one. In this case the first part of the equation (2.29), which is influenced by the third moment of the radius, generates negative values and dominates the *Gibbs* energy ΔG at large radii compared to the second part of the equation, influenced by the second moment of the radius, which dominates at small radii. Thus, the *Gibbs* free energy passes through a maximum at a certain radius, the critical radius r^* , and declines as the radius increases.

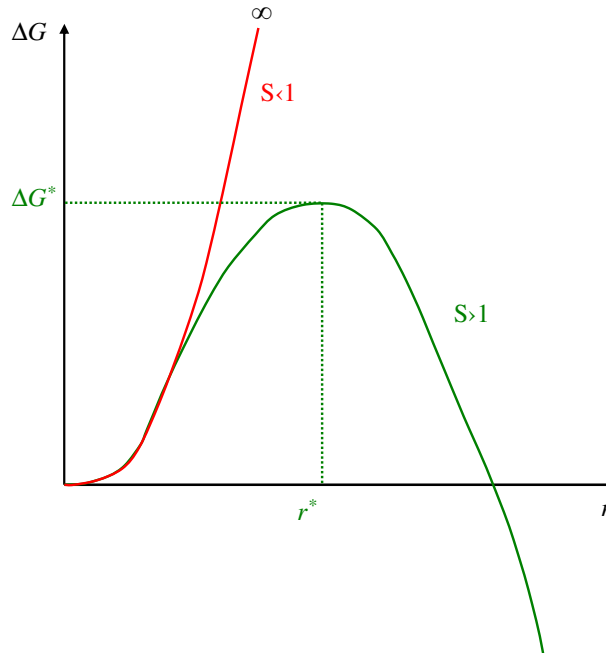


Figure 2.7: A schematic diagram of the *Gibbs* energy for cluster formation in a subsaturated (red solid line) and a supersaturated (green solid line) vapor according to CNT as a function of the cluster radius r (equation (2.29)). The barrier ΔG^* is located at the critical cluster radius r^* .

To obtain the critical cluster size the free *Gibbs* energy has to be derived with respect to the radius and placed zero

$$\frac{\partial \Delta G^*}{\partial r} = 0. \quad (2.30)$$

From this the radius of the critical cluster is obtained

$$r^* = \frac{2\sigma_{ST}v_l}{kT \ln S}. \quad (2.31)$$

By inserting equation (2.31) into equation (2.28) the number of molecules in the critical cluster is given by

$$n^* = \frac{32\pi v_l^2 \sigma_{ST}^3}{3(kT \ln S)^3}. \quad (2.32)$$

Figure 2.8 illustrates schematically the sensitivity of the critical cluster radius (equation (2.31)) and the number of molecules in the critical cluster (equation (2.32)) vs. the supersaturation of the gas phase at a constant temperature. The supersaturation is varied by varying the partial pressure of the condensible species. With increasing supersaturation in the gas phase the critical cluster size and the number of molecules in the critical cluster decreases. Clearly the effect of decreasing critical cluster size and decreasing number of molecules in the critical cluster is the largest at small supersaturations.

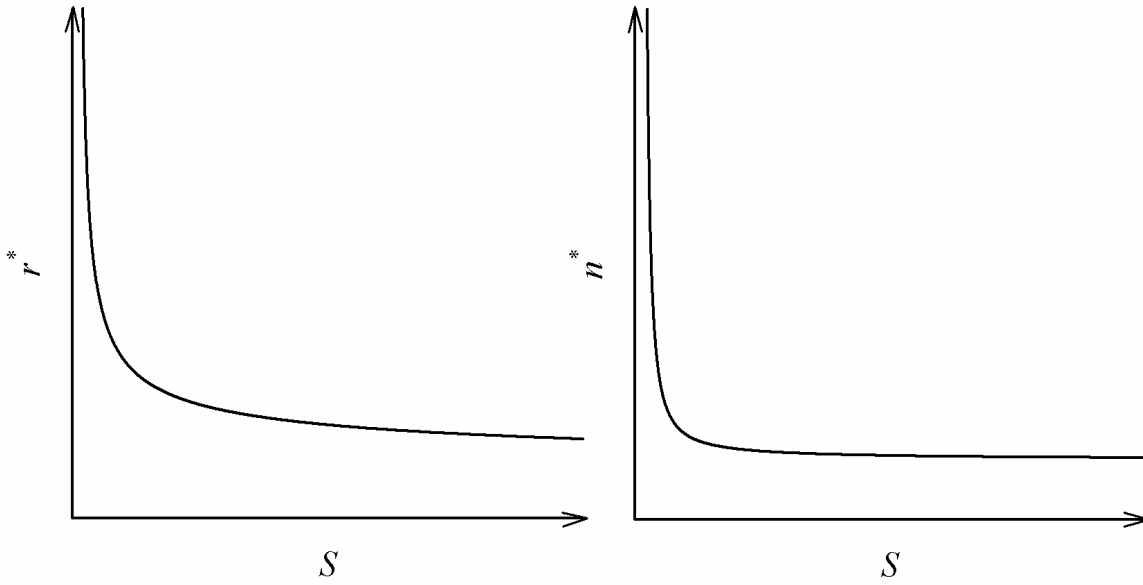


Figure 2.8: The sensitivity of the critical cluster radius (left, equation (2.31)) and the number of molecules in the critical cluster (right, equation (2.32)) vs. the supersaturation at a constant temperature. The supersaturation is varied by varying the partial pressure of the nucleating species.

The *Gibbs* energy of the critical cluster ΔG^* is obtained by inserting equation (2.31) into equation (2.29)

$$\Delta G^* = \frac{16\pi v_l^2 \sigma_{ST}^3}{3(kT \ln S)^2}. \quad (2.33)$$

Figure 2.9 illustrates the sensitivity of the *Gibbs* energy to the supersaturation as a function of the cluster radius. Increasing the supersaturation ($S > 1$, Figure 2.9 left to $S \gg 1$, Figure 2.9 right) in a system lowers the critical *Gibbs* energy and shifts the critical cluster size towards smaller radii.

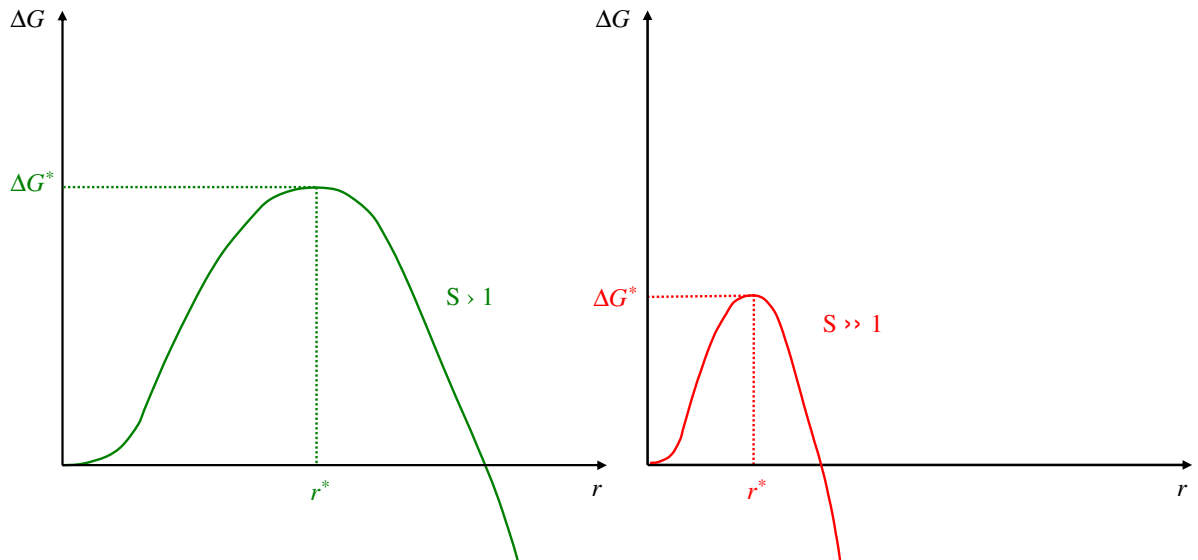


Figure 2.9: The sensitivity of the *Gibbs* energy for cluster formation to the supersaturation as a function of the cluster radius at constant temperature.

Figure 2.10 illustrates the critical *Gibbs* energy for cluster formation predicted by CNT as a function of supersaturation at constant temperature. Increasing the supersaturation in the gas phase decreases the critical *Gibbs* energy. Clearly the effect of decreasing critical *Gibbs* energy is the largest at small supersaturations and becomes significantly smaller with increasing supersaturation, however does not vanish even at very high supersaturations.

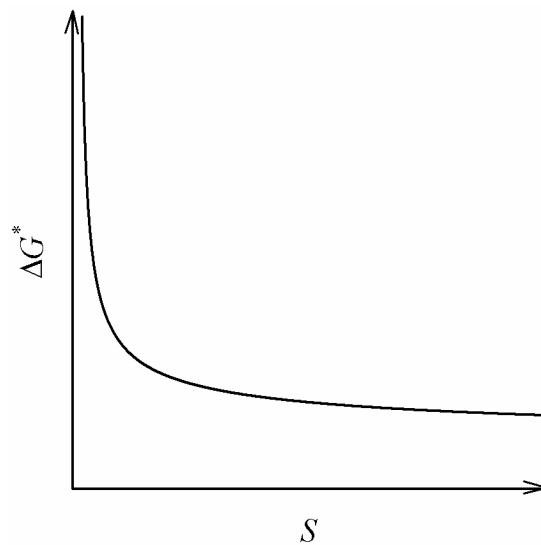


Figure 2.10: A schematic diagram of the *Gibbs* energy of the nucleation barrier predicted by CNT as a function of the supersaturation at constant temperature. The barrier does not vanish even for very high values of supersaturation.

The derivation of the kinetic pre-exponential factor K is obtained by considering a quasi-stationary condensation process, in which primarily the condensation and evaporation rate of monomers onto a cluster are examined.³² According to this the pre-exponential factor is given by

$$K = v_l N_l^2 \sqrt{\frac{2\sigma_{ST}}{\pi\mu}}. \quad (2.34)$$

Here μ is the molecular weight of the nucleating substance and N_l the number density of monomers, which can be obtained from the number of particles and the ideal gas law

$$N_l = \frac{N}{V} = \frac{p}{kT}. \quad (2.35)$$

Finally, the classical nucleation rate J_{BD} is expressed by

$$J_{BD} = \sqrt{\frac{2\sigma_{ST}}{\pi\mu_v}} v_m \left(\frac{p_v}{kT}\right)^2 \exp\left\{\frac{-16\pi v_m^2 \sigma_{ST}^3}{3(kT)^3 (\ln S)^2}\right\}. \quad (2.36)$$

³² Becker and Döring, 1935.

3 Experimental Setup

The experimental work consists of two sets of experiments: First, pressure trace measurements are conducted during supersonic nozzle expansion experiments. All of these experiments have been performed in April – Juli 2005 at The Ohio State University, Columbus, OH, USA, with an exception of 11 experiments which were carried out in September 2003 at the Worcester Polytechnic Institute, Worcester, MA, USA. Second, the Small Angle X-ray Scattering experiments were conducted in December 2005 at the National Advanced Photon Source, Argonne National Laboratory, IL, USA.

This chapter will first give a detailed description of the majority of the pressure trace measurements. The 11 pressure trace measurements which were carried out in September 2003 at the Worcester Polytechnic Institute, Worcester, MA, USA use a very similar experimental setup discussed in detail elsewhere.³³ After this, the Small Angle X-ray Scattering experiments are described in-depth.

3.1 Pressure Trace Measurements

The supersonic nozzle apparatus used for the majority of the pressure trace measurements consists of the carrier gas generator, the vaporizer, the heat exchanger and the plenum, and the nozzle with the pressure probe. The plenum, the flow straightener, and the nozzle are located in a vacuum box to reduce the heat transfer to the environment. Figure 3.1 exhibits a schematic diagram of the experimental setup.

³³ Gharibeh *et al.*, 2005.

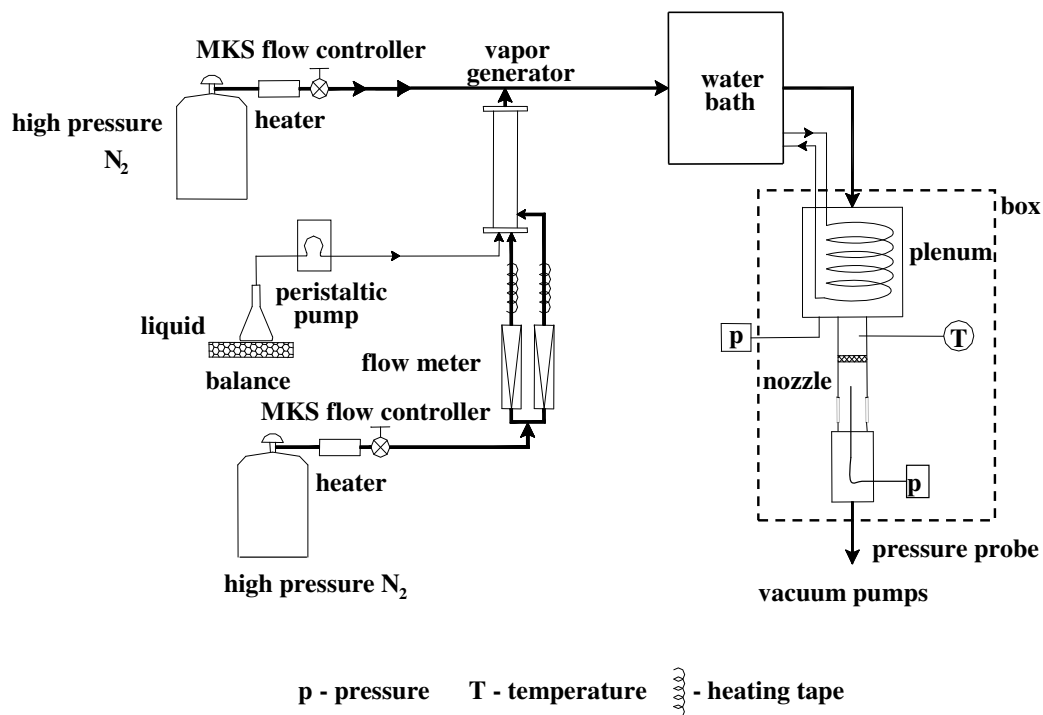


Figure 3.1: A schematic diagram of the experimental setup for the pressure trace measurements.

Depending upon the *n*-alkane under study N_2 or Ar is used as carrier gas. Two carrier gas streams, the main - and the secondary gas stream, is drawn from the gas side of two high pressure liquid Dewars. Electrical heaters (1000 FS Mc ILRRATH'S Heaters) bring the gas to room temperature to prevent regulators and gas lines from freezing. Two mass flow controllers (MKS flow controllers Range 400 SLM and 200 SLM) monitor and control each of the carrier gas flow rates (Figure 3.2).

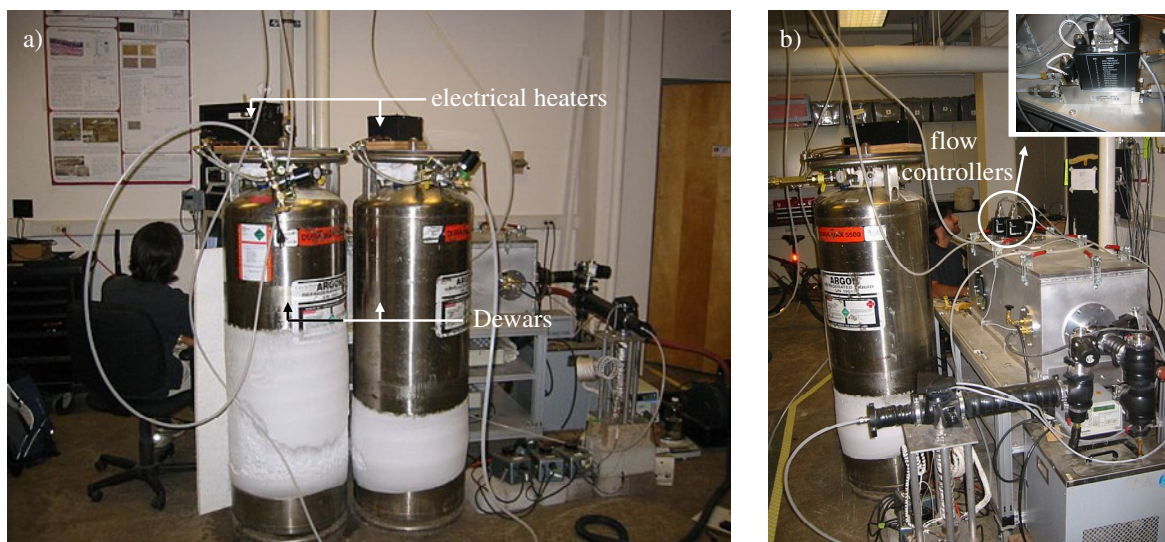


Figure 3.2: The Dewars, electrical heaters (a), and the mass flow controllers during the experiment (b).

The secondary carrier gas stream is heated further by heating bands, before it reaches the vaporizer. Here, a peristaltic pump (Master flex pump, Model 7525-20) transports the condensible liquid at a constant flow through a needle (1.6 mm diameter) into the vaporizer. This needle is inserted into the vaporizer through a hole in a plate which is 0.15 mm wider than the diameter of the needle. Part of the secondary carrier gas stream flows through this gap to disperse the condensible liquid into a fine spray. The remaining secondary carrier gas stream flows through eight additional holes drilled symmetrically around the needle in the plate. This disperses the condensible liquid further and provides the energy to evaporate the droplets and dilute the vapor. The mass flow rate of the condensible is determined by monitoring the weight change of the condensible located in a flask on a balance over the length of the experiment (Figure 3.3).

The vapor rich gas stream is combined with the main carrier gas stream and the mixture flows through a heat exchanger placed in a temperature controlled circulating water bath (VWR Scientific, Model 1157). This water bath also controls the plenum temperature T_0 , while the plenum pressure p_0 is controlled by the flow through the system (Figure 3.3).

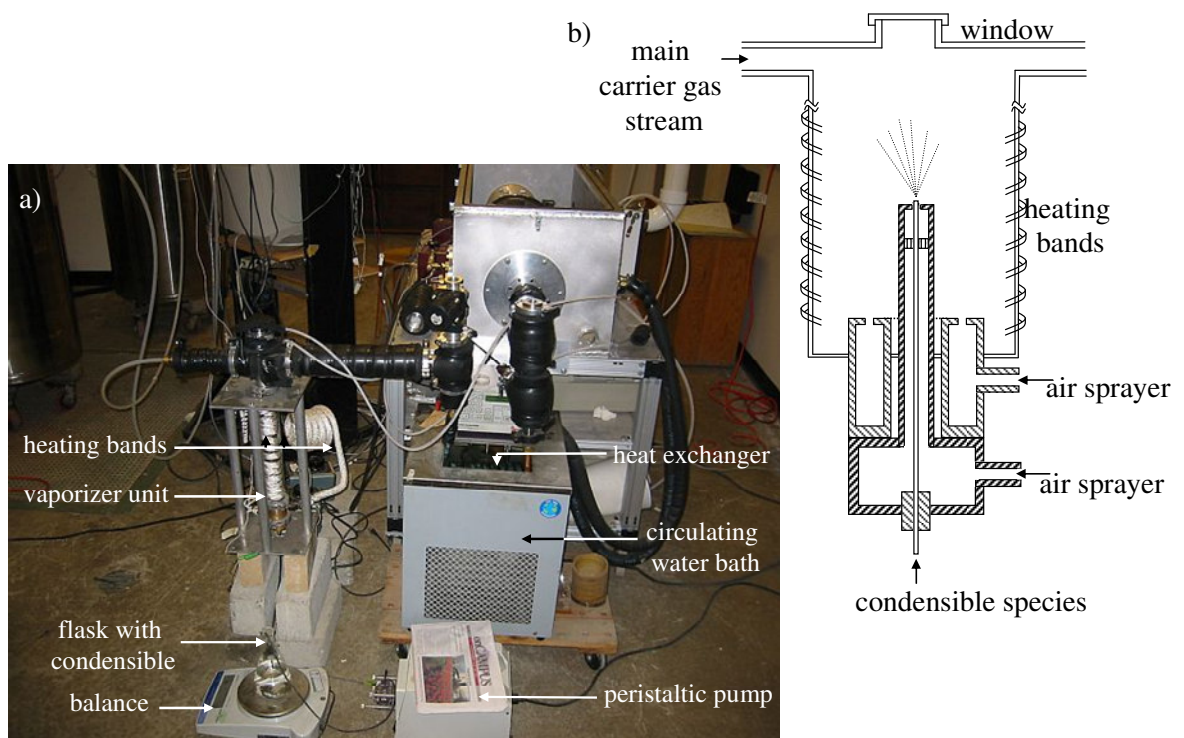


Figure 3.3: A view of the vaporizer unit, the flask containing the condensible, the balance, the heat exchanger, and the circulating water bath (a), and a schematic diagram of the vaporizer (b).

The gas mixture continues its flow through the plenum in which a copper heating spiral

is located. The copper heating spiral is fed with water from the thermostat. In the plenum the velocity of the gas is ~ 0.3 m/s, and compared to sonic speed (~ 340 m/s) at the throat of the nozzle, stagnation conditions can be assumed. A MKS Baratron (MKS Type 690A) attached to the plenum measures the stagnation pressure p_0 . After the gas passes through the plenum it continues through the flow straightener (6.4 cm x 2.54 cm x 1.27 cm). Here a platinum resistance temperature detector (RTD, Omega Engineering, Type A, sensing element) measures the plenum temperature T_0 . Figure 3.4a exhibits a view of the closed box in which the plenum is located during an experiment. In Figure 3.4b the box is opened for demonstration purposes.

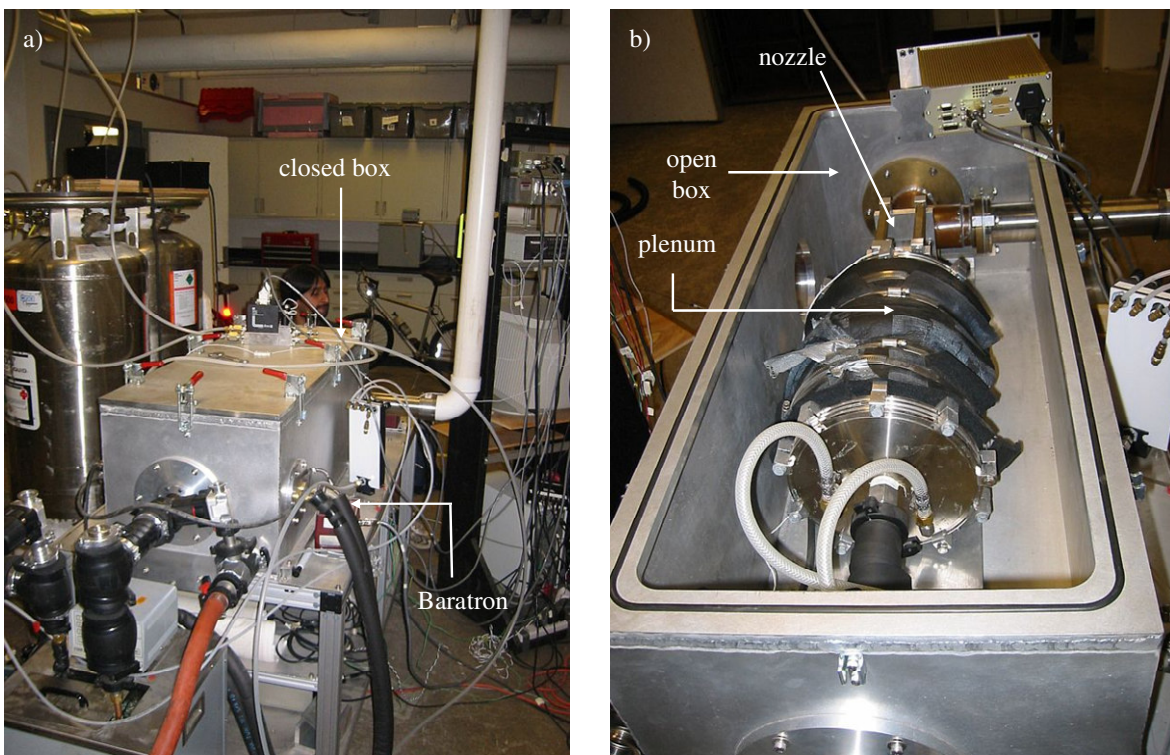


Figure 3.4: A view of the closed box and the MKS Baratron (a) during the experiment. Additionally, a view in the open box with the plenum and the nozzle (b).

The gas mixture enters the Laval nozzle (Figure 3.5a and b), which consists of two shaped nozzle blocks defining the top and bottom surface, and two flat sidewalls. The top and the bottom surface are shaped in a manner that the nozzle consists of a converging and a diverging section through which the gas flows. A movable pressure probe measures the static pressure of the gas as a function of the axial position along the center line of the nozzle, from ~ 2 cm upstream of the throat to ~ 8 cm downstream of the throat. The pressure

probe is a 30.5 cm long hollow, front side capped tube with a diameter of 0.102 cm. Three holes with a diameter of 0.05 cm are drilled symmetrically 15.7 cm downstream of the capped tip. The open back side is attached to a MKS Baratron (Type 690 A) (Figure 3.5c). Finally, the flow is exhausted to atmospheric pressure by two pumps (Figure 3.5d).

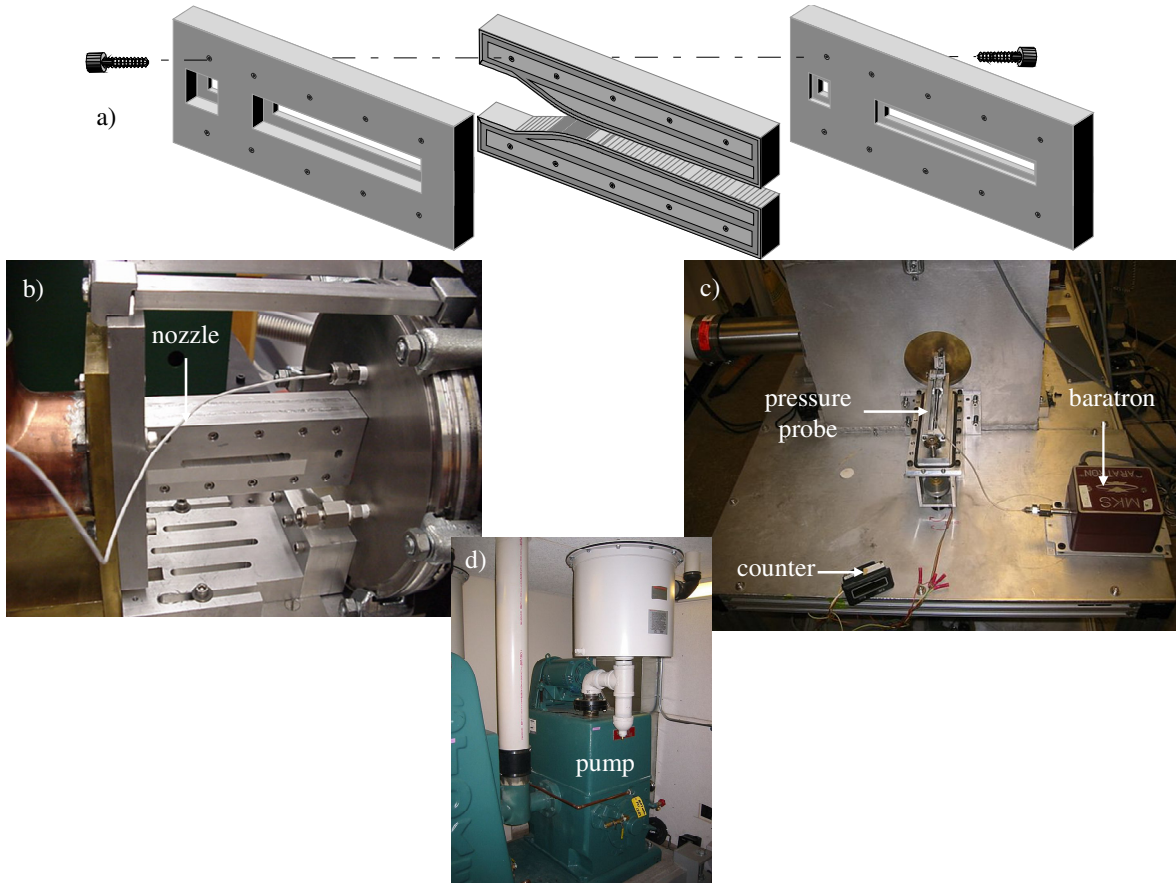


Figure 3.5: The nozzle is built up from two sidewalls and a top and bottom plate (a), a view of the nozzle in the experimental setup (b), the movable pressure probe, MKS Baratron, counter (c), and the pumps (d).

The majority of the reported condensation experiments were performed at a stagnation pressure of $p_0 = 30.2 \pm 0.02$ kPa. The 11 *n*-nonane runs, performed in 2003 were carried out at a stagnation pressure of $p_0 = 59.6 \pm 0.02$ kPa.³⁴ The opening angle of nozzle C, used for the *n*-alkane pressure trace measurements, is $d(A/A^*)/dx = 0.078$ cm⁻¹ in the supersonic region, with A being the effective area of the nozzle and A^* the effective area of the throat. The opening angle for the nozzle was determined by a linear fit to the area ratio from 2 cm to 7 cm downstream of the throat.

Once the system reaches stable operating conditions, a pressure trace $p(x)$ is measured

³⁴ Gharibeh *et al.*, 2005.

starting with the pressure probe at the furthest upstream position, 2 - 3 cm upstream of the throat. Several pressure trace measurements are conducted in the sub-sonic region. In the vicinity of the throat the measurements are conducted at 0.1 mm intervals, and downstream of the throat the pressure is measured at 1.0 mm intervals to the end of the nozzle. In addition to recording the static pressure at each position x , the stagnation temperature T_0 , the stagnation pressure p_0 , the flow rate of the carrier gas \dot{m}_i , and the time of each condensible experiment are recorded using a digital-to-analog board (Keithly DAS1602) and a desktop computer. At every measurement position a burst of 21 measurements are taken for every variable in less than 1 s via direct memory access mode, and the average value of each variable and its standard deviation are computed. In addition, the mass flow rate of the condensible liquid entering the system is recorded manually for the time period of each flow rate experiment. Before the actual experiment starts, a dry trace experiment (only carrier gas) is conducted. After this the wet trace measurements of experimental interest are carried out (carrier gas with condensible species).

3.2 Small Angle X-ray Scattering Experiments

The supersonic nozzle apparatus used in the Small Angle X-ray Scattering experiments is the setup used for earlier spectroscopy work³⁵ with the additional improvement that the carrier gas flow is now controlled using two MKS mass flow controllers (MKS flow controllers Range 400 SLM and 200 SLM). Figure 3.6 exhibits a schematic diagram of the experimental setup.

³⁵ Paci *et al.*, 2004.

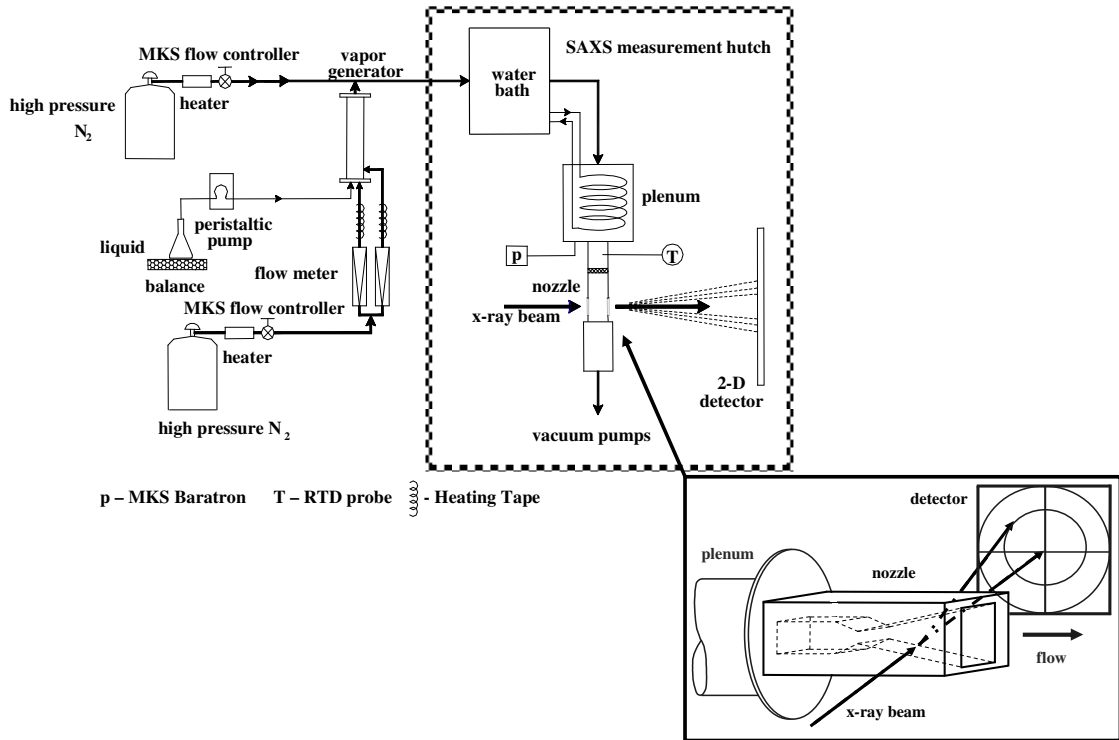


Figure 3.6: A schematic diagram of the setup for the Small Angle X-ray Scattering experiments.

Since the fundamental method of operation for this supersonic nozzle apparatus is similar to that used for the thermodynamic measurements (Section 3.1) only the main differences will be presented here. First, for the Small Angle X-ray Scattering experiments the plenum and the nozzle are not contained in a metal vacuum box. Second, the stagnation temperature T_0 is measured slightly further upstream of the nozzle entrance. And finally, the stagnation pressure p_0 is determined by measuring the static pressure through a pressure tap in the entrance region of the nozzle, where the cross section is constant and correcting for the velocity of the gas. These changes in the setup are due to geometrical issues concerning space availability.

As illustrated in Figure 3.7, at the x-ray facility the carrier gas and the vapor generator system were located outside of the SAXS measurement hutch, while the water bath, plenum, nozzle, and the pumps were located inside (Figure 3.7).

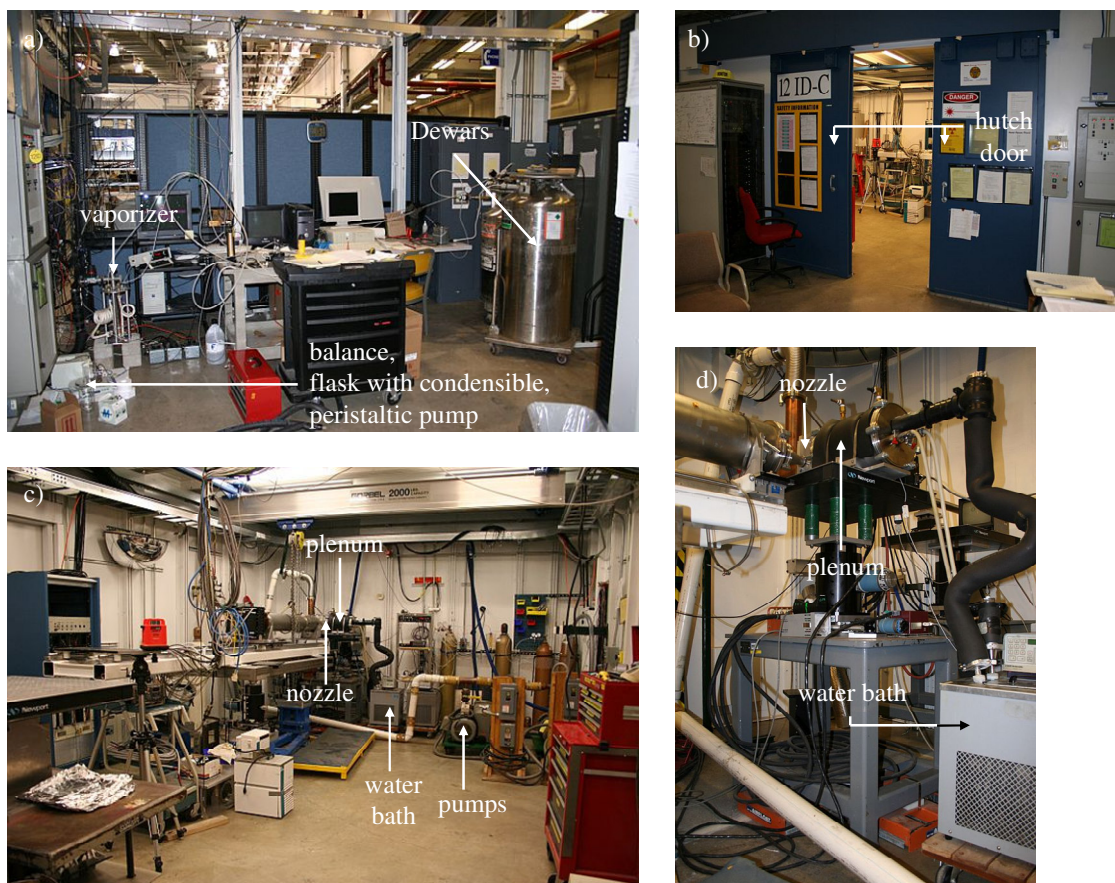


Figure 3.7: A view inside and outside of the SAXS hutch.

As for the pressure trace measurements our nozzles for the SAXS studies (nozzle H2 and nozzle C2) are machined from aluminium and consist of two shaped nozzle blocks that define the top and bottom surface, and two flat sidewalls. Each sidewall has a window consisting of a 1 mm x 90 mm slot covered by a 25 μm thick piece of mica (10 mm x 100 mm) glued in place using epoxy. The experimental setup is built up in a manner that the x-ray beam is guided in a right angle through these windows (Figure 3.8). The opening angle of the nozzle used for the *n*-alcohol SAXS measurements (nozzle H2) is $d(A/A^*)/dx = 0.054 \text{ cm}^{-1}$, while the opening angle of the nozzle used for the *n*-alkane SAXS measurements (nozzle C2) is $d(A/A^*)/dx = 0.078 \text{ cm}^{-1}$. The opening angles for both nozzles were determined by a linear fit to the area ratio from 2 cm to 7 cm downstream of the throat.

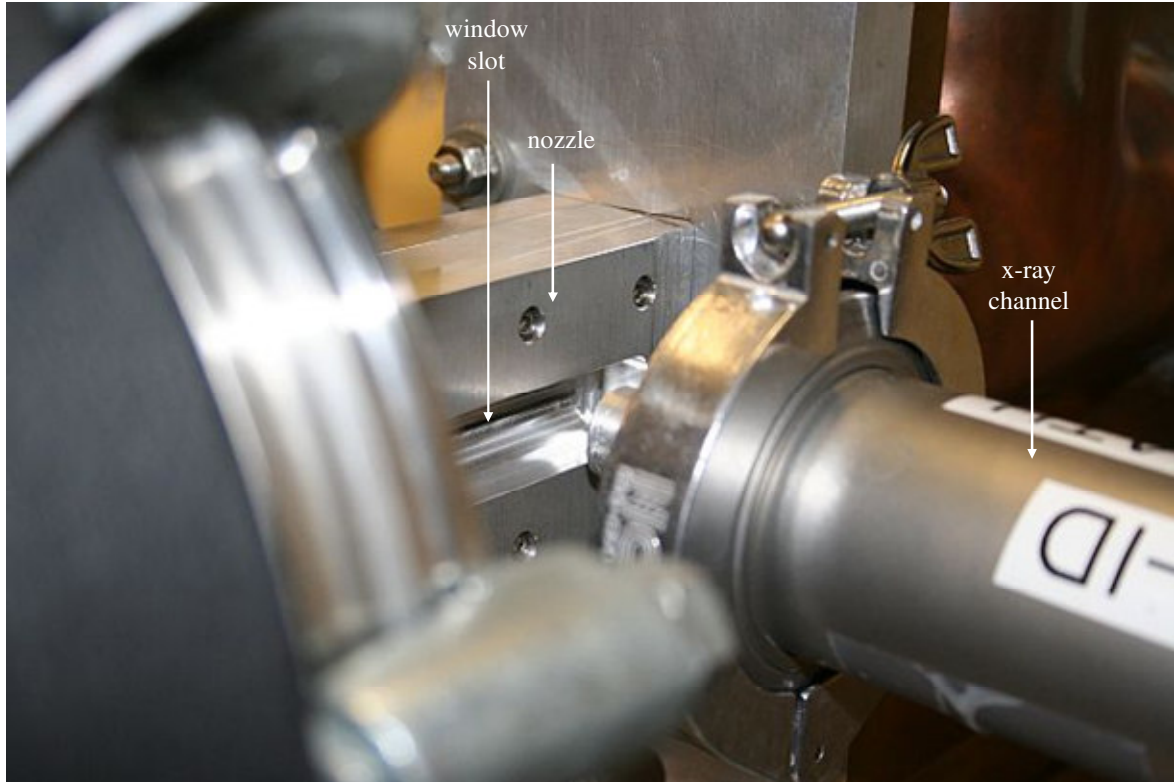


Figure 3.8: A view of the nozzle side wall with the window slots.

The SAXS measurements were performed using the Besserc 12-ID beam line³⁶ at the Advanced Photon Source, Argonne National Labs., Argonne, IL. A 0.2 mm x 0.2 mm beam of 12 keV ($\lambda = 1.0332 \cdot 10^{-10}$ m)³⁷ x-ray with a wavelength of spread $\Delta\lambda/\lambda = 10^{-4}$ passes through the nozzle at a right angle to the gas flow. The two dimensional detector consists of a mosaic of nine CCD chips with a 15 cm x 15 cm active area comprised of 3072 x 3072 pixels. The sample to detector distance (SDD) was fixed at 2.0 m and the q -range was calibrated by scattering from a sample of silver behenate.³⁸ Here the scattering vector q is related to the scattering angle θ and the x-ray wavelength λ by

$$q = \left(\frac{4\pi}{\lambda} \right) \sin\left(\frac{\theta}{2} \right). \quad (3.1)$$

The absolute calibration factor was established by scattering from several D₂O aerosols that were produced under conditions identical to a previous SANS study.³⁹ The total integration time for each spectrum was 5 s for the sample (nozzle with carrier gas and conden-

³⁶ Seifert *et al.*, 2000.

³⁷ For those who have asked me: Yes, it is possible to calculate λ from E : $E = h_{\text{planck}} a/\lambda$.

³⁸ Huang *et al.*, 1993; Blanton *et al.*, 1995; Megens *et al.*, 1997.

³⁹ Wyslouzil, Strey, and Wilemski, 2007.

sible) and 5 s for the empty cell (nozzle with carrier gas). The sample and the empty cell measurements were alternated. For the data reduction the local empty cell measurement has always been used. To produce radially averaged spectra the APS data inversion program that corrects for dark background, pixel efficiency, and special inhomogeneities has been used.

4 Data Analysis

The backbone of every experimental work is the analysis of the measured data. In this thesis many data analysis techniques acquired from former research projects are used.⁴⁰ However, also innovative improvements for the data analysis have been imported: As the n -alkanes are more complex molecules, the temperature dependency of the heat capacity has been imbedded into the data analysis technique for the very first time. Further, a novel approach to calculate the characteristic time has been developed.

In chapter 4.1 the analytical technique used for the data reduction of the pressure trace measurements is explained. The procedures for the analysis of Small Angle X-ray Scattering curves are presented in chapter 4.2.

4.1 Pressure Trace Measurement

To analyze the pressure trace measurements, first, the effective nozzle geometry has to be determined (Chapter 4.1.1). In a second step, the pressure profiles of the wet condensing flows have to be rescaled for the effective throat position (Chapter 4.1.2). In a third step, the entire history of the flow can be calculated (Chapter 4.1.3), i.e. the temperature $T(x)$, the density $\rho(x)$, the velocity $u(x)$, and the condensate mass fraction $g(x)$ at every position x in the nozzle. Finally, the maximum nucleation conditions can be determined (Chapter 4.1.4).

4.1.1 Effective Area Ratio

To determine the variables of interest for the condensible flow, i.e. the temperature $T(x)$, the density $\rho(x)$, the velocity $u(x)$, and the condensate mass fraction $g(x)$ at every position x in the nozzle it is essential to know the exact nozzle geometry. However, the area ratio A/A^* with no gas flowing through the nozzle (physical area ratio) changes once gas flows through the nozzle (effective area ratio) due to boundary layers. Thus, it is not as simple as

⁴⁰ Wyslouzil *et al.*, 2000a.

to meter the physical area ratio to know the exact nozzle geometry. To obtain the effective area ratio a dry trace measurement (carrier gas, i.e. pure nitrogen or argon) is analyzed by the following set of equations:

$$M^2 = \frac{2}{\gamma - 1} \left[\left(\frac{p}{p_0} \right)^{(1-\gamma)/\gamma} - 1 \right] \quad (4.1)$$

and

$$\frac{A}{A^*} = \frac{1}{M} \left[\frac{2 + (\gamma - 1)M^2}{\gamma + 1} \right]^{(\gamma+1)/(2\gamma-2)}. \quad (4.2)$$

Here, T_0 is the stagnation temperature, p_0 the stagnation pressure, and $M = u/a$ the Mach number, with u being the local velocity of the gas, $a^2 = \gamma RT/\mu$ the local speed of sound, $\gamma = c_p/c_v$ the ratio of constant pressure and volume heat capacity, R the universal gas constant, and μ the molecular weight.

4.1.2 Rescaling for the Effective Throat Position for the Condensing Flow

In a first step, it is necessary to rescale the counter position of the pressure ratio p/p_0 measurements for the wet condensing flow relative to the effective throat position. For pressure trace measurements, the position of the throat ($M = 1$) is found by determining the location of p^*/p_0 . However, when c_p is not constant, i.e. γ is a strong function of the temperature, as for the n -alkanes, the usual isentropic relationship

$$\frac{p^*}{p_0} = \left\{ \frac{2}{\gamma + 1} \right\}^{\gamma/(\gamma-1)} \quad (4.3)$$

is not accurate enough. Thus, a novel integration procedure is used for rescaling.⁴¹ For this the following set of equations are used⁴²

$$\frac{dT}{T} = \frac{(\gamma - 1)M^2}{1 - M^2} \frac{dA}{A}, \quad (4.4)$$

$$\frac{du}{u} = -\frac{1}{1 - M^2} \frac{dA}{A}, \quad (4.5)$$

⁴¹ Tanimura *et al.*, 2007.

⁴² Shapiro, 1953.

$$\frac{dp}{p} = \frac{\gamma}{\gamma-1} \frac{dT}{T}. \quad (4.6)$$

From the definition of $M = u/a$ one obtains

$$\begin{aligned} \frac{da}{a} &= \frac{du}{u} - \frac{dM}{M} \\ &= \frac{d\gamma}{2\gamma} + \frac{dT}{2T}. \end{aligned} \quad (4.7)$$

Combining equation (4.4) - (4.7) yields the following expression for dp/p ,

$$\frac{dp}{p} = -\frac{2\gamma M dM + M^2 d\gamma}{2 + (\gamma-1)M^2}, \quad (4.8)$$

where $d\gamma$ is given by

$$d\gamma = \left(\frac{\partial\gamma}{\partial T}\right)dT + \left(\frac{\partial\gamma}{\partial p}\right)dp. \quad (4.9)$$

From equation (4.6), (4.8), and (4.9) $d\gamma$ can be written in terms of dM

$$d\gamma = -\frac{2f\gamma(\gamma-1)MdM}{\gamma + f(\gamma-1)M^2}, \quad (4.10)$$

$$f \equiv \left\{ \frac{\partial\gamma}{\partial T} + \frac{p}{T} \frac{\gamma}{\gamma-1} \frac{\partial\gamma}{\partial p} \right\} / \{2 + (\gamma-1)M^2\}. \quad (4.11)$$

The pressure and temperature at the throat are determined by integrating equation (4.6), (4.8), and (4.10) from $M = 0$ to $M = 1$. In this work, the pressure dependency of γ was neglected, i.e. $(\partial\gamma/\partial p) = 0$, while the temperature dependency of c_p is given in chapter A.3.

4.1.3 Flow Profiles

The n -alkanes are longer, and more complex molecules compared to the isotopes of water and the n -alcohols ($n\text{-C}_i\text{H}_{2i+1}$, $i = 3 - 5$), substances that have been studied to date in our experimental setup.⁴³ As direct consequence the heat capacity $c_p(T)$, and the heat capacity ratio

$$\gamma = c_p(T)/c_v(T) = c_p(T)/(c_p(T) - R) \quad (4.12)$$

⁴³ Wyslouzil *et al.*, 2000a; Heath *et al.*, 2002; Streletzky *et al.*, 2002; Heath *et al.*, 2003; Khan *et al.*, 2003; Kim *et al.*, 2004; Paci *et al.*, 2004; Gharibeh *et al.*, 2005; Tanimura, Zvinevich, and Wyslouzil, 2005.

are functions of the temperature and must be treated as such when analyzing the pressure measurement data to determine the temperature $T(x)$, the density $\rho(x)$, the velocity $u(x)$, and the condensate mass fraction $g(x)$ at every position x in the nozzle. To derive these key unmeasured properties we assume the effective area ratio of the pure carrier gas flow and that of the condensable mixture as identical. This value is used to determine the variables of interest by integrating the diabatic flow equations cast in a form with pressure and area ratio as the known quantities.⁴⁴ The first two equations are the mass balance equation

$$u = \frac{u^* \rho^* A^*}{\rho A} \quad (4.13)$$

and the density equation

$$d\left(\frac{\rho}{\rho_0}\right) = \left[\frac{1}{\gamma(T)} \left(\frac{u^*}{u}\right)^2 \frac{T_0}{T^*} \right] d\left(\frac{p}{p_0}\right) - \left(\frac{\rho}{\rho_0}\right) d \ln\left(\frac{A}{A^*}\right). \quad (4.14)$$

Here the asterisk indicates that the variables are evaluated at the throat position. The subscript zero indicates stagnation values. Equation (4.14) is a combination of the momentum equation,

$$p u du = -p \quad (4.15)$$

and the mass balance equation (4.13). One of the two remaining diabatic flow equations is the complete temperature change equation

$$d\left(\frac{T}{T_0}\right) = \left[w_0(g) - \frac{1}{\gamma(T)} \left(\frac{u^*}{u}\right)^2 \frac{T}{T^*} \right] \frac{\rho_0}{\rho} d\left(\frac{p}{p_0}\right) + \left(\frac{T}{T_0}\right) \left[d \ln\left(\frac{A}{A^*}\right) + w(g) dg \right]. \quad (4.16)$$

Here the quantities $w_0(g)$ and $w(g)$ are defined as

$$w_0(g) = \mu / [\mu_0 (1 - g)] \quad (4.17)$$

and

$$w(g) = \mu / [\mu_v (1 - g)], \quad (4.18)$$

where μ is the mean molecular weight of the gas mixture when the condensate mass fraction g is non-zero and μ_0 is the corresponding value of μ at the stagnation conditions when $g = 0$.

⁴⁴ Wegener, 1966.

In order to integrate equation (4.16) it is necessary to investigate how the condensate mass fraction g varies in the nozzle. This is determined by first combining the energy equation for the heat added per unit mass of gas flow Q with equation (4.16) to eliminate dT . This is followed by using the definition of dQ in terms of g

$$dQ = L(T)dg, \quad (4.19)$$

where $L(T)$ is the latent heat of condensate per unit mass. The result is

$$\left[\frac{L(T)}{c_p(T) T_0} - \frac{T}{T_0} w(g) \right] dg = \left(\frac{\rho}{\rho_0} \right) \left[h - \frac{1}{\gamma(T)} \left(\frac{u^*}{u} \right)^2 \frac{T}{T^*} \right] d \left(\frac{p}{p_0} \right) + \left(\frac{T}{T_0} \right) d \ln \left(\frac{A}{A^*} \right), \quad (4.20)$$

where

$$h = w_0(g) - \frac{c_{p0}}{c_p(T)} \left(\frac{\gamma_0 - 1}{\gamma_0} \right) \quad (4.21)$$

is the specific heat of the flowing gas stream.

Finally, to calculate the theoretical expansion of a vapor-carrier gas mixture in the absence of condensation, the “wet isentrope”, equation (4.13) - (4.16), is integrated and dg and g is set to zero.

Once the temperature profile $T(x)$ and the condensate mass fraction profile $g(x)$ are known, the driving force of the nucleation, the supersaturation profile $S(x)$ is calculated

$$S(x) = \frac{p(x)}{p^\infty(T(x))}. \quad (4.22)$$

Here $p^\infty(T(x))$ is the equilibrium vapor pressure of the condensible species and $p(x)$ is the partial pressure of the condensible which is related to the initial conditions and the condensate mass fraction by

$$p(x) = y_0 p_0 \left(\frac{p(x)}{p_0} \right) \left(1 - \frac{g(x)}{g_\infty} \right). \quad (4.23)$$

Here $g_\infty = \dot{m}_v / (\dot{m}_v + \dot{m}_i)$ is the initial mass fraction of the condensible in the gas mixture, \dot{m}_v and \dot{m}_i are the mass flow rates of the condensible vapor and the inert gas respectively. The mole fraction of the condensible vapor in the initial mixture is given by

$$y_0 \equiv \frac{\dot{m}_v/\mu_v}{\dot{m}_i^0/\mu_i}, \quad (4.24)$$

where \dot{m}_v/μ_v is the molar flow rate of the vapor and \dot{m}_i^0/μ_i is the molar flow rate of the inert carrier gas through the nozzle at stagnation conditions.

4.1.4 Maximum Nucleation Conditions and Characteristic Time

The temperature $T_{J_{\max}}$, condensible partial pressure $p_{J_{\max}}$, and supersaturation $S_{J_{\max}}$ corresponding to the maximum nucleation rate J_{\max} are determined by calculating the nucleation rate as a function of position using the temperature $T(x)$ and supersaturation $S(x)$ profiles and the CNT expression by *Becker and Döring*⁴⁵

$$J_{BD} = \sqrt{\frac{2\sigma_{ST}}{\pi\mu_v}} v_m \left(\frac{p_v}{kT}\right)^2 \exp\left\{\frac{-16\pi v_m^2 \sigma_{ST}^3}{3(kT)^3 (\ln S)^2}\right\}. \quad (4.25)$$

Here σ_{ST} is the surface tension of the macroscopic fluid-vapor interface, v_m the molecular volume and k the *Boltzmann* constant. With a known nucleation profile it is easy to determine the temperature $T_{J_{\max}}$, the condensible partial pressure $p_{J_{\max}}$, and the supersaturation $S_{J_{\max}}$ values corresponding to the maximum nucleation rate.

The characteristic time $\Delta t_{J_{\max}}$ is one of the two essential key variables needed to evaluate the experimental maximum nucleation rate $J_{\max} = N / \Delta t_{J_{\max}}$. In this work a novel calculating method is approached to determine the characteristic time compared to the former calculation technique.⁴⁶ To calculate $\Delta t_{J_{\max}}$ it is assumed that the ratio of the experimental particle production rate $\int J_{\exp} dt$ to the experimental maximum nucleation rate J_{\exp}^{\max} is the same as that predicted by CNT⁴⁵ or any other reasonable nucleation rate expression. The characteristic time is given by

$$\Delta t_{J_{\max}} = \frac{\int J_{theory} dt}{J_{theory}^{\max}} = \frac{\int J_{exp} dt}{J_{exp}^{\max}}, \quad (4.26)$$

where

$$dt = \frac{dx}{\langle u \rangle}. \quad (4.27)$$

Here $\langle u \rangle = (u(i) - u(i-1))/2$ with u being the local velocity and the distance between the

⁴⁵ Becker and Döring, 1935.

⁴⁶ Khan *et al.*, 2003.

position i and $i-1$ being 0.02 cm.

4.2 Small Angle X-ray Scattering Experiments

In this section the analysis of the Small Angle X-ray Scattering signal of n -alcohol and n -alkane droplets is described.

4.2.1 X-ray Scattering Length Density

The X-ray Scattering length density of a molecule is given by

$$\rho_{SLD} = \frac{\sum_i Z r_{SL}}{V_m}, \quad (4.28)$$

where Z is the atomic number, $r = 2.81 \cdot 10^{-13}$ cm, and the molar volume is

$$V_m = \frac{\mu}{\rho N_A}. \quad (4.29)$$

Here μ is the molecular weight, ρ the density of the aerosol at the approximated nucleation temperature, and N_A is the *Avogadro* constant. The contrast factor $\Delta\rho_{SLD}$, the difference in scattering length density between the liquid n -alkane or n -alcohol droplet $\rho_{droplet}$ and the surrounding bulk gas phase ρ_{gas} , the carrier gas, is given by

$$\Delta\rho_{SLD} = \rho_{droplet} - \rho_{gas}. \quad (4.30)$$

4.2.2 Scattering of n -Alkane Aerosols

To characterize the n -alkane aerosols, i.e. the average particle radius $\langle r \rangle$, the distribution width σ , and the volume fraction ϕ , the spectra are fit assuming the aerosol consists of a polydisperse *Gaussian* distribution of spheres with a diffuse interface thickness t_D .⁴⁷ In this case the scattering intensity $I(q)$ is given by

$$I(q) = \frac{36\pi}{3} \phi \langle r \rangle^3 \frac{(\Delta\rho_{SLD})^2}{(q \langle r \rangle)^6} [f(1) + f(2) + f(3) + f(4)] \exp(-q^2 t_D^2) + I_{Incoh}, \quad (4.31)$$

$$f(1) = \frac{1}{2} [1 - \cos(2q \langle r \rangle) \exp(-2\sigma^2 q^2)], \quad (4.32)$$

⁴⁷ Strey, 1992.

$$f(2) = -q[\langle r \rangle \sin(2q\langle r \rangle) + 2q\sigma^2 \cos(2q\langle r \rangle)] \exp(-2\sigma^2 q^2), \quad (4.33)$$

$$f(3) = \frac{1}{2} q^2 \left[-4q\langle r \rangle \sigma^2 \sin(2q\langle r \rangle) \exp(-2\sigma^2 q^2) + \langle r \rangle^2 + \sigma^2 \right], \quad (4.34)$$

$$f(4) = \frac{1}{2} q^2 \left[\langle r \rangle^2 \cos(2q\langle r \rangle) \exp(-2\sigma^2 q^2) + \sigma^2 \cos(2q\langle r \rangle) \cdot (1 - 4\sigma^2 q^2) \exp(-2\sigma^2 q^2) \right], \quad (4.35)$$

where ϕ is the volume fraction, and $\Delta\rho_{\text{SLD}}$ the contrast factor. The final term I_{incoh} is due to small differences in incoherent scattering between the sample and the empty cell. The value of N comes from

$$N = \frac{3\phi}{4\pi\langle r^3 \rangle}, \quad (4.36)$$

where $\langle r^3 \rangle$ is the third moment of the radius, which is given by

$$\langle r^3 \rangle_{\text{Gaussian}} = \langle r \rangle^3 \left[1 + 3 \left(\frac{\sigma}{\langle r \rangle} \right)^2 \right]. \quad (4.37)$$

4.2.3 Scattering of n -Alcohol Aerosols

To characterize the n -alcohol aerosols, i.e. the average particle size $\langle r \rangle$, the distribution width σ , and the volume fraction ϕ , the scattering spectra are fit to scattering from a polydisperse distribution of spheres. Here it is assumed that the droplet size distribution follows either a *Gaussian* or a *Schultz* distribution. For a *Gaussian* distribution of droplets the scattering intensity $I(q)$ is given by

$$I_{\text{Gaussian}}(q) = \frac{3\phi}{4\pi\langle r^3 \rangle_{\text{Gaussian}}} \frac{1}{\sigma\sqrt{2\pi}} \int \exp\left[-\frac{(\langle r \rangle - r)^2}{2\sigma^2}\right] P(q, r) dr, \quad (4.38)$$

where $P(q, r)$ is the particle form factor for spheres

$$P(q, r) = \left[\frac{4\pi(\sin(qr) - qr \cos(qr))}{q^3} \right]^2 (\Delta\rho_{\text{SLD}})^2 \quad (4.39)$$

and where $\Delta\rho_{\text{SLD}}$, the contrast factor, is the difference in scattering length density between the liquid n -alcohol droplet and the surrounding bulk gas phase, the N_2 carrier gas. The aerosol number density is given by

$$N = \frac{3\phi}{4\pi\langle r^3 \rangle}, \quad (4.40)$$

where $\langle r^3 \rangle$, the third moment of r , is given by

$$\langle r^3 \rangle_{Gaussian} = \langle r \rangle^3 \left[1 + 3 \left(\frac{\sigma}{\langle r \rangle} \right)^2 \right]. \quad (4.41)$$

Similar expressions for the scattering intensity from a collection of polydisperse spheres that follow a *Schultz* distribution are given in the literature.⁴⁸

The main difference between the *Gaussian* and *Schultz* distributions is that the former is symmetric about the average particle size $\langle r \rangle$, while the latter is asymmetric and skewed towards larger sizes. As shown in Table 8.3, the differences between the two distributions are small for particles with narrow size distribution, i.e. $\sigma/\langle r \rangle < \sim 0.3$.

⁴⁸ Kotlarchyk and Chen, 1983.

5 Fundamental Basics during Supersonic Nozzle Expansion Experiments

In Chapter 4.1 it is explained how the key unmeasured properties, temperature $T(x)$, condensible partial pressure $p(x)$, and supersaturation $S(x)$ are calculated at every position x in the nozzle. In the following chapter I will discuss how these profiles behave and how they are affected if variables such as the condensible flow rate \dot{m} (Chapter 5.2), or the plenum temperature T_0 are varied (Chapter 5.3). Further, the influence of the used carrier gas is investigated (nitrogen or argon) in Chapter 5.4. This systematic discussion is to train the reader's ability to understand and interpret the results discussed in Chapter 6.

5.1 Flow Profiles

As a gas mixture, consisting of carrier gas and condensible species, flows through the nozzle the gas is expanded and accelerated. Consequently the temperature of the gas mixture drops, or in other words, a temperature gradient in the nozzle arises. As temperature and total pressure correlate, the gas mixture also undergoes a pressure drop during the expansion in the nozzle. To visualize this behavior Figure 5.1 shows exemplarily an expansion experiment for *n*-pentanol with a flow rate of 59 mmol min^{-1} and a plenum temperature of $T_0 = 60^\circ\text{C}$.⁴⁹ During the above mentioned temperature and total pressure drop the condensible species changes its state from the former stable gas state into a meta-stable vapor, and finally, relaxes into the under the new conditions stable state, the liquid. This phase transition releases latent heat into the system and static pressure trace measurements detect this heat addition as a deviation of the condensing pressure trace (Figure 5.1 top, solid line) from the theoretical isentropic expansion of the same gas mixture only without the ability of condensation (the wet theoretical isentrope, Figure 5.1 top, dotted line). The temperature gradient in the nozzle (Figure 5.1, center solid line) decreases up to the position where condensation takes place (here $x \sim 2.6 \text{ cm}$). At this point an increase in temperature of the condensing flow from the theoretical wet isentrope due to the latent heat released by nu-

⁴⁹ Gharibeh *et al.*, 2005.

cleation is detected (Figure 5.1 center, dotted line). Further expansion of the gas mixture continues to decrease the temperature of the gas mixture. Figure 5.1 center also exhibits the partial pressure of the condensible species in the nozzle. The condensible partial pressure decreases during the expansion and at the point of nucleation ($x \sim 2.6$ cm) a sudden rapid decrease in condensible partial pressure is observed. This is due to the strong depletion of the vapor phase during nucleation. The equilibrium vapor pressure is an exponential function of the inverse temperature. And thus, the equilibrium vapor pressure decreases rapidly in the nozzle, much quicker than the decrease of the condensible partial pressure. The supersaturation, given by the ratio of the partial condensible pressure to the equilibrium vapor pressure, increases up to the point of nucleation and reaches a maximum value (Figure 5.1, bottom). The strong depletion of the vapor phase at the nucleation position is accompanied by a decrease in supersaturation. The apparent increase in supersaturation after the nucleation burst is an artifact and not a real event. It is a consequence of boundary layer recompression, i.e. the boundary layer is compressed slightly by the increase in pressure due to the release of latent heat. Thus the pressure measured during the wet condensing flow is lower than it would be if recompression would not occur. While inverting the pressure data the condensate mass fraction is slightly underestimated, which means that the condensible partial pressure doesn't decrease as much as it should and consequently the supersaturation increases.⁵⁰ The normalized nucleation rate profile J/J_{\max} according to CNT is given by a dashed line in Figure 5.1 bottom. The trend of the profile is to some extent similar to that of the supersaturation. The nucleation rate increases up to a maximum value at $x \sim 2.6$ cm and then drops off rapidly. However, the peak of the nucleation profile is much steeper, slimmer and much more pronounced than the supersaturation peak. Further downstream the nucleation rate also increases as the supersaturation increases.

⁵⁰ Paci *et al.*, 2004., Tanimura *et al.*, 2007.

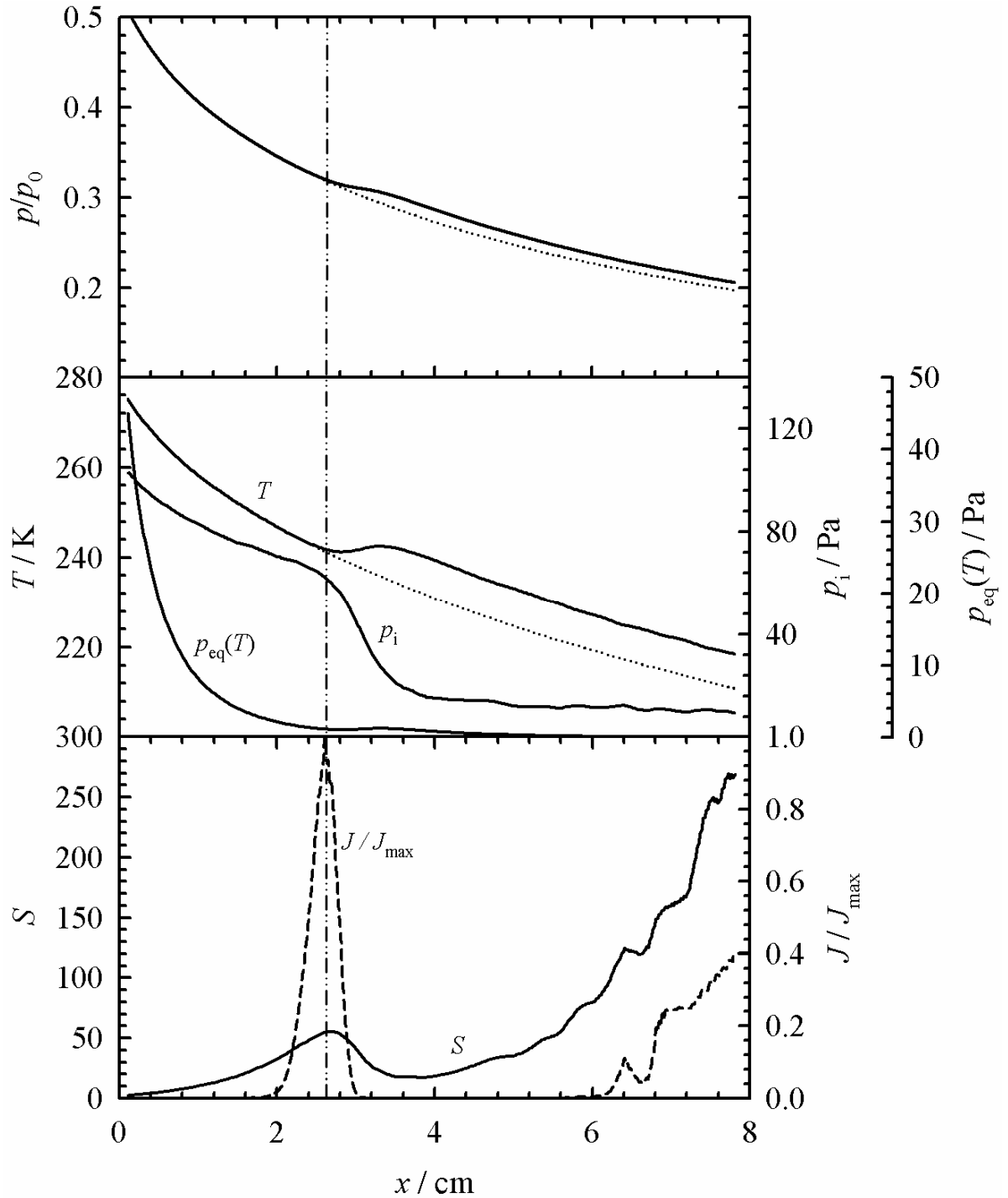


Figure 5.1: The experimentally measured total pressure ratio p/p_0 (top, solid line) and the expansion of an identical gas mixture without the ability of condensation, the theoretical isentrope (top, dotted line), the partial pressure of the condensible p_i (center), the temperature T (center, solid line) and the temperature profile of the theoretical isentrope (center, dotted line), the equilibrium vapor pressure $p_{eq}(T)$ (center), the supersaturation S (bottom, solid line), and the normalized nucleation rate according to Classical Nucleation Theory (bottom, solid line) as a function of the position x in the nozzle for a n -pentanol flow rate of 59 mmol min^{-1} at $T_0 = 60^\circ\text{C}$. The vertical dashed-dotted-dotted line is a reference line corresponding to the maximum nucleation rate condition.

5.2 The Flow Rate of the Condensible Species

Information on the phenomena of nucleation is enhanced by measurements made over a wide range of nucleation rates, temperatures, and supersaturations. To achieve this, a number of parameters can be varied during the experiment. The primary parameter is the flow rate \dot{m} of the condensible species. For low flow rates the critical supersaturation is reached at low pressures and temperatures, thus, the nucleation position shifts further downstream in the nozzle while for high flow rates the critical supersaturation is inherently reached at higher pressures and temperatures, and thus, the nucleation position shifts further upstream. An example is shown in Figure 5.2:⁵¹ Decreasing the flow rate for *n*-propanol at a plenum temperature of $T_0 = 50^\circ\text{C}$ from $248 \text{ mmol min}^{-1}$ to 68 mmol min^{-1} shifts the nucleation position from $x = 2.0 \text{ cm}$ to $x = 4.7 \text{ cm}$ downstream.

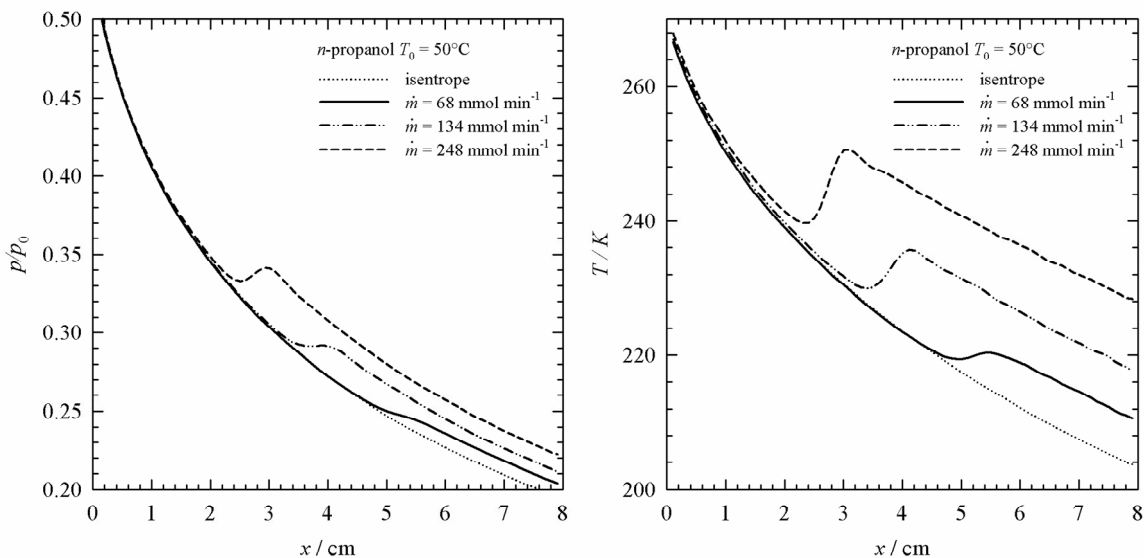


Figure 5.2: The reduced total pressure ratio p/p_0 (left) and temperature T (right) vs. the nozzle position x for a series of *n*-propanol flow rates at a plenum temperature of $T_0 = 50^\circ\text{C}$.

The occurring nucleation at a given plenum temperature T_0 for various condensible flow rates \dot{m} does not only take place at different pressures, temperatures, and supersaturations but is also sensitive to the expansion rate. Since this work uses a Laval nozzle (opening angle = const.; $d(A/A^*) = \text{const.}$) the expansion rate ($d(p/p_0)/dt \neq \text{const.}$) is sensitive to the nucleation position in the nozzle. Consequently, the occurring nucleation itself is also affected by the nucleation position in the nozzle. Figure 5.3 illustrates the expansion rate

⁵¹ Gharibeh *et al.*, 2005.

at the maximum nucleation position for two *n*-propanol flow rates, 248 mmol min⁻¹ and 68 mmol min⁻¹, at $T_0 = 50^\circ\text{C}$. For this the pressure ratio p/p_0 is plotted vs. the time. Here the unit of the abscissa has been transformed from a position to a time scale as described by equation (4.27). Nucleation occurring further upstream in the nozzle shows higher values for the negative expansion rate $-d(p/p_0)/dt$. The value for the negative expansion rate indicates how steep the system is probing the meta-stable regime in terms of pressure per unit time at the maximum nucleation position. For strong declining expansion rates the condensible species crosses its equilibrium vapor pressure line and probes the meta-stable vapor state with a sharp decline. Consequently, states of higher nucleation rates for the relaxation are reached. Simultaneously we will see that large values for the negative expansion rate correspond to small characteristic times (Figure 6.17).

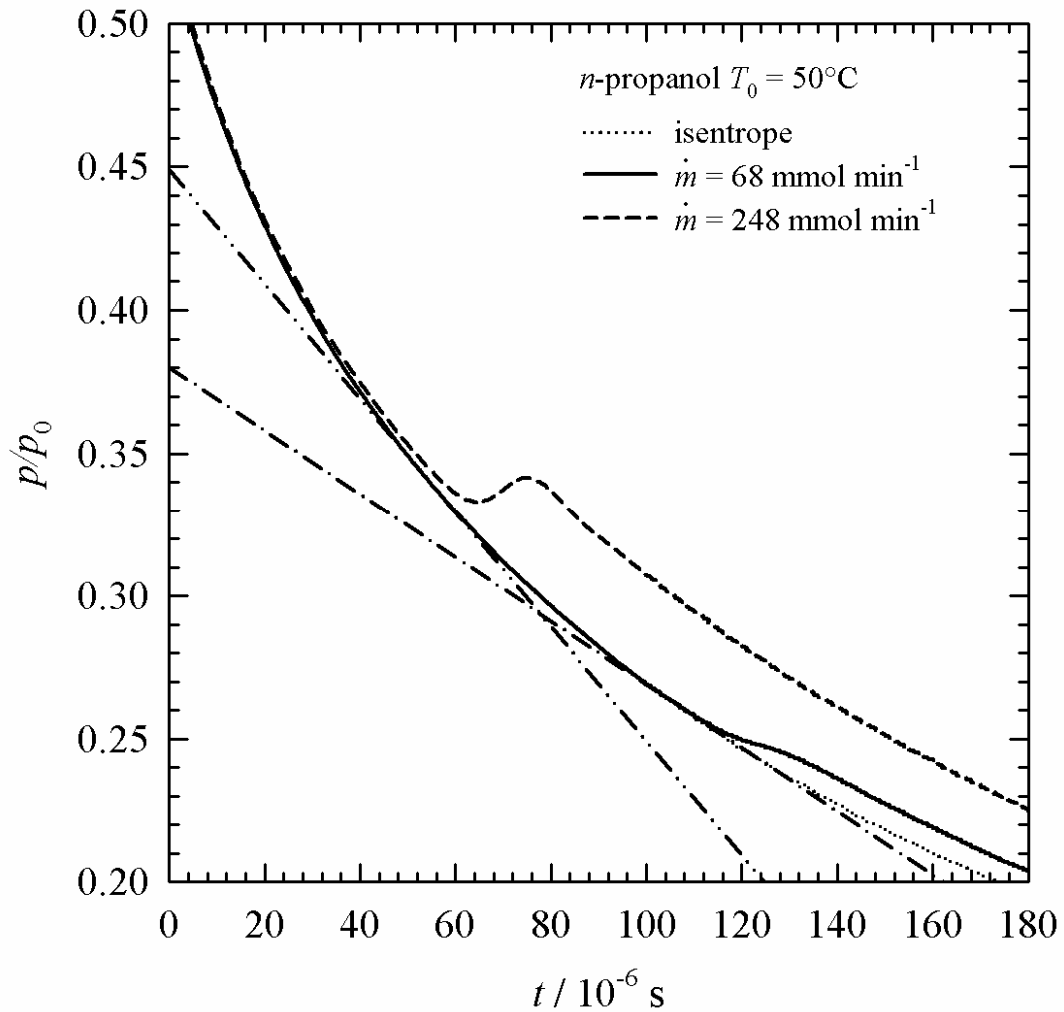


Figure 5.3: The pressure ratio p/p_0 vs. the time t for two *n*-propanol flow rates, 248 mmol min⁻¹ (dashed line) and 68 mmol min⁻¹ (solid line), at a plenum temperature of $T_0 = 50^\circ\text{C}$. The dashed-dotted-dotted line and the dashed-dotted line represent the tangent at the nucleation position, respectively.

5.3 The Stagnation Temperature

It is not possible to decrease or increase the flow rate of the condensible species m at a given stagnation temperature to an arbitrary value. If the chosen flow rate at a given stagnation temperature is too low, condensation would not occur in the nozzle. Using a longer nozzle would only delay the problem. If the chosen flow rate at a given stagnation temperature is too high, the condensible species would already be supersaturated in the plenum and condense. To prevent these two phenomena the stagnation temperature T_0 can be varied depending upon the flow rate of interest. Decreasing the stagnation temperature shifts the nucleation position further upstream, and thus, allows us to measure low flow rates of the condensible species. Increasing the stagnation temperature increases the equilibrium vapor pressure in the plenum; i.e. condensation in the plenum is prevented, and furthermore, the nucleation position shifts further downstream in the nozzle and allows us to measure high flow rates. Figure 5.4 illustrates an example for a flow rate of $67.5 \text{ mmol min}^{-1}$ of *n*-propanol at a stagnation temperature of $T_0 = 35^\circ\text{C}$ and $T_0 = 50^\circ\text{C}$.⁵² For a stagnation temperature of $T_0 = 35^\circ\text{C}$ the nucleation position is at $x = 2.5 \text{ cm}$. Increasing the stagnation temperature by 15 K to $T_0 = 50^\circ\text{C}$ shifts the nucleation position 2.2 cm downstream to $x = 4.7 \text{ cm}$. Figure 5.4 bottom left and right illustrate the expansion and the cooling rate at the maximum nucleation position for an *n*-propanol flow rate of $67.5 \text{ mmol min}^{-1}$ at a stagnation temperature of $T_0 = 35^\circ\text{C}$ and $T_0 = 50^\circ\text{C}$. Here the unit of the abscissa has been transformed as described by equation (4.27). Lower stagnation temperatures shift the nucleation position further upstream. Here the expansion rate $-d(p/p_0)/dt$ and the cooling rate $-d(T/T_0)/dt$ are large. Consequently, the condensible species crosses its equilibrium vapor pressure line and probes the meta-stable vapor state with a sharp decline so that states of higher nucleation rates for the relaxation are reached.

⁵² Gharibeh *et al.*, 2005.

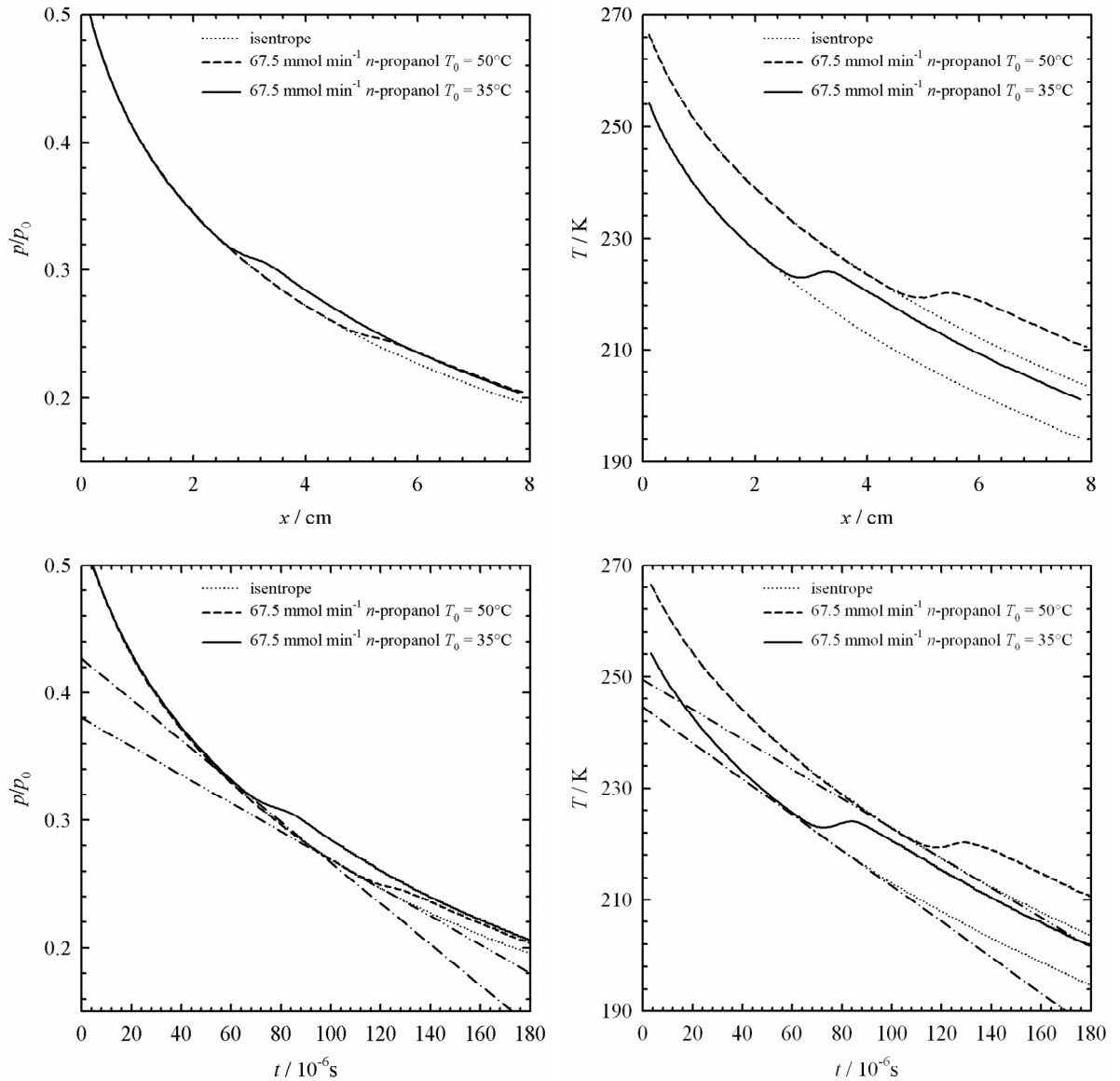


Figure 5.4: The reduced total pressure ratio p/p_0 (top left) and the temperature T (top right) vs. the position x in the nozzle for $67.5 \text{ mmol min}^{-1}$ n -propanol at a stagnation temperature of $T_0 = 35^\circ\text{C}$ (solid line) and $T_0 = 50^\circ\text{C}$ (dashed line). The identical experiments, only with a transformed abscissa (time) are given in the left and right bottom figure. The dashed-dotted and the dashed-dotted-dotted lines correspond to the respective tangents at the maximum nucleation condition.

5.4 The Effect of Carrier Gas

As the thermostat has its limits for cooling the plenum and the gas flow (water bath $\sim 6^\circ\text{C}$), it is not possible to continue decreasing the flow rate of the condensible species to an arbitrary small value. Furthermore, as the investigation within one class of compounds progresses, e.g. for the n -alkanes as also shorter chained n -alkanes like n -heptane with higher equilibrium vapor pressures are of further interest, a complication occurs. In order for

nucleation to occur very low temperatures in the nozzle have to be achieved. However, it is not as simple as to lower the plenum temperature, since the condensible substance would simply condense in the plenum. In such cases it is wise to switch the carrier gas from nitrogen to argon. Nitrogen with $\gamma = 7/5$, compared to Argon with $\gamma = 5/3$, has the ability to store heat in the two additional degrees for rotation and one degree for vibration. Consequently, when using Nitrogen the gas stream does not cool down as rapidly as with Argon. Figure 5.5 top left exhibits a pressure trace in nozzle C with nitrogen and argon at $T_0 = 15^\circ\text{C}$. When using Ar lower pressures are reached at a given nucleation position compared to N_2 as carrier gas. The reason is quite obvious when observing Figure 5.5 top right. Argon as carrier gas cools down in the nozzle much more rapidly compared to nitrogen, and since pressure and temperature correlate the pressure profile of argon must lie below that of N_2 . Using nitrogen as carrier gas a nozzle exit temperature of 164 K is reached. When switching to argon as carrier gas the nozzle exit temperature is reduced to 127 K. Consequently, a shifting of the nucleation position is accompanied by switching between different carrier gases. And since the expansion rate ($d(p/p_0)/dt \neq \text{const.}$) and cooling rate ($d(T/T_0)/dt \neq \text{const.}$) are sensitive to the nucleation position in the nozzle the occurring nucleation is effected by switching between the carrier gases. Figure 5.5 bottom left and right illustrate the expansion and the cooling rate for a hypothetical nucleation temperature of 180 K. Here the unit of the abscissa has been transformed as described by equation (4.27). When using Argon as carrier gas, the nucleation position is reached further upstream in the nozzle at higher pressures. Here the expansion rate $-d(p/p_0)/dt$ and the cooling rate $-d(T/T_0)/dt$ are larger and the condensible species crosses its equilibrium vapor pressure line and probes the meta-stable vapor state with a sharp decline. As the system probes further into the meta-stable regime, states of higher nucleation rates for the relaxation are reached. This is similar to switching between different nozzles with various opening angles ($d(A/A^*) = \text{const.}$).⁵³

⁵³ Kim *et al.*, 2004.

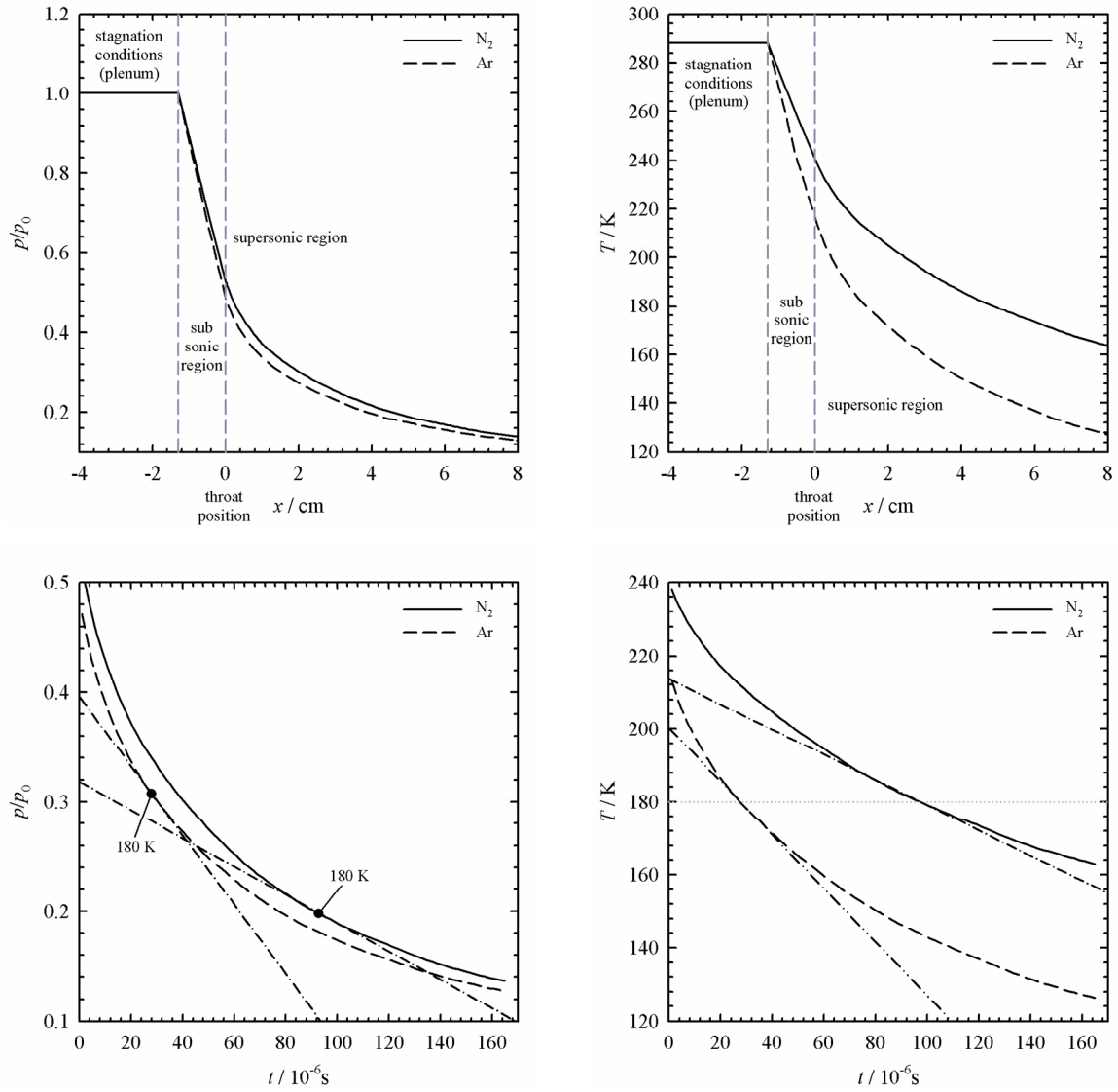


Figure 5.5: The reduced total pressure ratio p/p_0 (top left) and the temperature T (top right) vs. the position x in the nozzle for a pure nitrogen (solid line) and a pure argon expansion (dashed line) at $T_0 = 50^\circ\text{C}$ and $p_0 = 30.2$ kPa. The identical experiments, only with a transformed abscissa (time) are given in the left and right bottom figure. The dashed-dotted and the dashed-dotted-dotted lines correspond to the respective tangents at the temperature $T = 180$ K.

6 Results and Discussion

This chapter will proceed as follows: First, the results of the Small Angle X-ray Scattering experiments of the n -alcohols will be presented. This section builds up on our earlier publication.⁵⁴ Second, the influence of the temperature dependent heat capacity is investigated on n -nonane expansion experiments available from literature.⁵⁵ Then, the results of n -alkane pressure trace measurements are shown. Fourth and final, the Small Angle X-ray Scattering results of the n -alkane aerosols will be presented and discussed.

6.1 Small Angle X-ray Scattering of n -Alcohol Droplets

Small Angle X-ray Scattering experiments at a fixed position, $x = 6.5$ cm downstream of the throat, were conducted of n -propanol, n -butanol, and n -pentanol aerosols in nozzle H2. During these experiments the n -alcohol flow rate \dot{m} was varied. All condensation experiments were performed at a stagnation pressure $p_0 = 30.2 \pm 0.02$ kPa and stagnation temperatures T_0 that ranged from 35°C - 60°C depending on the n -alcohol. Figure 6.1 illustrates the radially averaged x-ray spectra for droplets formed from n -butanol in expansions with $T_0 = 50^\circ\text{C}$, $p_0 = 30.2$ kPa, and n -butanol flow rates between 32.1 mmol min⁻¹ and 107.9 mmol min⁻¹. The spectrum for 32.1 mmol min⁻¹ is at the absolute intensity scale, determined by comparing D₂O SAXS spectra to D₂O SANS spectra previously measured using the NG7-SANS instrument at the NIST Center for Neutron Research,⁵⁶ while the spectra at higher flow rates are offset by factors of 4, 16, 256, and 4096, respectively. The error bars, based on count statistics, have been omitted for clarity. Below $q = 1$ nm⁻¹ the error is less than 1% of the signal and for $q > 1$ nm⁻¹ the error is generally less than 5% of the signal (Figure 6.2).

⁵⁴ Gharibeh *et al.*, 2005.

⁵⁵ Wagner and Strey, 1984; Viisanen, Wagner, and Strey, 1998.

⁵⁶ Wyslouzil, Strey, and Wilemski, 2007.

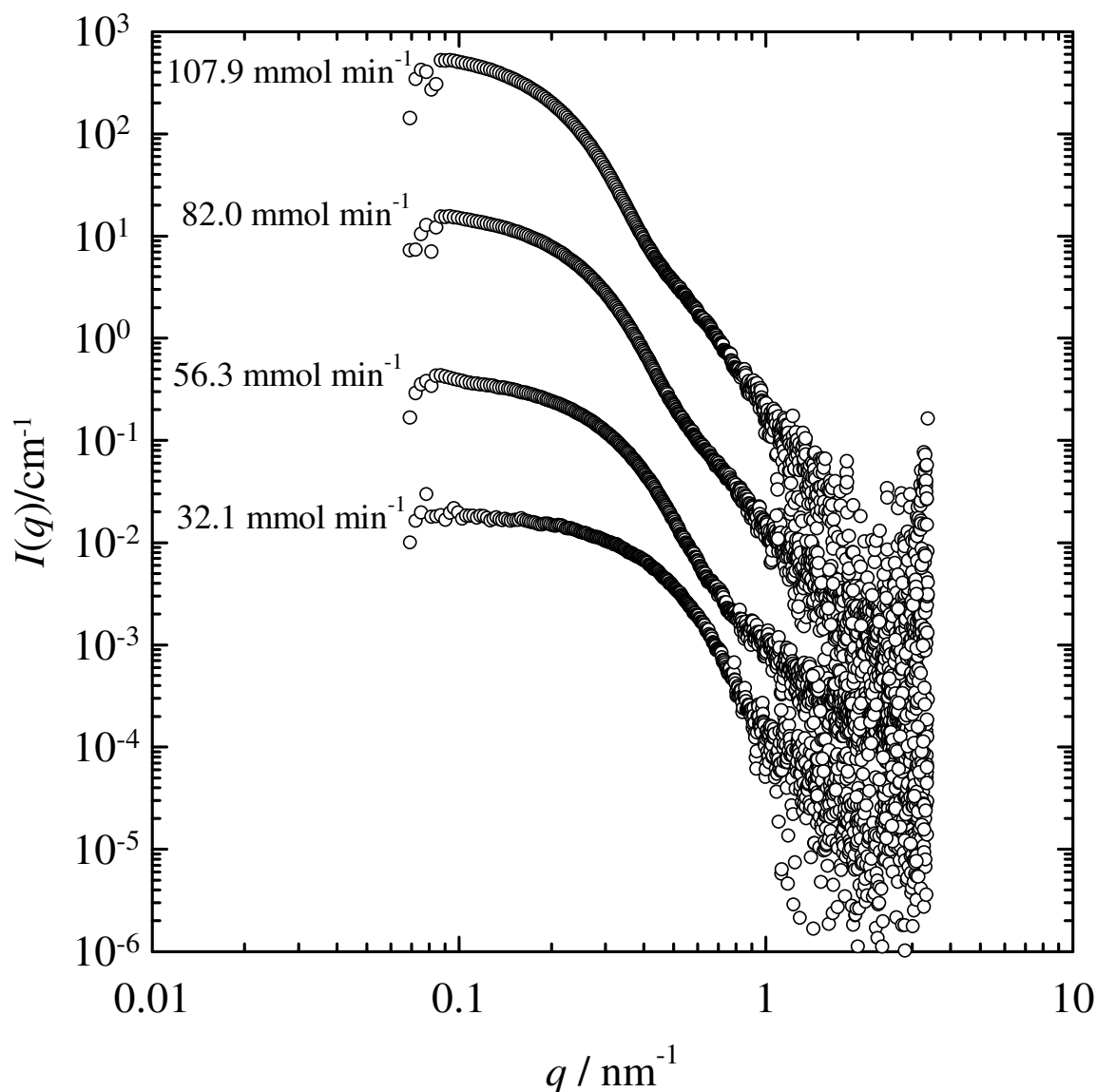


Figure 6.1: All one-dimensional *n*-butanol SAXS spectra in this figure are measured at $T_0=50^\circ\text{C}$ and $p_0=30.2\text{ kPa}$. The spectrum for $32.1\text{ mmol min}^{-1}$ of *n*-butanol is at the true absolute intensity scale. The spectra at higher flow rates are offset by factors of 4, 16, 256, and 4096, respectively. For clarity error bars are omitted. Below $q = 1\text{ nm}^{-1}$ the error is less than 1% of the signal. For $q > 1\text{ nm}^{-1}$ the error is generally less than 5% of the signal.

As illustrated in Figure 6.1, at high flow rates the data cover ~ 5 orders of magnitude in intensity over the accessible range of the scattering vector q . As the flow rate decreases, the inflection point in the intermediate q range moves to larger q values, an indication of a decrease in the average particle size. In the high q region, the intensity decreases as q^{-4} , a feature characteristic for scattering from a polydisperse distribution of spheres.

One of the major advantages of SAXS, compared to earlier Small Angle Neutron Scat-

tering work⁵⁷ is that these measurements were conducted with normal, hydrogenated compounds rather than expensive deuterated ones. Furthermore, the high photon flux available at synchrotron sources has reduced the time required to obtain highly resolved spectra by about 3 orders of magnitude. Finally, because the speed of the x-rays (speed of light) is so much higher than the speed of the aerosols (~500 m/s), a Doppler shift is not observed in the scattering pattern and the data analysis is, therefore, more straightforward.⁵⁸

The mean radius $\langle r \rangle$, the width of the size distribution function σ , and the particle number density N are determined by fitting each spectrum to scattering from a polydisperse distribution of spheres. In this thesis the sensitivity of the parameters derived to the underlying size distribution is tested by fitting to both *Gaussian* and *Schultz* distribution functions. Figure 6.2 illustrates a typical *Gaussian* fit to one of the *n*-butanol spectra, and Table 8.3 summarizes all of the fit results. In most cases there are no significant differences between the values of $\langle r \rangle$ (< 5%), σ (< 10%), or N (< 5%) obtained for the two distributions. The polydispersity $\sigma/\langle r \rangle$ is usually lower for the *Schultz* distributions, and, generally, the differences are most pronounced for the smallest droplets.

⁵⁷ Wyslouzil *et al.*, 1999; Wyslouzil, Wilemski, and Strey, 2000b; Heath *et al.*, 2003; Khan *et al.*, 2003; Kim *et al.*, 2004.

⁵⁸ Wyslouzil *et al.*, 1999.

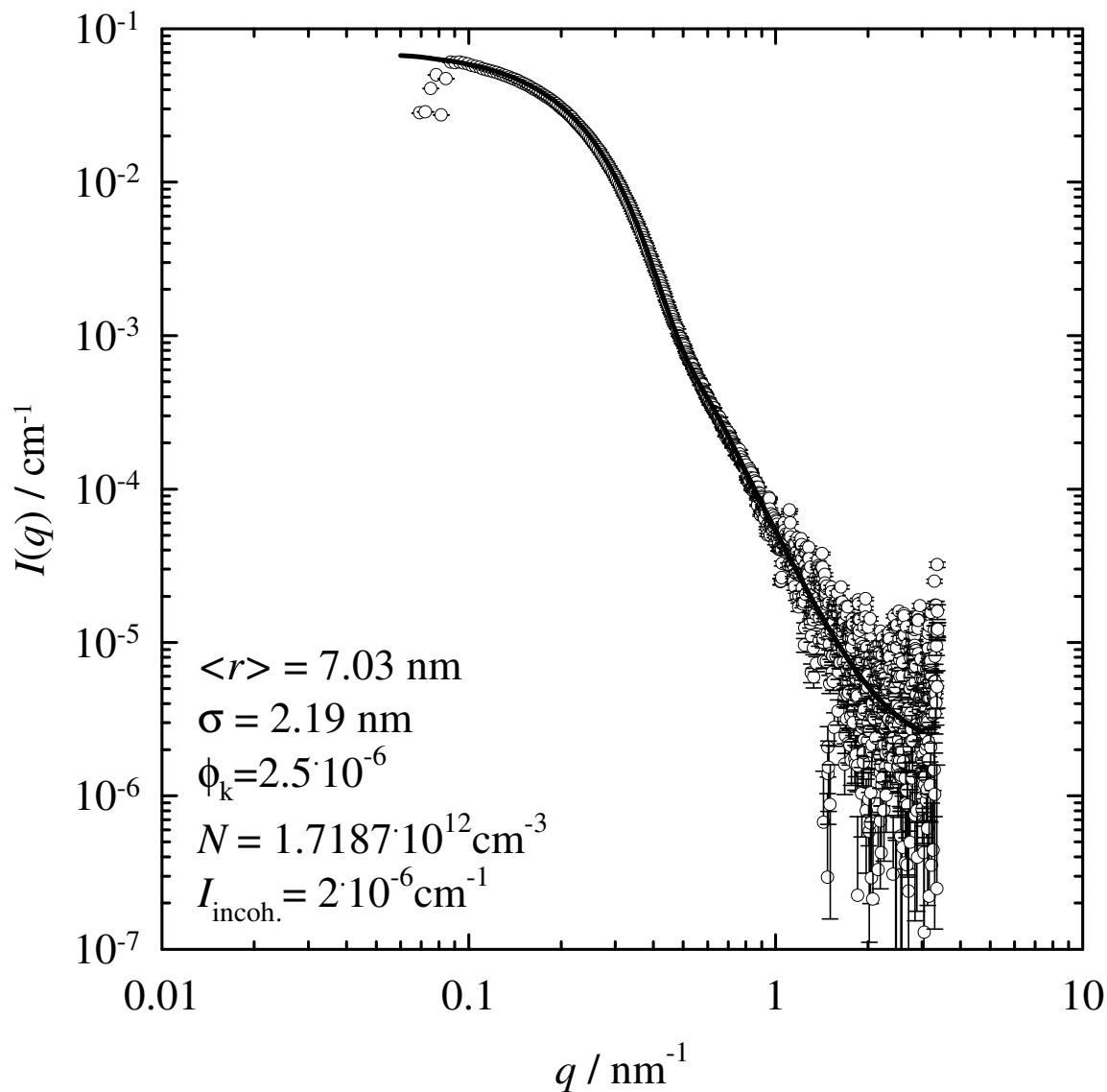


Figure 6.2: The one-dimensional SAXS spectrum of $82.0 \text{ mmol min}^{-1}$ *n*-butanol at a plenum temperature of $T_0=50^\circ\text{C}$ and pressure of $p_0=30.2 \text{ kPa}$. The symbols correspond to the SAXS measurement, while the solid line indicates the fit curve. The fit curve is calculated assuming a polydisperse *Gaussian* distribution of spheres. During these experiments the incoherent background is generally $1 \cdot 10^{-6} < I_{\text{incoh.}} / \text{cm}^{-1} < 10 \cdot 10^{-6}$.

The variations in the size distribution parameters (*Gaussian* fits) with the *n*-alcohol flow rate are summarized in Figure 6.3 (*n*-propanol), Figure 6.4 (*n*-butanol), and Figure 6.5 (*n*-pentanol). For each *n*-alcohol a rapid increase in the mean radius $\langle r \rangle$ with the condensable flow rate \dot{m} is found. This increase is expected because the concentration of condensable vapor is directly proportional to \dot{m} , the reservoir. If the particle number density N and the fraction of vapor that condenses are constant, a simple volumetric balance shows that $\langle r \rangle \propto \sqrt[3]{\dot{m}}$. In Figure 6.3 the solid black line illustrates this trend for a particle number

density $N = 10^{12} \text{ cm}^{-3}$. The experimental data follow the simple scaling law at high flow rates where $N \approx 10^{12} \text{ cm}^{-3}$, however deviate at low flow rates as N increases rapidly. Clearly as N increases with decreasing n -alcohol flow rate this simple scaling overestimates the particle radius $\langle r \rangle$. When N increases for decreasing condensible concentration, $\langle r \rangle$ must decrease as $(10^{12}/N_{\text{obs}})^{1/3}$. This trend is given by the dashed line in Figure 6.3 and a rather good agreement is found between the measured radii and this simple scaling. Finally, the droplet size (squares in Figure 6.3 - Figure 6.5) observed at a fixed position in the nozzle does not only depend on the the n -alcohol flow rate but also on the length of time available for droplet growth. Droplets formed further upstream have a longer time of flight before they reach the fixed observation point compared to those formed further downstream in the nozzle. In a supersonic nozzle, the position corresponding to the maximum particle formation rate moves closer to the throat, i.e. further from the observation point, as the stagnation temperature T_0 decreases or as the flow rate of the condensible increases (Chapter 5.2 - 5.3). Thus, at a fixed condensible flow rate, particles formed in expansions starting from a lower T_0 will have a longer growth time and should be slightly larger, a trend that is confirmed by the data in Figure 6.3 – Figure 6.5. Since the changes in $\langle r \rangle$ with T_0 are only on the order of 3%, it is concluded that this effect is not dominant for these experiments.

The deviation between the scaling law, which takes the non constancy of the particle number density into account $N \neq \text{const.}$ (black dashed line) and the measured radii depends on the stagnation temperature and the condensible flow rate for a measurement set of constant plenum temperature. Understandably in both cases, decreasing plenum temperature and increasing flow rate, increase the growth time for the aerosols, and thus, deviations between the simple mass balance (black dashed line) are propagated.

Over the range of measured n -alcohol flow rates the mean radius $\langle r \rangle$ and the width of the size distribution σ (triangles in Figure 6.3 - Figure 6.5) both increase by factors of 2 - 2.5. For fits to the *Schultz* distribution, the polydispersity $\sigma/\langle r \rangle$ is remarkably constant at $\sigma/\langle r \rangle = 0.26 \pm 0.01$, while for the *Gaussian* fits $\sigma/\langle r \rangle$ ranges from $\sigma/\langle r \rangle \approx 0.3$ for the smallest drops decreasing to $\sigma/\langle r \rangle \approx 0.25$ for the largest drops. At a fixed n -alcohol flow rate, the values of σ for different values of T_0 differ by up to 15%, and the lowest values of σ correspond to the highest values of T_0 .

In contrast to the mean radius $\langle r \rangle$ and the width of the size distribution σ , the particle number density N (circles in Figure 6.3 - Figure 6.5) decreases rapidly, by up to a factor of

4, as the n -alcohol flow rate increases. At a fixed n -alcohol flow rate, the particle number densities lie within $\sim 20\%$ of each other and the lowest values of N correspond to the lowest T_0 . The increase in N with decreasing flow rate may be understood in the following way: Decreasing flow rates shift the nucleation position further downstream in the nozzle to low temperatures and high supersaturations. High supersaturation, in turn, means a stronger driving force for the nucleation, and thus, a larger particle production rate $\int J(S,T)dt$. Thereto, downstream condensation entails small values for the negative expansion rate $-\dot{p}/p_0 = -(dp/dt)/p_0$. Small values of the negative expansion rate correspond to a large characteristic time $\Delta t_{J_{\max}}$ (see Figure 6.17). At the same time, in the supersonic nozzle, the nucleation pulse occurs because particle growth depletes the vapor phase and quenches particle formation. Decreasing the n -alcohol flow rate also corresponds to a decreasing vapor phase concentration. Lower vapor phase concentrations and lower temperatures both decrease the impingement rate of monomer onto the growing drop, and thus, should act to slow down the self quenching process. A longer characteristic time $\Delta t_{J_{\max}}$ (in both cases) in turn, should give rise to higher particle number densities N as long as the nucleation rate does not decrease too rapidly. Consequently more subcritical and critical clusters can be formed which continue to grow. The change in N with T_0 is most likely due to differences in the gas density at the observation point and due to a small degree of coagulation between the position of particle formation and the observation point, and also because of the fact that the nucleation position shifts in respect to the plenum temperature.

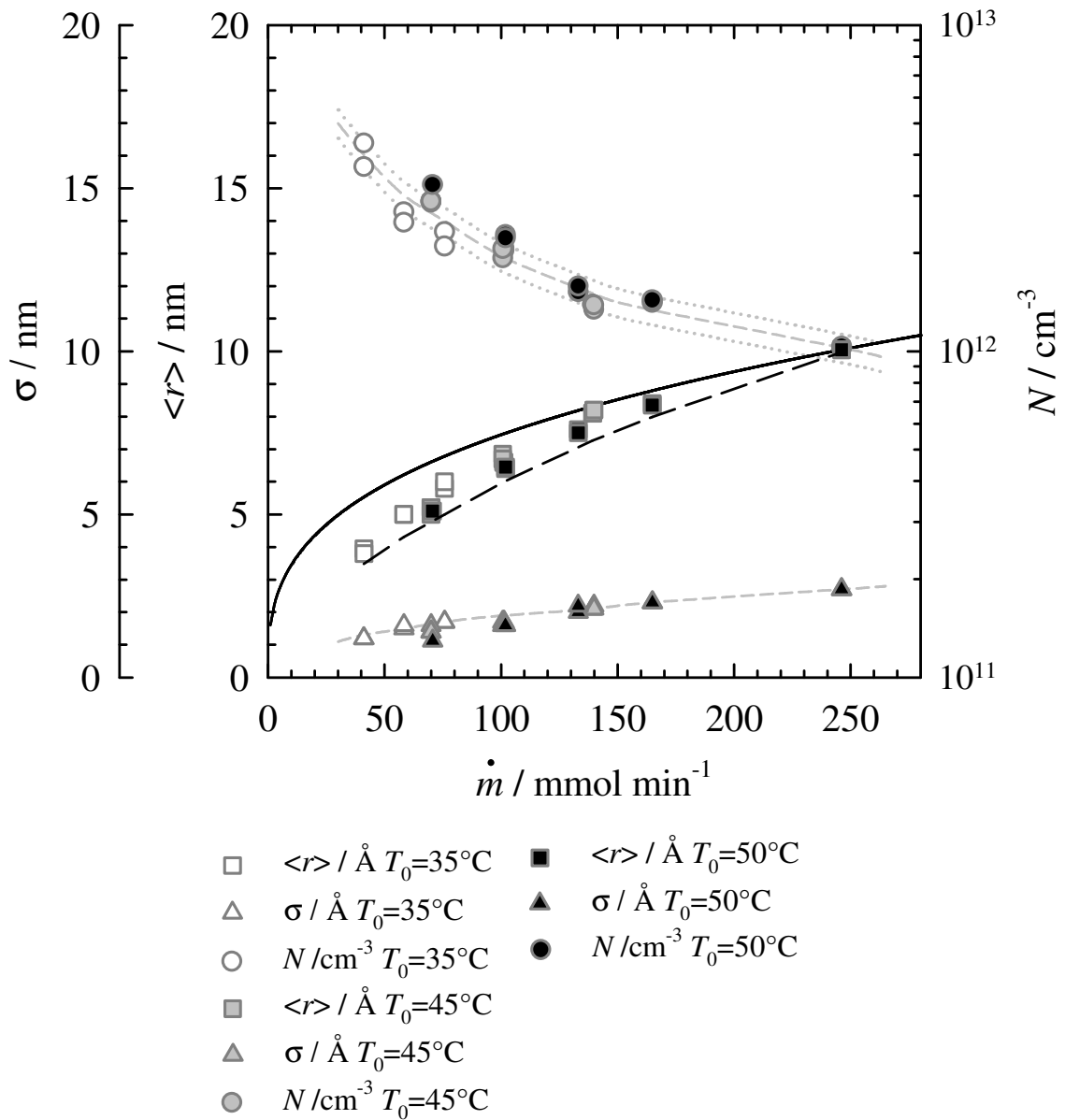


Figure 6.3: The mean radius (squares), the width of the size distribution function (triangles) and the particle number density (circles) as a function of the flow rate for *n*-propanol at $T_0=35^\circ\text{C}$ (light coloured), $T_0=45^\circ\text{C}$ (grey coloured) and $T_0=50^\circ\text{C}$ (dark coloured). The Small Angle X-ray Scattering signal has been analyzed assuming a *Gaussian* distribution of droplets. The grey dashed lines are intended to guide the eye. The grey dotted lines indicate a 10% deviation of the particle number density. The black solid line indicates the growth behavior of the radius as a function of the flow rate assuming a constant particle number density of $N=1\cdot 10^{12}\text{cm}^{-3}$ and that the mean radius scales with $\sqrt[3]{\dot{m}}$. The black dashed line indicates the growth behavior of the radius as a function of the flow rate taking into account the flow rate dependency of the particle number density.

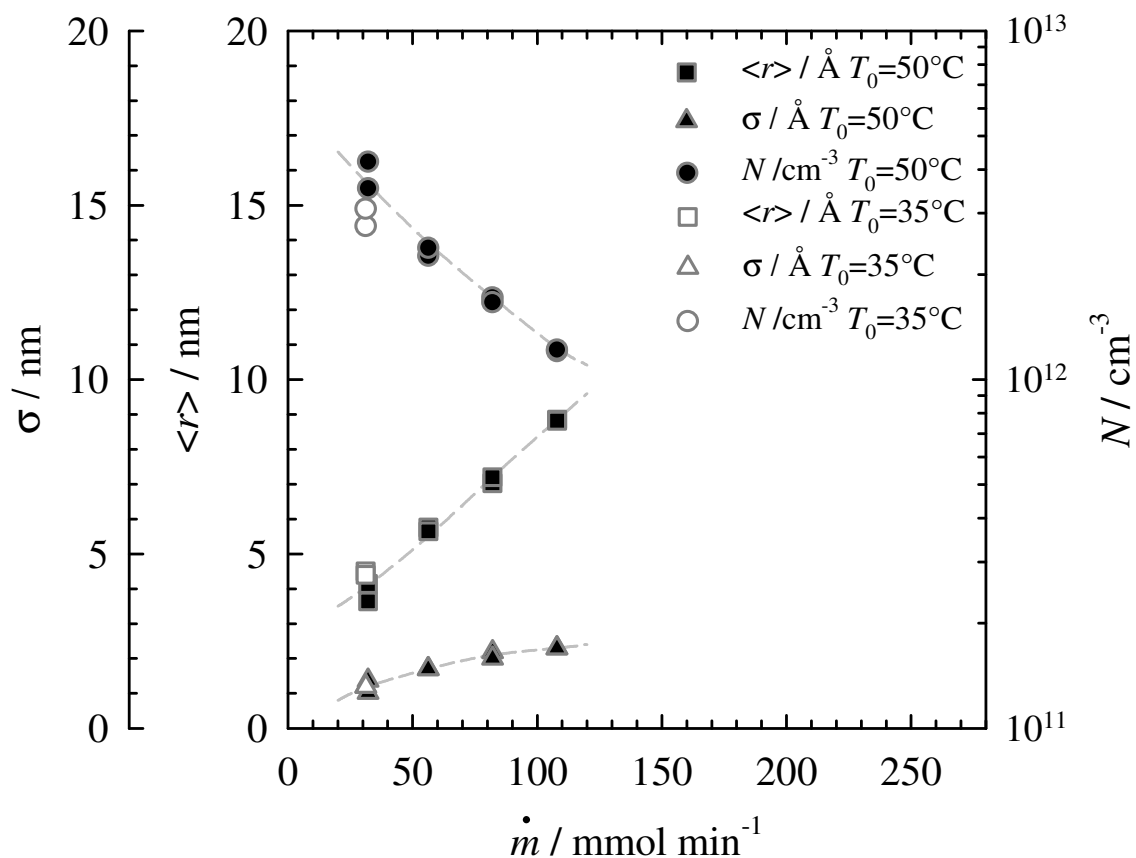


Figure 6.4: The mean radius (squares), the width of the size distribution function (triangles) and the particle number density (circles) as a function of the flow rate for *n*-butanol at $T_0=35^\circ\text{C}$ (light coloured) and $T_0=50^\circ\text{C}$ (dark coloured). The Small Angle X-ray Scattering signal has been analyzed assuming a Gaussian distribution of droplets. The dashed lines are intended to guide the eye.

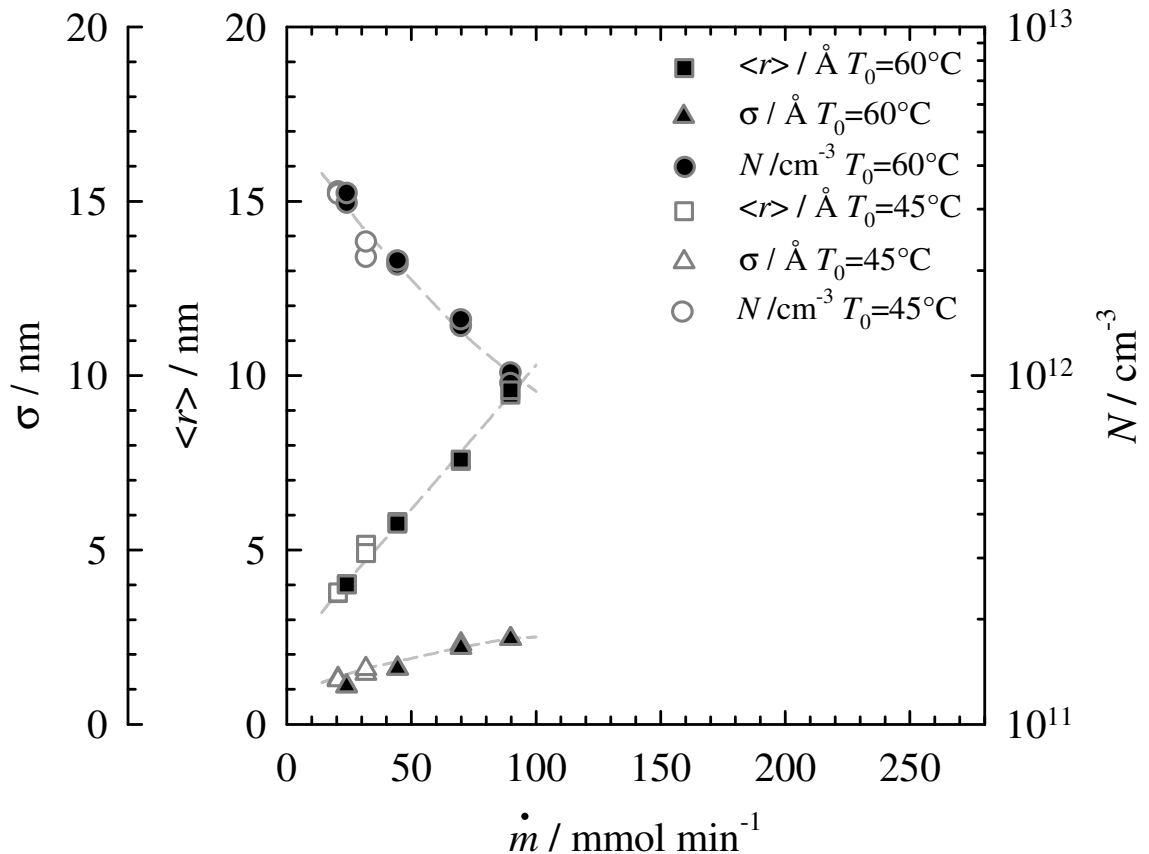


Figure 6.5: The mean radius (squares), the width of the size distribution function (triangles) and the particle number density (circles) as a function of the flow rate for *n*-pentanol at $T_0=45^\circ\text{C}$ (light coloured) and $T_0=60^\circ\text{C}$ (dark coloured). The Small Angle X-ray Scattering signal has been analyzed assuming a Gaussian distribution of droplets. The dashed lines are intended to guide the eye.

Figure 6.6 exhibits the mean radius (squares) and the width of the size distribution function (triangles) for *n*-propanol (white), *n*-butanol (grey) and *n*-pentanol (dark) as a function of the *n*-alcohol flow rate (*Gaussian* fit). At a given flow rate the mean radius and the width of the size distribution increase as the *n*-alcohol chain length increases. The increase in the mean radius with increasing *n*-alcohol chain length can be understood, or at least in part, first by the fact that at a given plenum temperature and molar flow rate the nucleation position moves further upstream as the *n*-alcohol chain length increases. Longer chained *n*-alcohols have a smaller equilibrium vapor pressure, and thus, the critical supersaturation is reached at higher temperatures, i.e. further upstream. This upstream shift and the adjunctive increase in the available time of growth up to the detection position $x = 6.5$ cm downstream of the throat is the dominant factor. Second and not dominant, the increasing *n*-alcohol chain length is conjoint with an increase in molecular volume which implicates a

larger cluster radius.

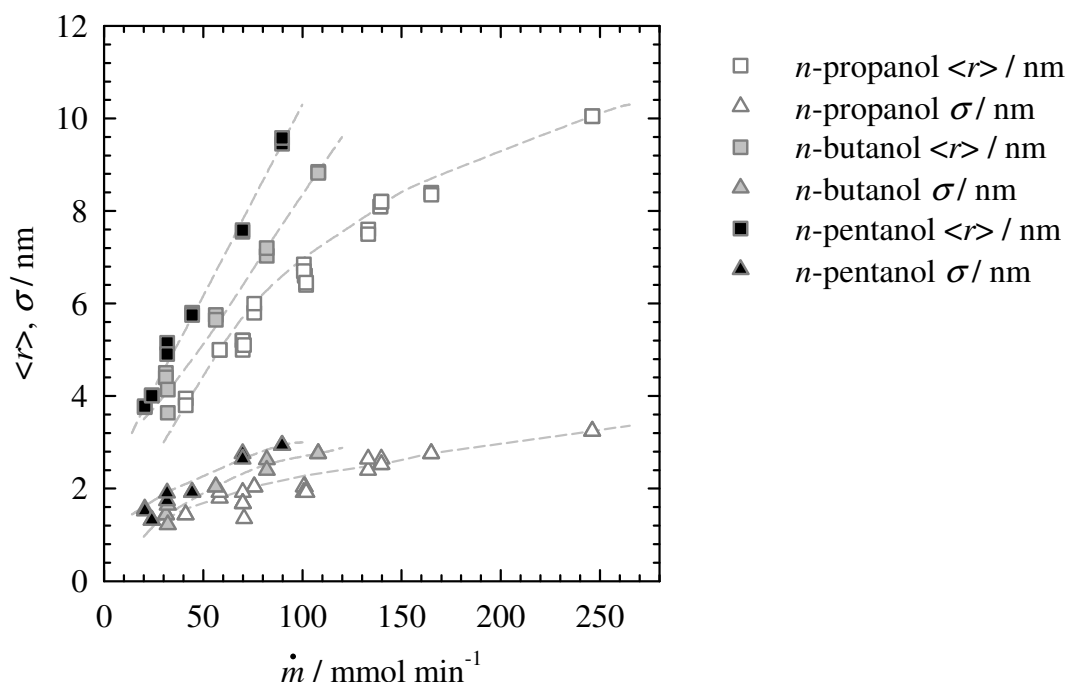


Figure 6.6: The mean radius (squares) and the width of the size distribution function (triangles) for *n*-propanol (white), *n*-butanol (grey), and *n*-pentanol (dark) as a function of the flow rate. The Small Angle X-ray Scattering signal has been analyzed assuming a *Gaussian* distribution of droplets. The dashed lines are intended to guide the eye.

Figure 6.7 exhibits the particle number density for *n*-propanol (white), *n*-butanol (grey) and *n*-pentanol (dark) on a log-log scale as a function of the *n*-alcohol flow rate (*Gaussian* fit). The particle number density decreases at a given molar flow rate as the *n*-alcohol chain length increases. This can be understood by the following: At a given molar flow rate and plenum temperature the nucleation position is shifted further upstream as the *n*-alcohol chain length increases which is conjoint with an increase in nucleation temperature. As the supersaturation is an exponential function of the inverse temperature it decreases as the *n*-alcohol chain length increases. Lower supersaturation, in turn, means a smaller driving force for the nucleation and a smaller particle production rate $\int J(S, T) dt$. Thereto, a large negative expansion rate $-\dot{p}/p_0 = -(dp/dt)/p_0$ corresponds to a shorter characteristic time. A shorter characteristic time, e.g. shorter nucleation bursts, in turn means a decrease in the particle number density N .

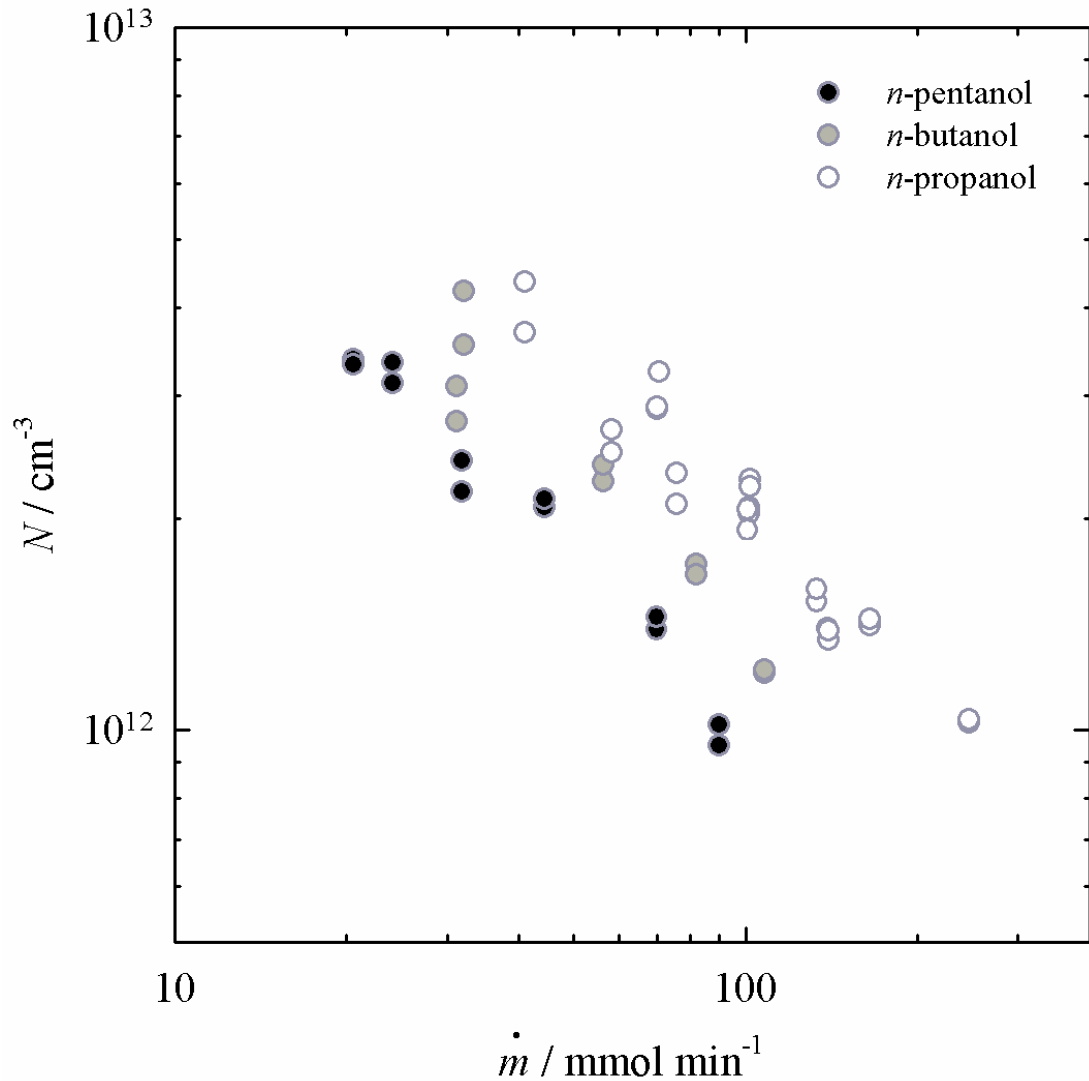


Figure 6.7: The particle number density for *n*-propanol (white), *n*-butanol (grey) and *n*-pentanol (dark) as a function of the flow rate. The Small Angle X-ray Scattering signal has been analyzed assuming a *Gaussian* distribution of droplets.

The main purpose of our research is to measure the maximum nucleation rate during condensation in our supersonic nozzle. Ideally, the thermodynamic and SAXS measurements should be conducted using the same nozzle under identical operating conditions. The previous thermodynamic⁵⁹ measurements were conducted in nozzle A which has a linear opening angle of $d(A/A^*)/dx = 0.0486 \text{ cm}^{-1}$, where A/A^* is the area ratio and A^* is the area of the throat. The nozzle used for this set of SAXS experiments, nozzle H2, has a linear opening angle of $d(A/A^*)/dx = 0.054 \text{ cm}^{-1}$. The opening angle is obtained by fitting the area ratio between $x = 2$ and $x = 7$ cm. Figure 6.8 compares a pressure trace measurement

⁵⁹ Gharibeh *et al.*, 2005.

and the area ratio A/A^* of these two nozzles for a pure nitrogen expansion at $p_0 = 59.6$ kPa and $T_0 = 35^\circ\text{C}$.

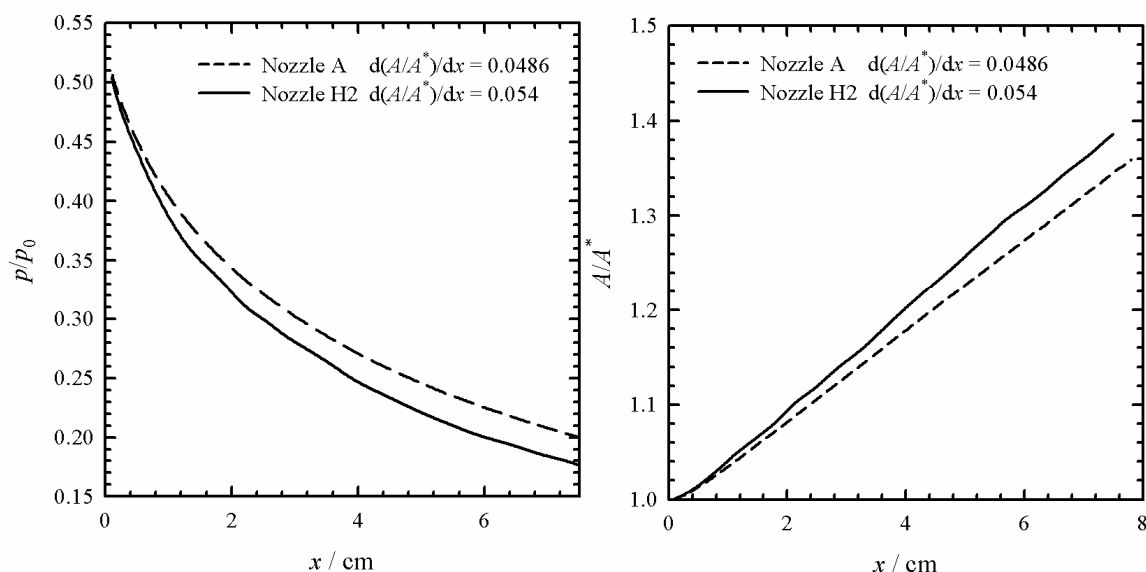


Figure 6.8: The pressure ratio (left) and the area ratio (right) of nozzle A and nozzle H2 at $p_0=59.6$ kPa and $T_0=35^\circ\text{C}$ using pure nitrogen.

To combine the SAXS and the pressure trace measurements first the measured particle number densities N have to be corrected for the difference in opening angle between nozzle H2 and nozzle A. To do this I rely on extensive particle number density measurements made by *Kim et al.*⁶⁰ for D_2O droplets formed in three nozzles, including nozzle A, with expansion rates that bracket that of nozzle H2. Figure 6.9 illustrates the particle number densities *Kim et al.*⁶⁰ measured as a function of the molar flow rate of D_2O for nozzle A (circles), B (squares), and C (triangles). Based on these data the estimated correction for the difference in the expansion rate between nozzle H2 (black dashed line) and nozzle A is a 15% decrease of the measured particle number densities. Further, it is then possible to correlate the corrected number densities as a function of flow rate in order to obtain the values of N corresponding to the thermodynamic data, and finally, to calculate the nucleation rate.

⁶⁰ Kim et al., 2004.

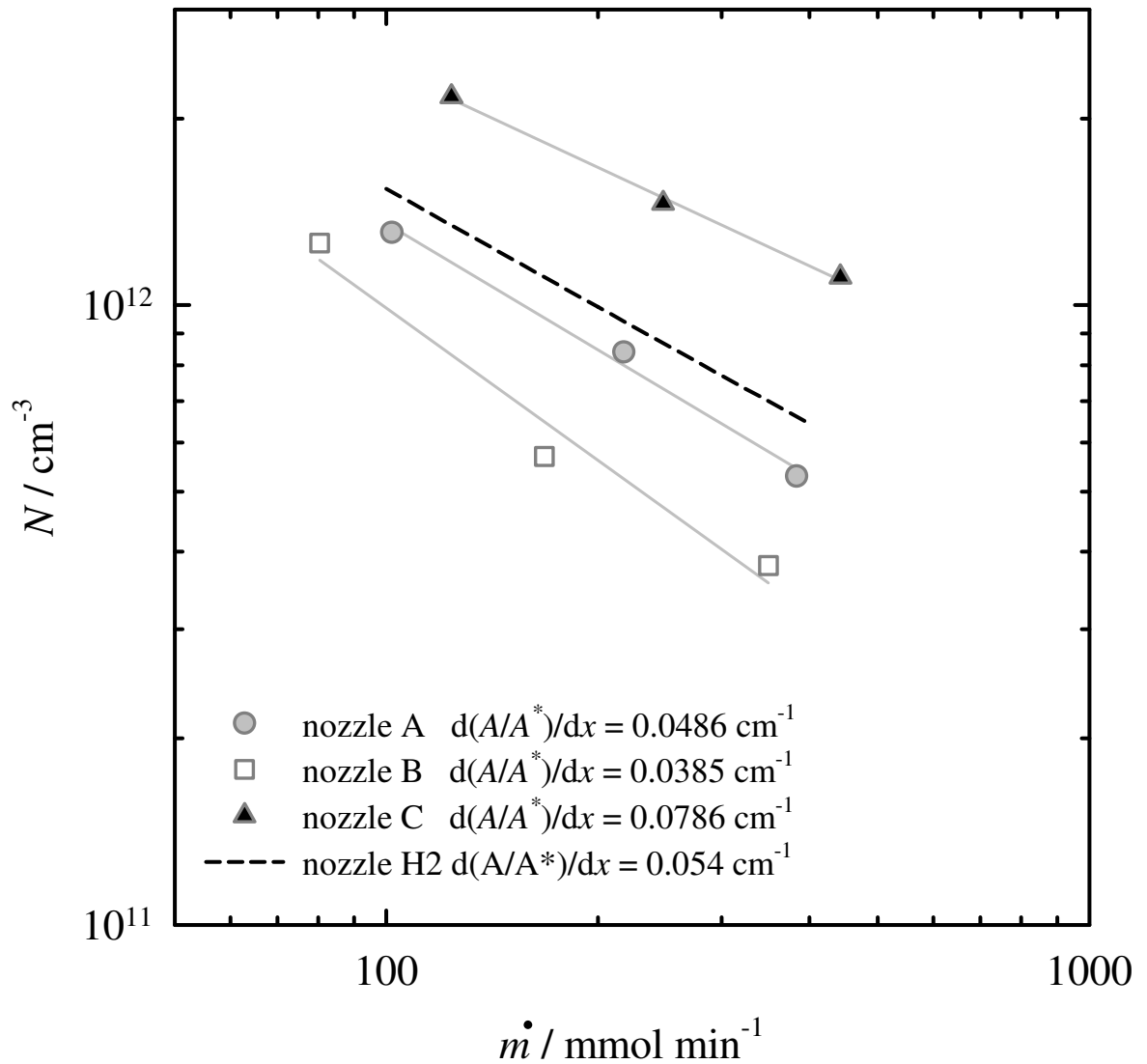


Figure 6.9: Particle number density vs. molar flow rate from former D₂O SANS experiments for Nozzle A ($d(A/A^*)/dx = 0.0486 \text{ cm}^{-1}$), Nozzle B ($d(A/A^*)/dx = 0.0385 \text{ cm}^{-1}$) and Nozzle C ($d(A/A^*)/dx = 0.0786 \text{ cm}^{-1}$) (details and references: see text). The estimated dependency of the particle number densities as a function of flow rate for nozzle H2 ($d(A/A^*)/dx = 0.054 \text{ cm}^{-1}$) is indicated by a black dashed line.

Table 8.4 summarizes the values of interest including the temperature, pressure, supersaturation, and characteristic time corresponding to the maximum nucleation rates, as well as the ratio of gas densities in the nucleation zone to the observation point. The values for the pressure and temperature corresponding to the maximum nucleation rate are identical to those reported in our earlier publication⁶¹ and have been conducted at $p_0 = 59.6 \text{ kPa}$. However, the values for the supersaturation differ from those reported earlier⁶¹ because of

⁶¹ Gharibeh *et al.*, 2005.

the use of a different equilibrium vapor pressure function.⁶² Table 8.4 further summarizes the values of the particle number density N and the nucleation rate J corresponding to a *Gaussian* and a *Schultz* distribution of particles. In general, the nucleation rate varies between $\sim 1 \cdot 10^{17} \text{ cm}^{-3} \text{ s}^{-1}$ and $\sim 5 \cdot 10^{17} \text{ cm}^{-3} \text{ s}^{-1}$. The deviation between the nucleation rate assuming a *Gaussian* and a *Schultz* distribution is therewith less than $\sim 10\%$.

Figure 6.10 illustrates the variation in the measured nucleation rates with supersaturation and temperature. For all three *n*-alcohols, the nucleation rate increases slowly as the supersaturation increases and temperature decreases. A similar trend was also observed for D_2O by *Kim et al.*, in nozzle B.⁶³ The agreement between nucleation rates measured at the same temperature, in expansions starting from different T_0 , is quite reasonable and certainly within the error bars of the measurements. Since all of the measurements were made in a single nozzle the range of accessible nucleation rates is quite small. Additional experiments with nozzles of different opening angles are necessary to obtain the data required to determine the properties of the critical clusters, i.e. the number of molecules in the critical cluster and their excess internal energy.

In an earlier work⁶⁴ it was estimated that the particle number densities were in the range of $1 \cdot 10^{11} < N / \text{cm}^{-3} < 1 \cdot 10^{12}$. This work demonstrates that over the range of conditions investigated N is by a factor of 2 - 10 higher than the average value of N previously estimated to evaluate the nucleation rates.⁶⁴ The particle number densities are $1 \cdot 10^{12} < N / \text{cm}^{-3} < 5 \cdot 10^{12}$. Thus, the newly calculated nucleation rates are higher than the estimated value of $J = 5 \cdot 10^{16} \text{ cm}^{-3} \text{ s}^{-1}$ by the same amount. When assigning an uncertainty factor of 2 to all of the rates, there is some overlap between the current measurements and the earlier estimates,⁶¹ although most of the current values lie slightly above the margin of error.

⁶² Strey and Schmeling, 1983.

⁶³ Kim *et al.*, 2004.

⁶⁴ Gharibeh *et al.*, 2005.

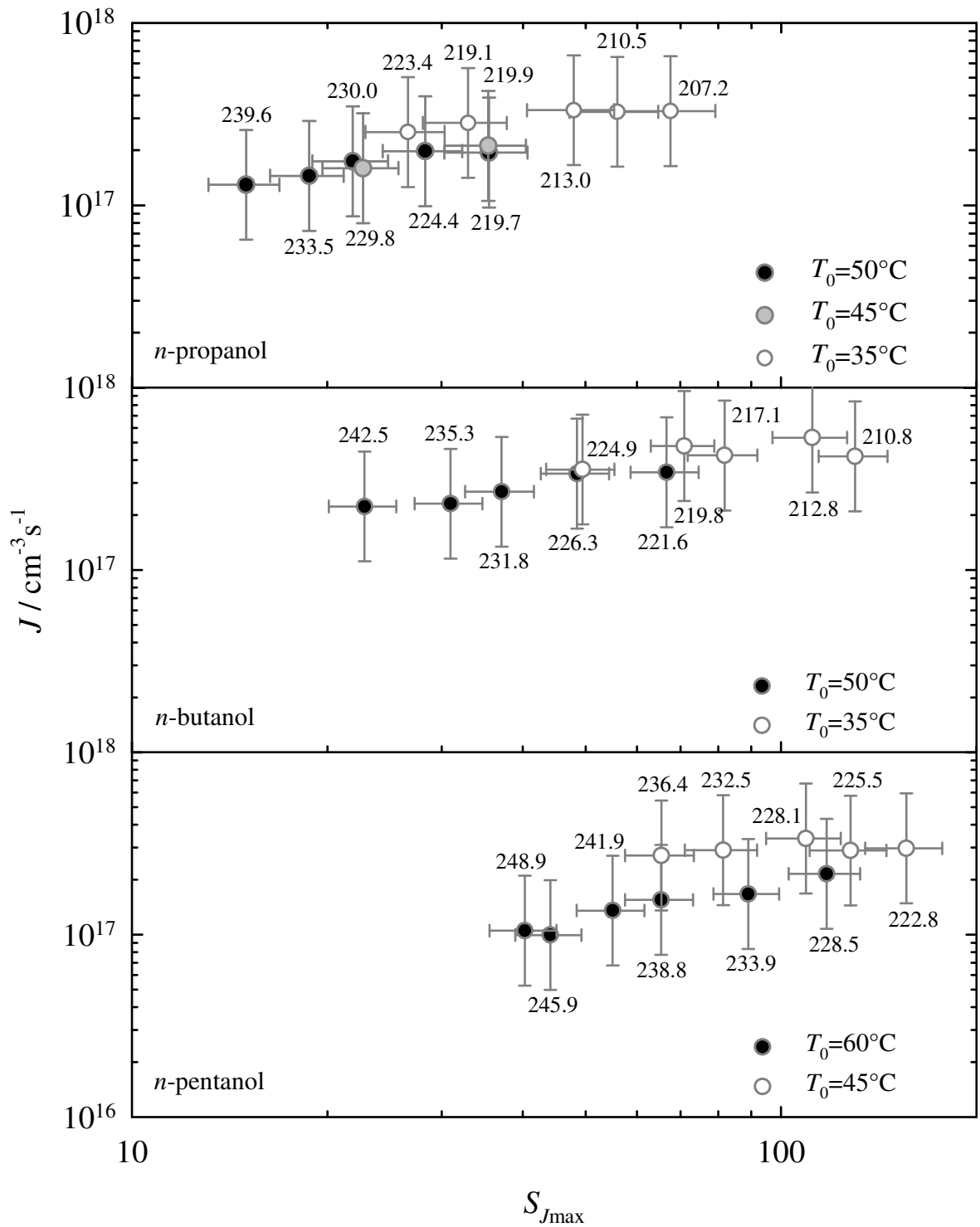


Figure 6.10: The experimental nucleation rate J vs. the supersaturation S for n -propanol, n -butanol, and n -pentanol. The nucleation temperature is additionally exhibited in the figure.

Finally, it is possible to compare the experimental data to those available in the pub-

lished literature⁶⁵ using *Hale's*⁶⁶ scaling formalism. Figure 6.11 plots the normalized nucleation rates $-\ln(J/10^{26})$ vs. $C_0[(T_c/T)-1]^3/(\ln S)^2$. The virtue of the latter parameter is that it simultaneously accounts for differences in the temperature and supersaturation between different experiments. For consistency, the identical equilibrium vapor pressure expressions (Table 8.1) are used to calculate S for all data presented here. The value of C_0 is adjusted until the best fit between the data and a straight line with a slope of 1 is achieved. From C_0 the parameter Ω , the surface entropy per molecule divided by k can be estimated.

$$\Omega = \sqrt[3]{\frac{3C_0 \ln 10}{16\pi}}. \quad (6.1)$$

Remarkable good agreements are found over ~ 21 orders of magnitude between most of the experimental results found in literature and our own (Figure 6.11), e.g. for *n*-pentanol: The data from this work, and those of *Luitjens et al.*,⁶⁷ who used an expansion wave tube, *Hruby et al.*,⁶⁸ who used a nucleation pulse chamber, *Lihavainen et al.*,⁶⁹ who used a laminar flow diffusion chamber, *Graßmann and Peters*,⁷⁰ who used a piston expansion tube, and those of *Ždímal and Smolík*,⁷¹ who used a static diffusion chamber agree remarkable well with each other. This is astonishing, because not only do the nucleation rates differ by ~ 21 orders of magnitude, but also the temperature and supersaturation regimes are often quite removed from each other, and in some cases the experimental techniques rely on very different physical phenomena. The largest scatter in data is seen for *n*-pentanol for the data by *Anisimov et al.*,⁷² who used a laminar flow diffusion chamber, and those of *Rudek et al.*,⁷³ who used an upward thermal diffusion cloud chamber.

The estimates for C_0 changed only slightly from those reported earlier,⁷⁴ and the scaling parameter for *n*-propanol agrees with that presented by *Brus et al.*⁷⁵

⁶⁵ Kacker and Heist, 1985; Strey, Wagner, and Schmeling, 1986; Viisanen and Strey, 1994; Strey, Viisanen, and Wagner, 1995; Hruby, Viisanen, and Strey, 1996; Luitjens, Baas, and van Dongen, 1997; Viisanen, Wagner, and Strey, 1998; Zdímal and Smolík, 1998; Rudek *et al.*, 1999; Anisimov *et al.*, 2000; Graßmann and Peters, 2000; Lihavainen, Viisanen, and Kulmala, 2001b; Graßmann and Peters, 2002; Schmitt and Doster, 2002; Iland *et al.*, 2004b; Brus *et al.*, 2005; Brus, Zdímal, and Stratmann, 2006.

⁶⁶ Hale, 1986; Hale, 1992.

⁶⁷ Luitjens, Baas, and van Dongen, 1997.

⁶⁸ Hruby, Viisanen, and Strey, 1996.

⁶⁹ Lihavainen, Viisanen, and Kulmala, 2001b.

⁷⁰ Graßmann and Peters, 2000.

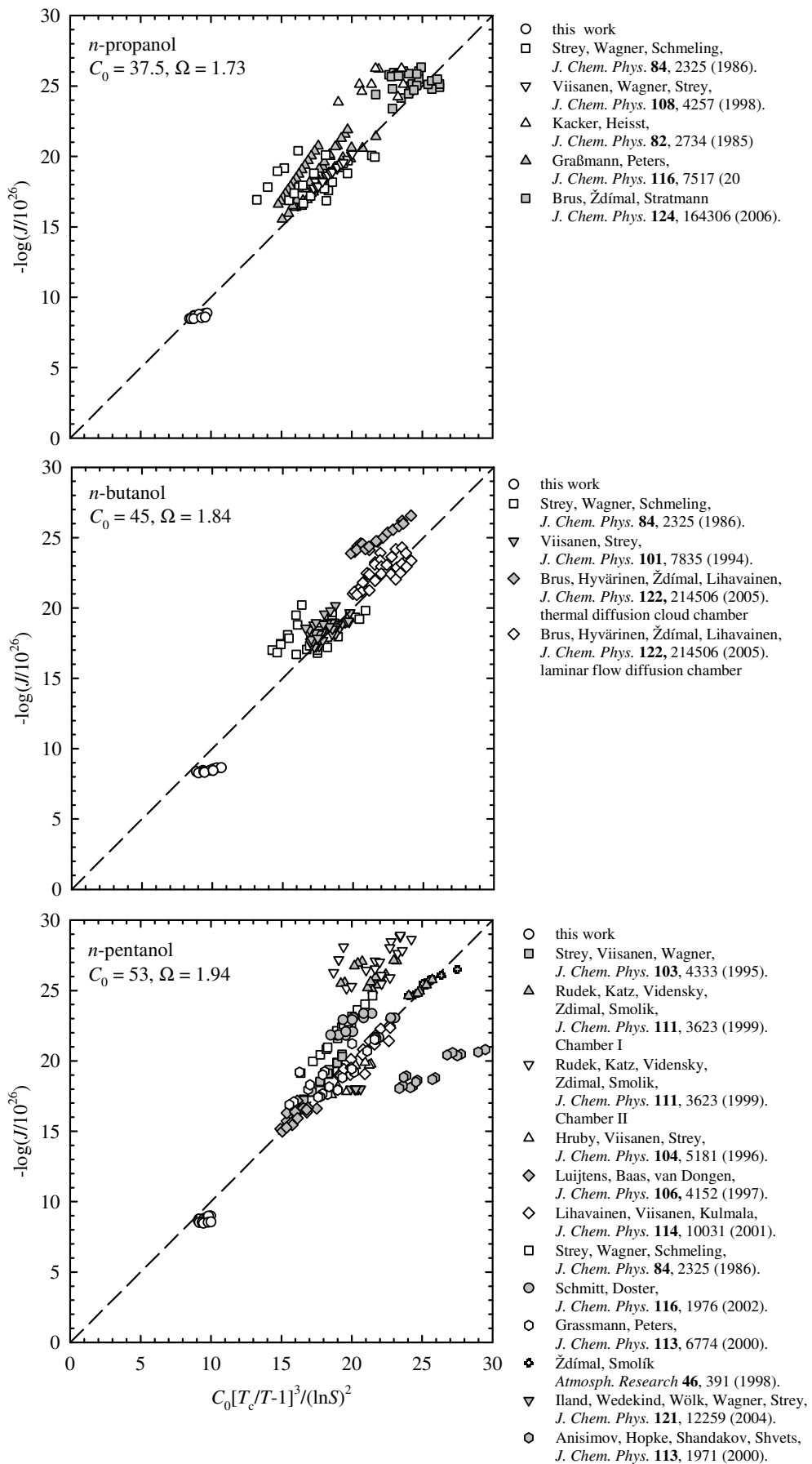
⁷¹ Zdímal and Smolík, 1998.

⁷² Anisimov *et al.*, 2000.

⁷³ Rudek *et al.*, 1999.

⁷⁴ Gharibeh *et al.*, 2005.

⁷⁵ Brus, Zdímal, and Stratmann, 2006.

Figure 6.11: The *n*-alcohol nucleation rates available in the literature are presented in a series of Hale plots.

6.2 The Effect of Temperature Dependent Heat Capacity on the Nucleation Temperature and the Critical Superaturation

Argon as mono-atomic “molecule” has three degrees of freedom, which are all translational degrees, and thus, the heat capacity is constant for all temperatures. For small and simple molecules, e.g. water or short chained *n*-alcohols and *n*-alkanes the temperature dependency of the heat capacity is negligible and often assumed to be constant. However, for longer chained *n*-alkanes such as *n*-nonane the molecule size, bondings, and intra molecular branching increase. Therewith, the complexity of the molecule and the number of degrees of freedom for rotation and vibration also increase. As a consequence of this, the heat capacity of these molecules can no longer be assumed to be constant and must be treated in a temperature dependent manner.

In Figure 6.12 the deviation in the nucleation temperature, and thus, in the supersaturation using equation (2.24) with a temperature independent heat capacity ($c_p = \text{const.}$, $\gamma = c_p / c_v = 1.1$) and equation (2.20) with a temperature dependent heat capacity $c_p(T)$ is investigated for two sets of *n*-nonane literature values, *Wagner and Strey*,⁷⁶ and *Viisanen et al.*,⁷⁷ by plotting the nucleation rate vs. the supersaturation. Both sets of data have been investigated using the two piston expansion chamber. The supersaturation is defined as

$$S = \frac{p}{p^\infty(T)}. \quad (6.2)$$

Here p is the partial pressure of the condensible species and $p^\infty(T)$ the equilibrium vapor pressure of the condensible species at the nucleation temperature T (T_{exp} in Chapter 2.3). A change in nucleation temperature is reflected by a change in the supersaturation.

For the *Wagner and Strey*⁷⁶ data (Figure 6.12, top) measured for the initial temperatures $T_0 = 25^\circ\text{C}$, $T_0 = 5^\circ\text{C}$, and $T_0 = -15^\circ\text{C}$ the nucleation temperatures are increased by ~ 3 K, ~ 0.5 K, and ~ 0.1 K, respectively, using equation (2.20) instead of equation (2.24) with $\gamma = c_p / c_v = 1.1$. This increase in nucleation temperature is accompanied by an increase in equilibrium vapor pressure and consequently by a decrease in supersaturation. Clearly the effect of the change in nucleation temperature and supersaturation are amplified as the expansion path is increased (Figure 2.6).

For the *Viisanen et al.*⁷⁷ data measured for the initial temperature $T_0 = 28.1^\circ\text{C}$ the nucleation temperature T shifts up from $T = 230$ K to $T \sim 231.15$ K. Consequently, the equi-

⁷⁶ Wagner and Strey, 1984.

⁷⁷ Viisanen, Wagner, and Strey, 1998.

librium vapor pressure increases and the supersaturation values are shifted to lower values.

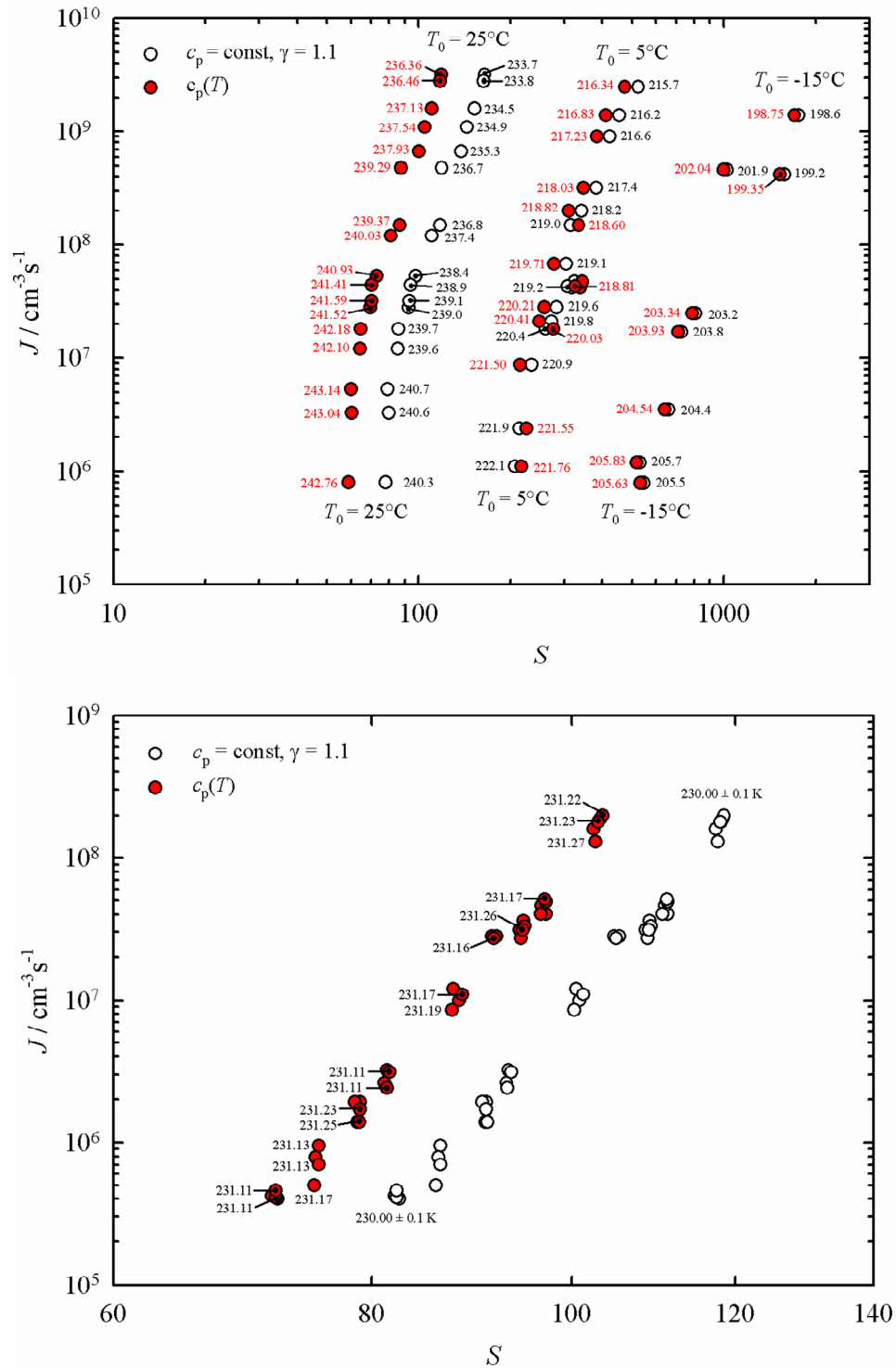


Figure 6.12: The nucleation J rate vs. the supersaturation S for n -nonane measured by *Wagner and Strey* (top) and *Viisanen et al.* (bottom). The empty symbols are the literature values. Here the temperature T is calculated by equation (2.24) with $\gamma = 1.1$. The temperatures of the red filled symbols have been recalculated by equation (2.20). The change in temperature T causes a change in equilibrium vapor pressure $p^\infty(T)$, and thus, also in supersaturation S .

When observing a plotted series of measurements, the observer generally judges that the abscissa is correct and if at all the ordinate is faulty. It is important to realize that, the abscissa (the supersaturation) can carry substantial error in itself when plotting the nucleation rate J vs. the supersaturation S . These errors can for example reflect in a faulty critical cluster size ($\partial \ln J / \partial \ln S \approx n^*$) or also in a wrong excess internal energy. From Figure 6.12 it is evident that an estimated value of $\gamma = c_p / c_v = 1.1$ could falsify the nucleation temperature and further the critical supersaturation for substances analog to n -nonane. Treating the heat capacity in a temperature dependent manner (equation (2.20)) should accurately give the nucleation temperature and supersaturation. Thus, in the following chapters the heat capacity for the n -alkanes is treated as a temperature dependent function for the first time during such supersonic nozzle expansion experiments.

6.3 n -Alkane Pressure Trace Measurements

As a mixture of carrier gas and condensible vapor flows through the nozzle, it undergoes an adiabatic expansion. During this expansion the temperature of the gas mixture drops rapidly, and the supersaturation of each component rises (Chapter 5.1). In a p - T diagram, the condensible species crosses its equilibrium vapor pressure line and enters the meta-stable vapor state. As the meta-stable vapor relaxes to the stable liquid state by condensation, heat is released to the flow. Static pressure trace measurements detect the addition of latent heat as a positive deviation of the measured condensing flow profile from the pressure profile calculated for an expansion of the same gas mixture in the absence of condensation, i.e. the wet theoretical isentrope.

Ideally, the condensing flow curve and the wet isentrope agree up to the onset, i.e. the begin of condensation. In some cases, however, the condensing flow curve lies slightly below the wet isentrope prior to the onset (Figure 6.13). In the worst case, a flow rate of $70.9 \text{ mmol min}^{-1}$ n -nonane in N_2 at $T_0 = 35^\circ\text{C}$ for example, shown as inset in Figure 6.13, it is found that the temperature along the wet isentrope is up to 0.3 K higher than along the condensing flow curve, and the ratio of the condensate mass fraction to the initial mass fraction of condensible g/g_∞ is slightly negative (-3.5%). These deviations may be due to minor changes to the shape of the boundary layer as the mixture of the composition changes. And they primarily effect the values of the condensible partial pressure $p_{J_{\max}}$ and the effect on the supersaturation $S_{J_{\max}}$ is well within the standard error of $\pm 10 - 15 \%$ based

on a potential systematic error of ± 1 K in the plenum temperature T_0 . Table 8.5 summarizes the experimental conditions as well as the thermo-physical properties of interest corresponding to the maximum nucleation rate for the n -alkanes.

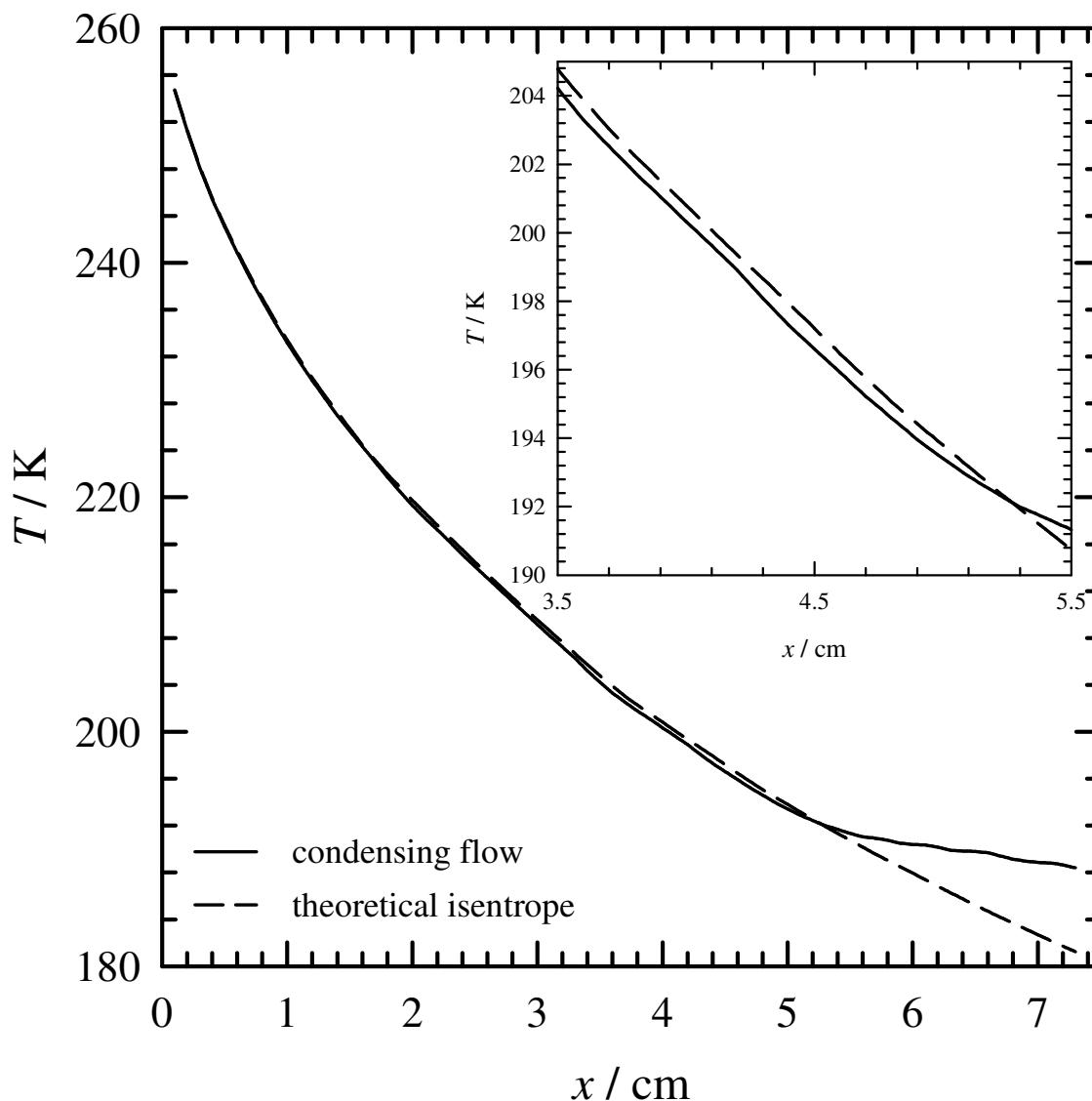


Figure 6.13: A temperature profile $T(x)$ for a flow rate of $70.9 \text{ mmol min}^{-1}$ n -nonane in N_2 at $T_0 = 35^\circ\text{C}$.

Figure 6.14 illustrates on a linear-log plot the changes in the maximum nucleation temperature as a function of the n -alkane flow rate. The data lie on a series of straight lines reasonably parallel to each other, with each line corresponding to a particular n -alkane expanding from a constant plenum temperature T_0 in a given carrier gas. The solid grey lines correspond to measurements made with Argon and the dashed black lines to Nitrogen as carrier gas, respectively, and are only meant to guide the eye. At a given molar

flow rate \dot{m} the temperature $T_{J_{\max}}$ increases as the n -alkane chain length increases. For a particular n -alkane, the temperature $T_{J_{\max}}$ increases at a given molar flow rate \dot{m} as the stagnation temperature T_0 decreases. For an n -octane in N_2 expansion at a flow rate of $\sim 85 \text{ mmol min}^{-1}$, for example, the maximum nucleation temperature increases from $T_{J_{\max}} = 175.4 \text{ K}$ when $T_0 = 25^\circ\text{C}$ to $T_{J_{\max}} = 178.4 \text{ K}$ when $T_0 = 15^\circ\text{C}$. This trend also holds for experiments when Ar is used as carrier gas. For a n -heptane in argon flow rate of 98 mmol min^{-1} at $T_0 = 45^\circ\text{C}$ a maximum nucleation temperature of $T_{J_{\max}} = 164.9 \text{ K}$ is reached. Decreasing the plenum temperature by 35 K to $T_0 = 10^\circ\text{C}$ increases the maximum nucleation temperature to $T_{J_{\max}} = 171.3 \text{ K}$ for a flow rate of 96 mmol min^{-1} of n -heptane in Ar. Furthermore, when switching the carrier gas from N_2 to Ar for a particular n -alkane a higher maximum nucleation temperature is reached. This behavior can be clearly seen in Figure 6.14 for n -heptane, n -octane, and n -nonane. Although no experiments were conducted in Ar and N_2 as carrier gas with identical plenum temperatures T_0 a direct comparison can be made. Generally, the experiments conducted in Ar as carrier gas have larger plenum temperatures T_0 . For a given n -alkane and flow rate the maximum nucleation temperature usually shifts towards smaller values for high plenum temperatures T_0 . However, an increase in maximum nucleation temperature is observed as the carrier gas is switched from N_2 to Ar even though simultaneously the plenum temperature is increased. Here it is observed that the carrier gas Ar overcompensates the decrease in maximum nucleation temperature due to the increase in plenum temperature in such a strong manner which effectively leads to an increase the maximum nucleation temperature.

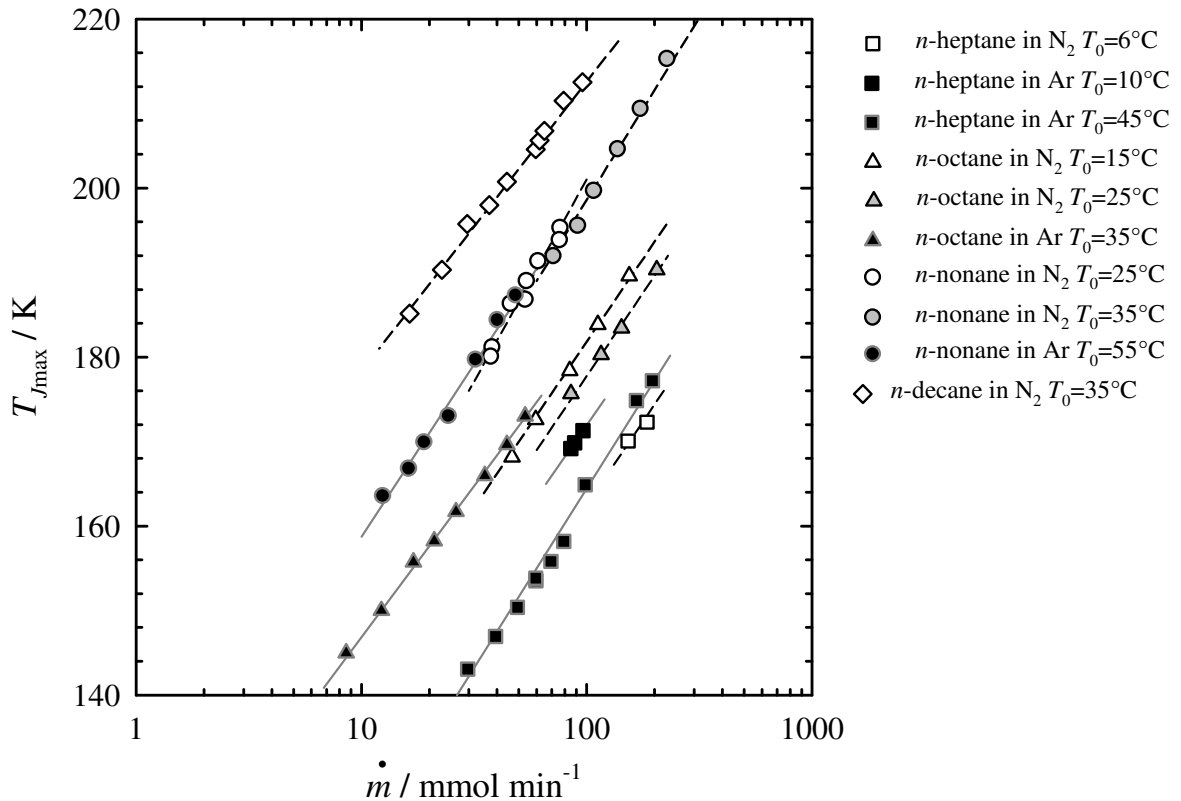


Figure 6.14: The temperature $T_{J_{\max}}$ that corresponds to the maximum nucleation rate vs. the molar flow rate. The grey solid lines and the black dashed lines which correspond to measurements with argon and nitrogen as carrier gas, respectively, are intended to guide the eye.

A far more unified picture is presented in Figure 6.15 where the maximum nucleation pressures $p_{J_{\max}}$ of the condensible species are plotted as a function of the inverse temperatures $T_{J_{\max}}$ in a *Volmer* plot.⁷⁸ The grey solid lines and the black dashed lines correspond to measurements with argon and nitrogen as carrier gas, respectively, and are meant to guide the reader's eye. There is no drawn line for the *n*-heptane in nitrogen data because there are too few points. In this figure, the data points for each *n*-alkane – carrier gas mixture lie along a single straight line independent of the stagnation temperature T_0 . It is important to point out, that the changes in the nucleation temperature $T_{J_{\max}}$, with the molar flow rate \dot{m} which arise from the change in plenum temperature T_0 (Figure 6.14) are accompanied by changes in the condensible partial pressure $p_{J_{\max}}$ as well. Thus, the discontinuities cancel down. The *n*-nonane data in N₂ which were conducted at many conditions, for example at $T_0 = 25^\circ\text{C}$, $p_0 = 30.2$ kPa, and $T_0 = 25^\circ\text{C}$, $p_0 = 59.6$ kPa, and also at $T_0 = 35^\circ\text{C}$, $p_0 = 59.6$ kPa, show no discernable differences between these curves. The lines

⁷⁸ Volmer and Weber, 1926.

corresponding to different n -alkanes and a particular carrier gas are reasonably parallel to each other. At a given maximum nucleation pressure $p_{J_{\max}}$, the maximum nucleation temperature $T_{J_{\max}}$ increases as the carbon chain length increases. For a given n -alkane and nucleation pressure $p_{J_{\max}}$, measurements using Ar reach lower values of $T_{J_{\max}}$ compared to corresponding experiments using N_2 . This effect is entirely consistent with the following observation: By switching the carrier gas from N_2 ($\gamma=7/5$) to Ar ($\gamma=5/3$) the nucleation position is reached earlier in the nozzle, i.e. further upstream (Chapter 5.4). Here the expansion rate \dot{p}/p_0 and the cooling rate $d(T/T_0)/dx$ are large. Consequently, by using Ar instead of N_2 we are able to probe steeper into the meta-stable regime, e.g. lower pressures and temperatures for the phase transition are reached. Additionally higher nucleation rates are achieved. This is similar to switching between nozzles with different physical opening angles $d(A/A^*)/dx$ while using the same carrier gas.

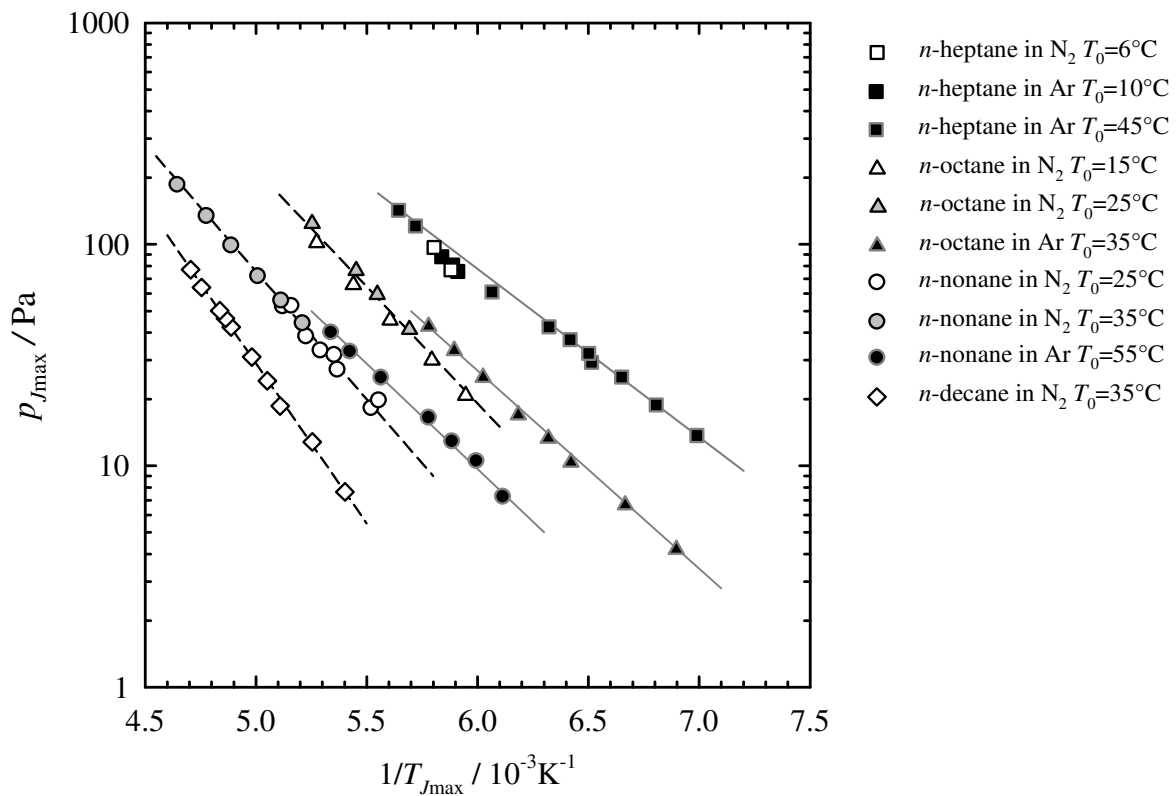


Figure 6.15: A Volmer plot of the condensible partial pressure $p_{J_{\max}}$ vs. the inverse maximum nucleation temperatures $T_{J_{\max}}$. The grey solid lines and the black dashed lines which correspond to measurements with argon and nitrogen as carrier gas, respectively, are intended to guide the eye.

In Figure 6.16 the critical supersaturation is plotted as a function of the inverse maximum nucleation temperature. The dashed-dotted-dotted lines are intended to guide the

reader's eye. The data points of each n -alkane lie on a curved line reasonably parallel to each other. At a fixed nucleation temperature the critical supersaturation increases as the carbon chain length of the n -alkanes increases. The curved line behavior is consistent with the predictions of CNT.⁷⁹ By combining equation (2.25), (2.26), and (2.27) we obtain

$$J = K \cdot \exp\left(n^* k T \ln S + 4\pi r^* \sigma\right). \quad (6.3)$$

By rearranging the following expression is obtained

$$\ln S = \frac{4\pi r^* \sigma}{n^* k} \cdot \frac{1}{T} - \frac{\ln(J/K)}{n^*} \quad (6.4)$$

$$\ln S = A \cdot \frac{1}{T} - B,$$

where r^* is the radius of the critical cluster, n^* the number of molecules in the critical cluster, J the nucleation rate and K the kinetic prefactor for the nucleation rate. In a particular supersonic nozzle, the nucleation rate J rarely varies by more than a few orders of magnitude and K is also roughly constant. A straight line, or also a line with a constant slope, can only be expected if both $A \propto r^2 \sigma / n^* \propto \sigma / r$ and B are constant. However, for non-isothermal measurements the surface tension σ increases and r^* decreases as the temperature T decreases. Consequently, the parameters A and B cannot be constant. Thus, the dependency of the supersaturation on the inverse temperature is not linear over a large enough temperature range. This behavior can be seen in Figure 6.16, where the slope of the data for each n -alkane increases as the temperature decreases. In particular, the effect is clearly seen for the n -heptane data where experiments were conducted over a wide temperature range in Ar. The n -octane and n -nonane data are confounded by the fact that two carrier gases, Ar and N₂, were used. This changes the nucleation position in the nozzle, which in turn affects the expansion rate, the cooling rate, and the nucleation rate J in our nozzle, and thus, some of the change in the slope is reflected by these changes.

⁷⁹ Becker and Döring, 1935.

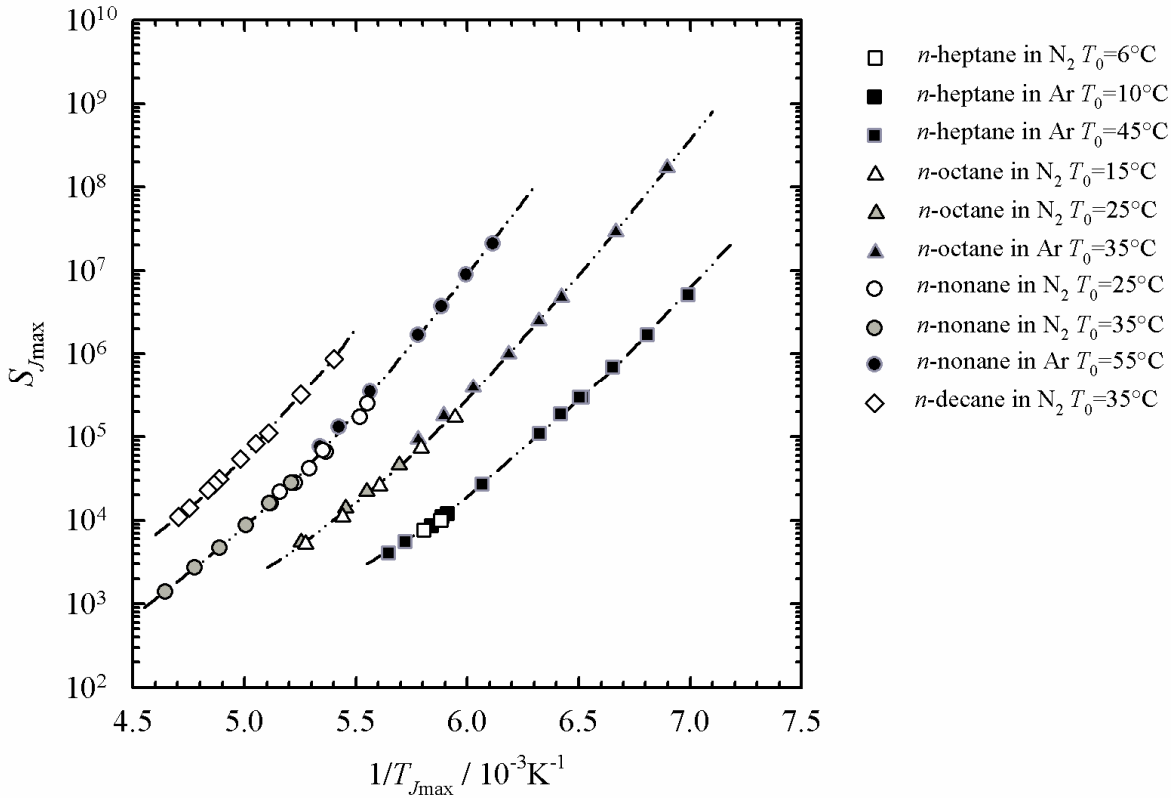


Figure 6.16: The critical supersaturation $S_{J_{\max}}$ corresponding to the maximum nucleation rate vs. the inverse maximum nucleation temperature $T_{J_{\max}}$. The black dashed-dotted-dotted lines are intended to guide the reader's eye.

In order to quantitatively determine the nucleation rate $J_{\max} = N / \Delta t_{J_{\max}}$ it is necessary to know the characteristic time $\Delta t_{J_{\max}}$ corresponding to the maximum nucleation rate. When calculating $\Delta t_{J_{\max}}$ by analyzing the pressure trace measurements using equation (4.26), it is important that the maximum nucleation rate occurs far enough upstream so that the entire nucleation pulse is inside the nozzle. This condition is not always met for the lowest n -alkane flow rates, and thus, the calculated characteristic times are smaller than they actually should be even if the conditions corresponding to the maximum nucleation rate can still be estimated. Going to longer nozzles would only delay the problem to lower flow rates, not eliminate it. When a dash appears for the characteristic time in Table 8.5, it corresponds to conditions where the entire nucleation pulse was not inside the nozzle. The pressure trace measurements show that the characteristic time corresponding to the maximum nucleation rate, is in the range of $1 \cdot 10^{-5} \leq \Delta t_{J_{\max}} / s \leq 4 \cdot 10^{-5}$. In Figure 6.17 the characteristic time is plotted vs. the expansion rate $d(p/p_0)/dt$. Even though there is a rather large scatter in the characteristic time, a general trend can be seen: As the expansion rate

$d(p/p_0)/dt$ declines sharper the characteristic time decreases. The reason for this is that the expansion rate reflects how steep the system is probing into the meta-stable regime. Probing with a sharper decline into the meta-stable regime enables the system to cross the equilibrium vapor pressure curve and reach states of higher nucleation rates for the relaxation. Higher nucleation rates in turn can correlate to shorter times for particle production, or also shorter nucleation bursts. Interestingly, during supersonic nozzle investigations the highest nucleation rates are observed for experiments with a low flow rate of condensible specie. Here, the nucleation temperature is low, the supersaturation is large, the characteristic time is large as well and the phase transition happens near the exit of the nozzle where the negative expansion rate is low. It is important to realize that the characteristic time also depends on how fast growth occurs. Nonetheless, further investigations need to be carried out in order to fully understand these phenomena. The values for the characteristic times (Figure 6.17) are by a factor of 2 - 3 larger than those from previous D₂O measurements by *Kim et al.*⁸⁰ in the same nozzle $5.9 \cdot 10^{-6} \leq \Delta t_{J_{\max}} / s \leq 1.2 \cdot 10^{-5}$. Finally, this is what will enable us to probe the the region where particle formation and growth are both occurring and competing.

⁸⁰ *Kim et al.*, 2004.

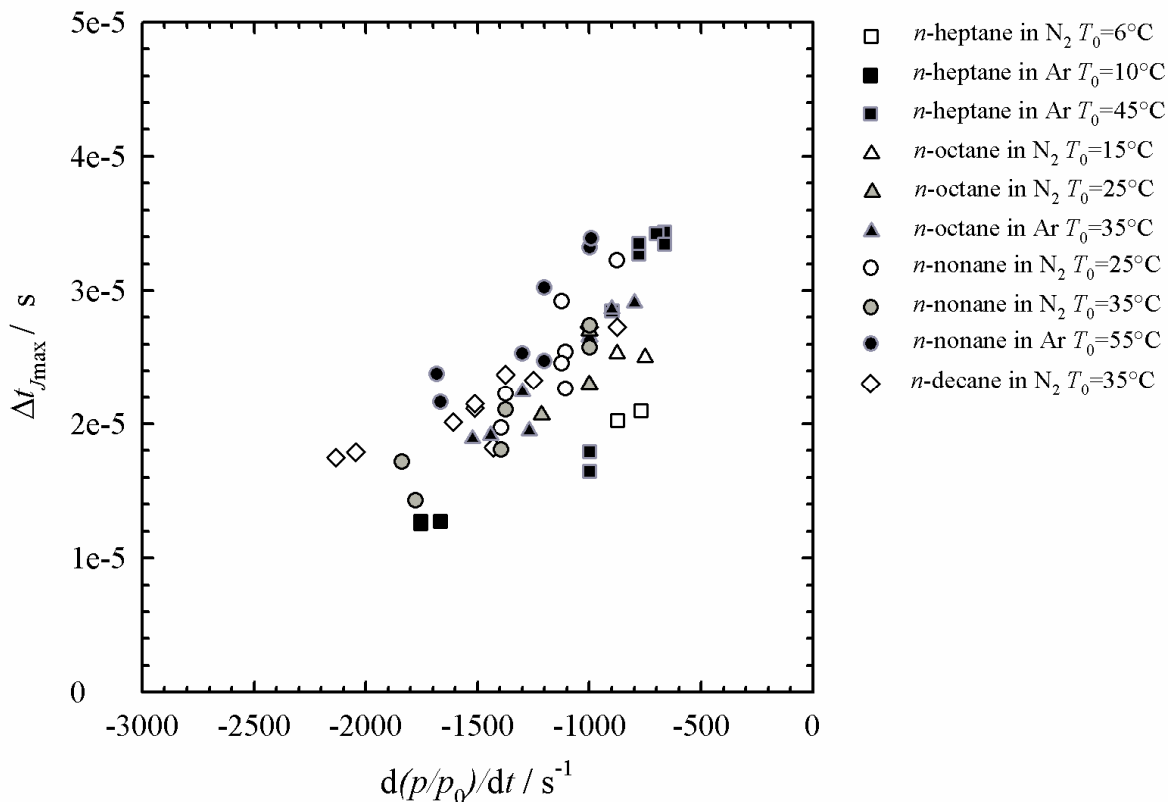


Figure 6.17: The characteristic time $\Delta t_{j_{\max}}$ vs. the expansion rate $d(p/p_0)/dt$ corresponding to the maximum nucleation rate for the series of n -alkanes.

6.4 n -Alkane SAXS Measurements

For all of the n -alkane Small Angle X-ray Scattering experiments, the x-ray beam was located $x = 7$ cm downstream of the throat of nozzle C2. The nozzle operating conditions, i.e. stagnation temperature T_0 , stagnation pressure p_0 , carrier gas, and condensible flow rate \dot{m} , were all chosen to match those of the earlier pressure trace measurements as closely as possible, i.e. stagnation temperatures between $T_0 = 15^\circ\text{C}$ and $T_0 = 55^\circ\text{C}$, a stagnation pressure of $p_0 = 30.2$ kPa, and Ar as well N_2 as carrier gas were used. Ar has a higher heat capacity ratio compared to N_2 , and thus, by using Ar it is possible to reach lower temperatures in the same nozzle (Chapter 5.4). For all of the thermodynamic measurements (Chapter 6.3) nozzle C was used, which has a linear opening angle $d(A/A^*)/dx = 0.078$ cm^{-1} in the supersonic region. Here A/A^* is the area ratio and A^* is the area of the throat. For these SAXS experiments a new nozzle, nozzle C2, was built with an identical opening angle of $d(A/A^*)/dx = 0.078$ cm^{-1} (Figure 6.18). The opening angles for both nozzles were determined by a linear fit to the area ratio from 2 to 7 cm downstream of the throat.

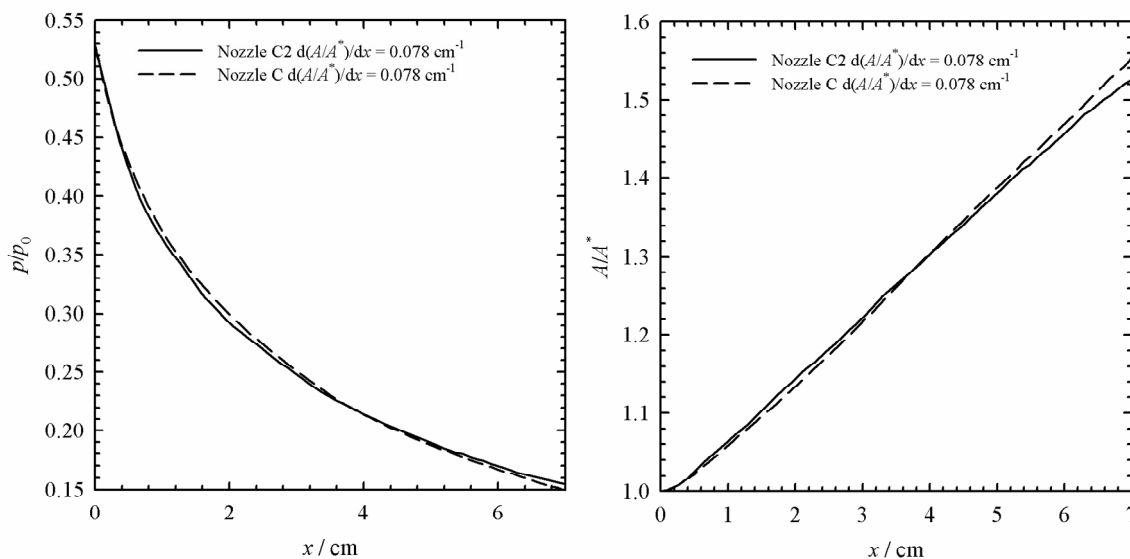


Figure 6.18: The pressure ratio (left) and the area ratio (right) of nozzle C (pressure trace measurements) and C2 (SAXS experiments) at $p_0 = 30.2$ kPa and $T_0 = 25^\circ\text{C}$ using nitrogen as carrier gas.

Figure 6.19 illustrates the radially averaged x-ray spectra for *n*-heptane in argon at $T_0 = 45^\circ\text{C}$ and $p_0 = 30.2$ kPa with varying flow rates. The spectrum for *n*-heptane at a flow rate of 52 mmol min^{-1} is at the true absolute intensity scale as determined using a calibration factor obtained by comparing D_2O SAXS spectra to D_2O SANS spectra made under the same conditions using the NG7-SANS instrument at the NIST Center for Neutron Research.⁸¹ For clarity the spectra at higher flow rate are offset by factors of 16, 256, 4096, 65536, and 1048576, respectively, and the error bars have been omitted. Below $q = 1\text{ nm}^{-1}$ the error is less than 1% of the signal and for $q > 1\text{ nm}^{-1}$ the error is generally less than 5% of the signal (Figure 6.20). In Figure 6.19 it can be observed that at high flow rates the data cover ~ 6 orders of magnitude in intensity over the accessible q -range, while at low flow rates the intensity covers $\sim 4\frac{1}{2}$ orders of magnitude. As the flow rate increases, the point of inflection in the intermediate q range moves to lower q values, an indication that the particle size is increasing. At the same time the inflection point develops into a more pronounced feature, which indicates that the particle size distribution is becoming more monodisperse.

⁸¹ Wyslouzil, Strey, and Wilemski, 2007.

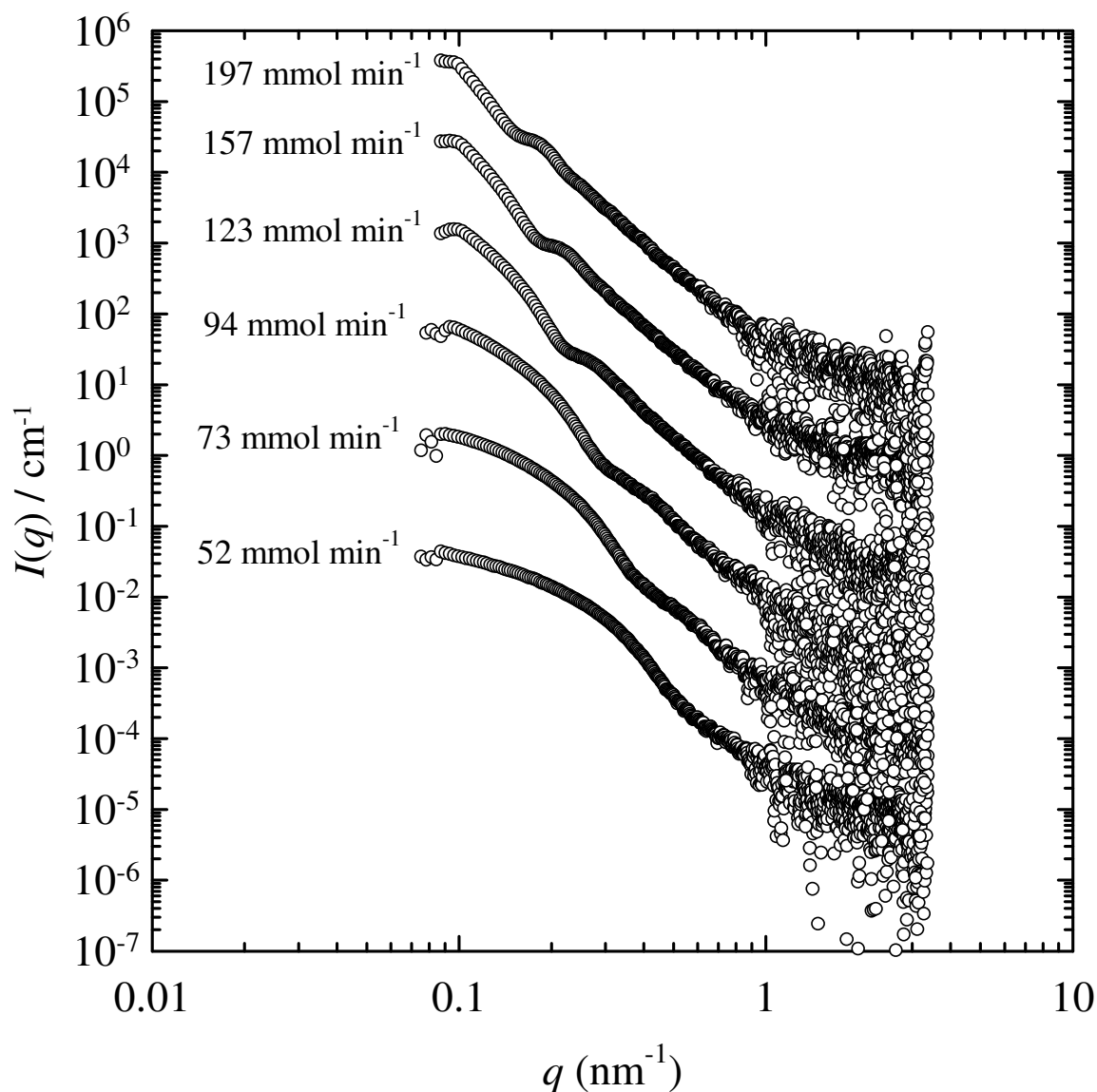


Figure 6.19: All one-dimensional *n*-heptane SAXS spectra in this figure are measured at $T_0=45^\circ\text{C}$ and $p_0=30.2\text{ kPa}$. The spectrum for 52 mmol min^{-1} of *n*-heptane is at the true absolute intensity scale as determined using a calibration factor. For clarity, the spectra at higher flow rates are offset by factors of 16, 256, 4096, 65536, and 1048576, respectively. For clarity error bars are omitted.

All of our measurements used a fixed sample to detector distance of 2 m. This setting is reasonable for particles with average radii $\langle r \rangle$ up to ~ 20 nm, a size that corresponds to the largest particles that had been previously observed in a nozzle.⁸² Ideally, the feature at intermediate q should be in the middle of the experimental q -range so that the spectrum contains enough scattering information from both the large particles that scatter at low q , and the small particles that scatter at high q . As illustrated in Figure 6.19, at the highest

⁸² Streletzky *et al.*, 2002.

n-alkane flow rates the feature is no longer centered in the q -range. Nevertheless, under these conditions, it is found that there was still enough signal at low q to accurately determine values for the mean radius. Furthermore, the highly resolved scattering signals in the high q region allows fitting the data to a function that accounts for the diffusive interface of the particles (Chapter 4.2.2).⁸³

Figure 6.20 exhibits a SAXS spectrum for *n*-nonane in N₂ at $T_0 = 35^\circ\text{C}$ and $p_0 = 30.2$ kPa and an *n*-alkane flow rate of 177.8 mmol min⁻¹. The error bars, based on count statistics, are shown and the data are on the correct absolute intensity scale. The solid line is the fit to the data assuming scattering from a *Gaussian* distribution of polydisperse spheres with a diffuse interface (Equation (4.31) - (4.35)) and the parameters of the size distribution are noted in the figure. For all of the fits, it is found that the incoherent background that arises from small differences between scattering from the sample and the empty cell, is always in the range of $3 \cdot 10^{-7} < I_{\text{Incoh}} / \text{cm}^{-1} < 4 \cdot 10^{-5}$, and that there is no systematic variation of I_{Incoh} with the composition of the condensing mixture.

⁸³ Strey, 1992.

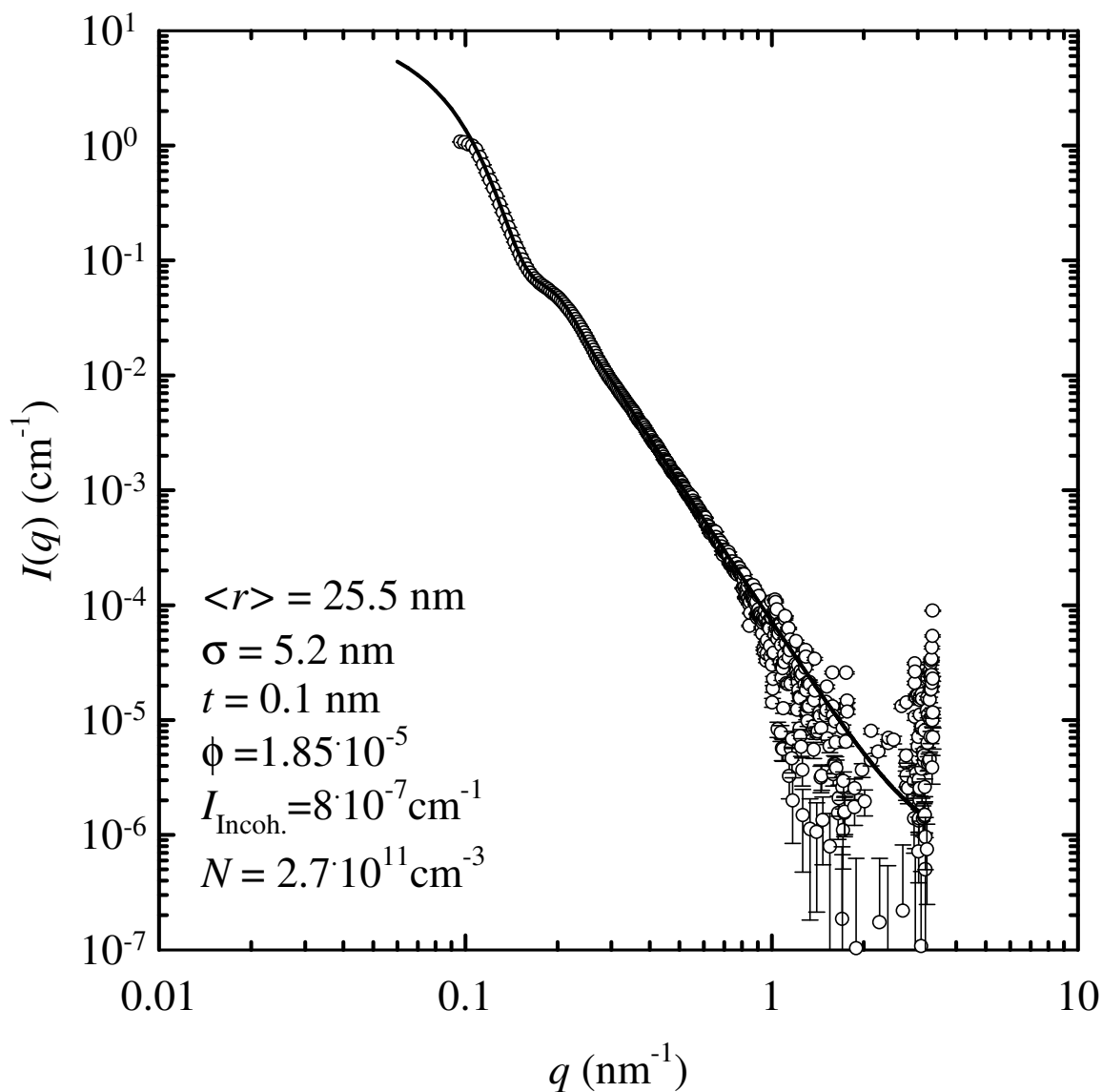


Figure 6.20: One-dimensional SAXS spectrum for *n*-nonane with a flow rate of $177.8 \text{ mmol min}^{-1}$ at $T_0 = 35^\circ\text{C}$ and $p_0 = 30.2 \text{ kPa}$. The solid line indicates the fit to the measured data (circles) assuming a *Gaussian* distribution of droplets with a diffuse interface.

Table 8.6 summarizes the nozzle operating conditions and the aerosol properties including the mean radius $\langle r \rangle$, the width of the size distribution function σ , the particle number density N , the polydispersity index $p = \sigma/\langle r \rangle$, the thickness of the diffuse interface thickness t_D , and the volume fraction of the aerosol droplets ϕ derived by fitting the spectra. The last column in Table 8.6 is the average time available for droplets to grow before they are detected. This time corresponds to the time of flight t_{tof} between the maximum nucleation position $x_{J_{\text{max}}}$ and the detection position $x = 7 \text{ cm}$ downstream of the throat.

Figure 6.21 – Figure 6.24 illustrate the variation of $\langle r \rangle$, σ , and N with the *n*-alkane mo-

lar flow rate \dot{m} for *n*-heptane, *n*-octane, *n*-nonane, and *n*-decane. Droplets in the range $5 < \langle r \rangle / \text{nm} < 30$ were found. At a fixed stagnation temperature T_0 , the average particle size $\langle r \rangle$ increases with increasing *n*-alkane flow rate \dot{m} . This observation is easily explained by recognizing that as the molar flow rate \dot{m} increases at a fixed T_0 , the amount of condensible vapor in the gas mixture increases, and thus, the particles have the potential to grow larger. Furthermore, in these experiments the particle number density decreases by $\sim 1/2$ - $2 1/2$ orders of magnitude as the flow rate increases. With fewer droplets and more vapor available for growth, the droplet size increases even more rapidly than the $\sqrt[3]{\dot{m}}$ scaling expected if N were constant (Chapter 6.1). Unlike the *n*-alcohols, the average particle size of the *n*-alkane droplets is also quite sensitive to the plenum temperature T_0 , with $\langle r \rangle$ increasing rapidly as T_0 decreases at a fixed *n*-alkane flow rate (Figure 6.22 for *n*-octane and Figure 6.23 for *n*-nonane). Decreasing stagnation temperatures T_0 (Chapter 5.3) shift the nucleation corresponding to the maximum particle formation rate closer to the throat, i.e. further from the observation point. Thus, at a fixed condensible flow rate, particles formed in expansions starting from a lower T_0 have more time to grow before they are observed (see Table 8.5), an effect that is clearly confirmed by the data in Figure 6.22 and Figure 6.23. For example, at an *n*-octane flow rate of $136.8 \text{ mmol min}^{-1}$, the value of the mean radius $\langle r \rangle$ is 9.4 - 9.8 nm and the time available for growth is $\sim 13 \mu\text{s}$ when $T_0 = 25^\circ\text{C}$. When the plenum temperature is decreased to $T_0 = 15^\circ\text{C}$ at a very similar flow rate, $133.6 \text{ mmol min}^{-1}$, the time of flight increases to $\sim 63 \mu\text{s}$ and the mean radius $\langle r \rangle$ increases to $\sim 16.8 \text{ nm}$. Evidently the growth of *n*-alkane droplets is driven by two major forces: Exhaustibility of the gas reservoir and the available time for particle growth.

The width of the aerosol distribution function ranges from about 3 nm to 6 nm, increasing with the *n*-alkane flow rate. Changing the plenum temperature does not strongly influence σ at a given molar flow rate. As for the *Gaussian n*-alcohol fits, the polydispersity index $P = \sigma / \langle r \rangle$ decreases with increasing flow rate. It must be noted that for the *n*-alcohols it is found that the *Schultz* fits give more consistent values of the polydispersity index P , and so the change in the polydispersity P with \dot{m} may be caused by the *Gaussian* distribution function.

The diffuse interface thickness t_D was always in the range of $t_D \sim 0.1$ - 0.2 nm or roughly about 11% - 22% of the length of an *n*-heptane molecule or 8.3% - 16.6% of the length of an *n*-decane molecule, or also 40% - 80% of the width of any *n*-alkane molecule.

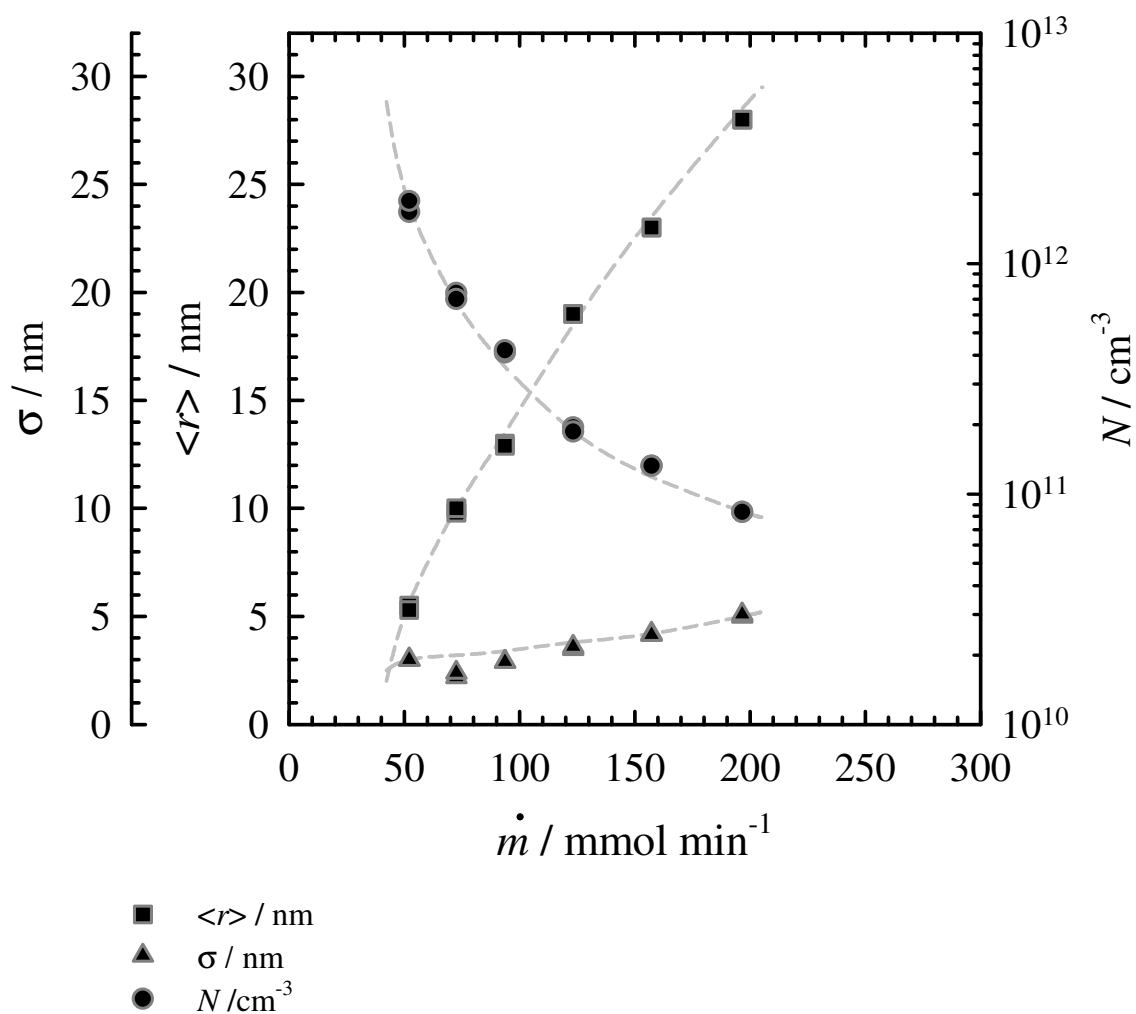


Figure 6.21: The mean radius $\langle r \rangle$ (squares), the width of the size distribution function σ (triangles) and the particle number density N (circles) as a function of the flow rate for *n*-heptane at $T_0=45^\circ\text{C}$ with Ar as carrier gas. The SAXS spectra were analyzed assuming a *Gaussian* distribution of droplets with a diffuse interface. The dashed lines are intended to guide the reader's eye.

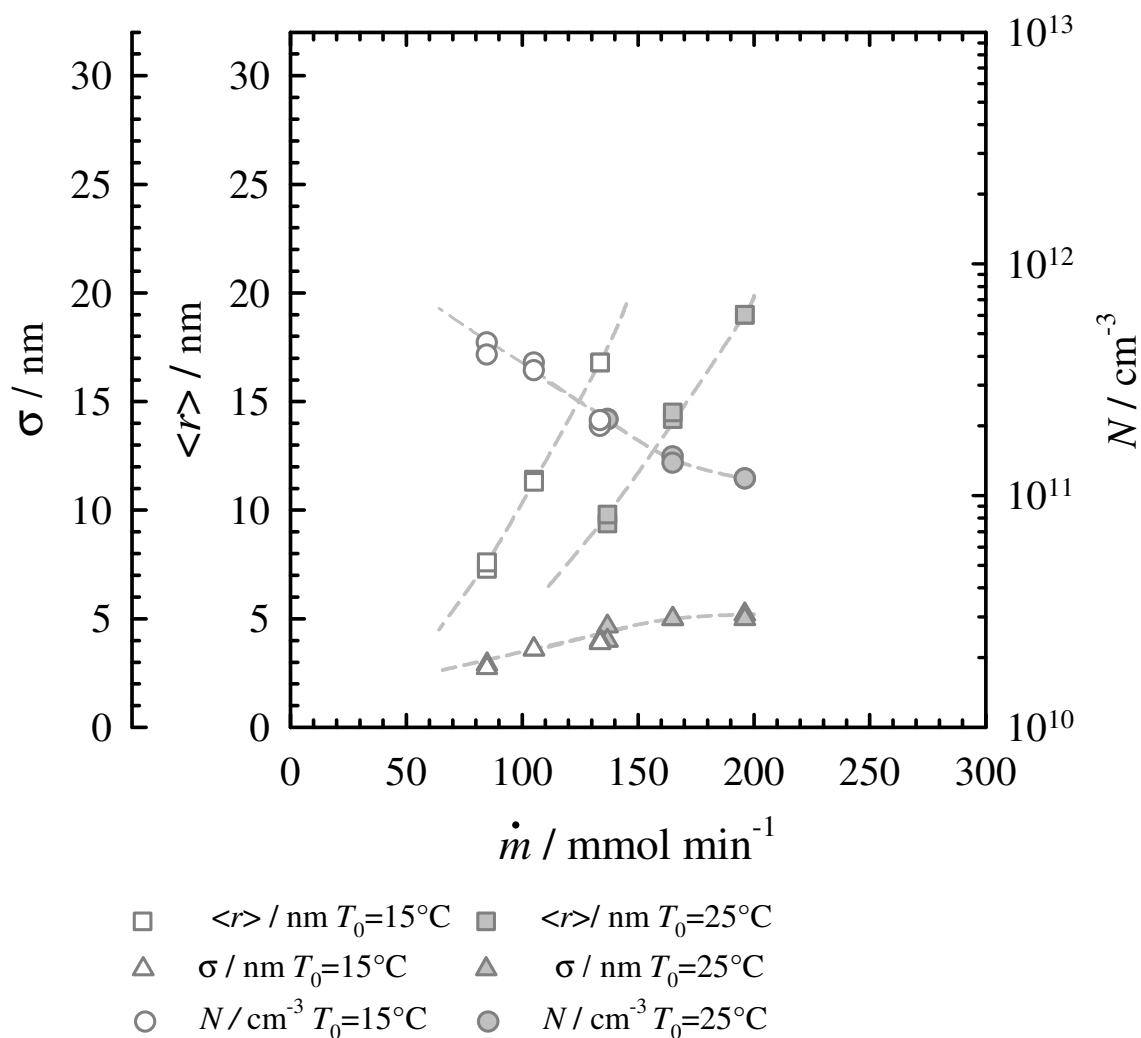


Figure 6.22: The mean radius $\langle r \rangle$ (squares), the width of the size distribution function σ (triangles) and the particle number density N (circles) as a function of the flow rate for n -octane at $T_0=15^\circ\text{C}$ (white coloured), and $T_0=25^\circ\text{C}$ (grey coloured). The carrier gas is N_2 in all cases. The SAXS spectra were analyzed assuming a *Gaussian* distribution of droplets with a diffuse interface. The dashed lines are intended to guide the reader's eye. The values of $\langle r \rangle$ are a strong function of T_0 , while N and σ are relatively insensitive to T_0 .

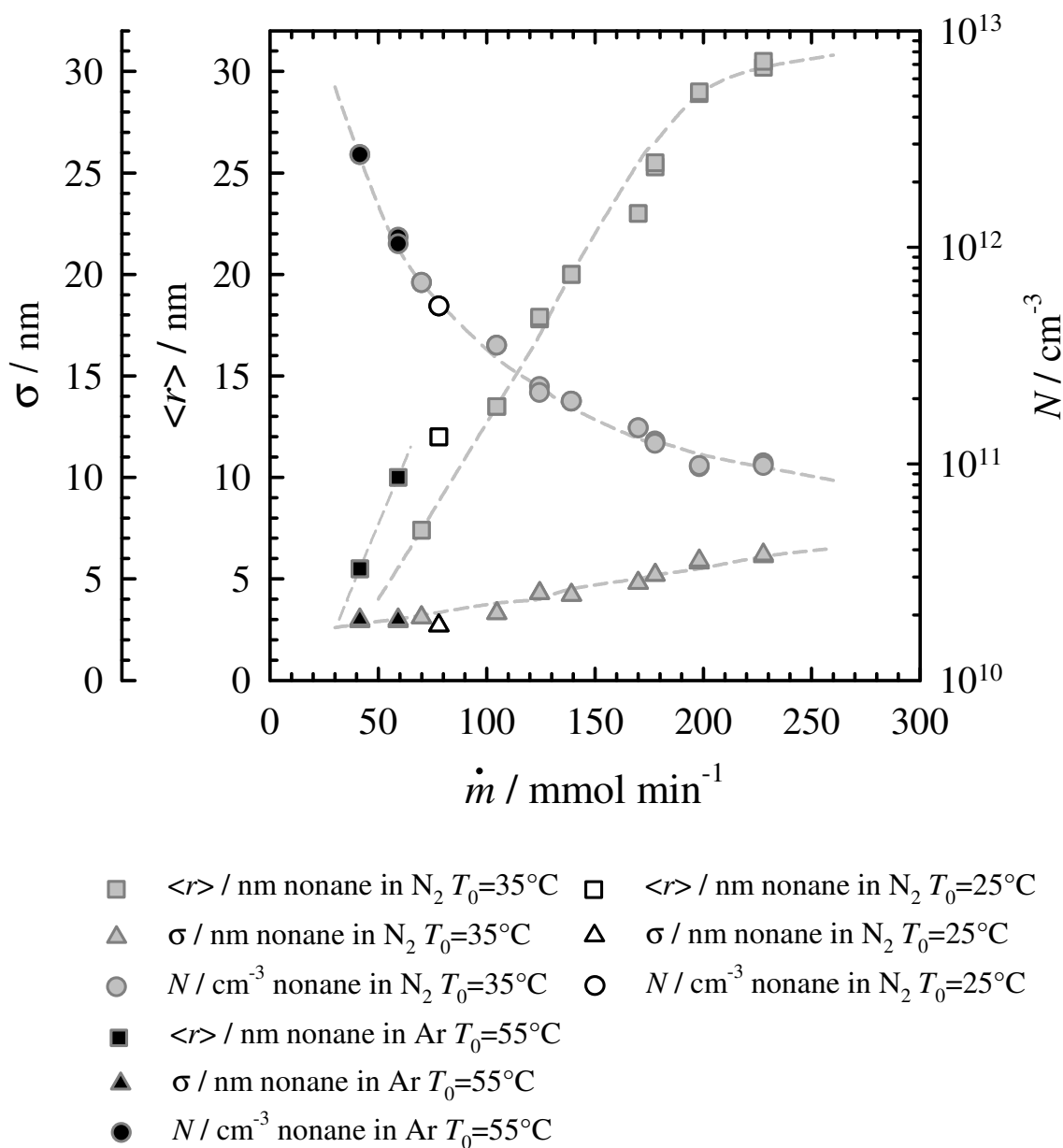


Figure 6.23: The mean radius $\langle r \rangle$ (squares), the width of the size distribution function σ (triangles) and the particle number density N (circles) as a function of the flow rate for n -nonane in N_2 at $T_0=25^\circ\text{C}$ (white coloured), n -nonane in N_2 at $T_0=35^\circ\text{C}$ (grey coloured), and n -nonane in Ar at $T_0=55^\circ\text{C}$ (dark coloured). The SAXS spectra were analyzed assuming a *Gaussian* distribution of droplets with a diffuse interface. The dashed lines are intended to guide the reader's eye. The values of $\langle r \rangle$ are a strong function of T_0 , while N and σ are relatively insensitive to T_0 .

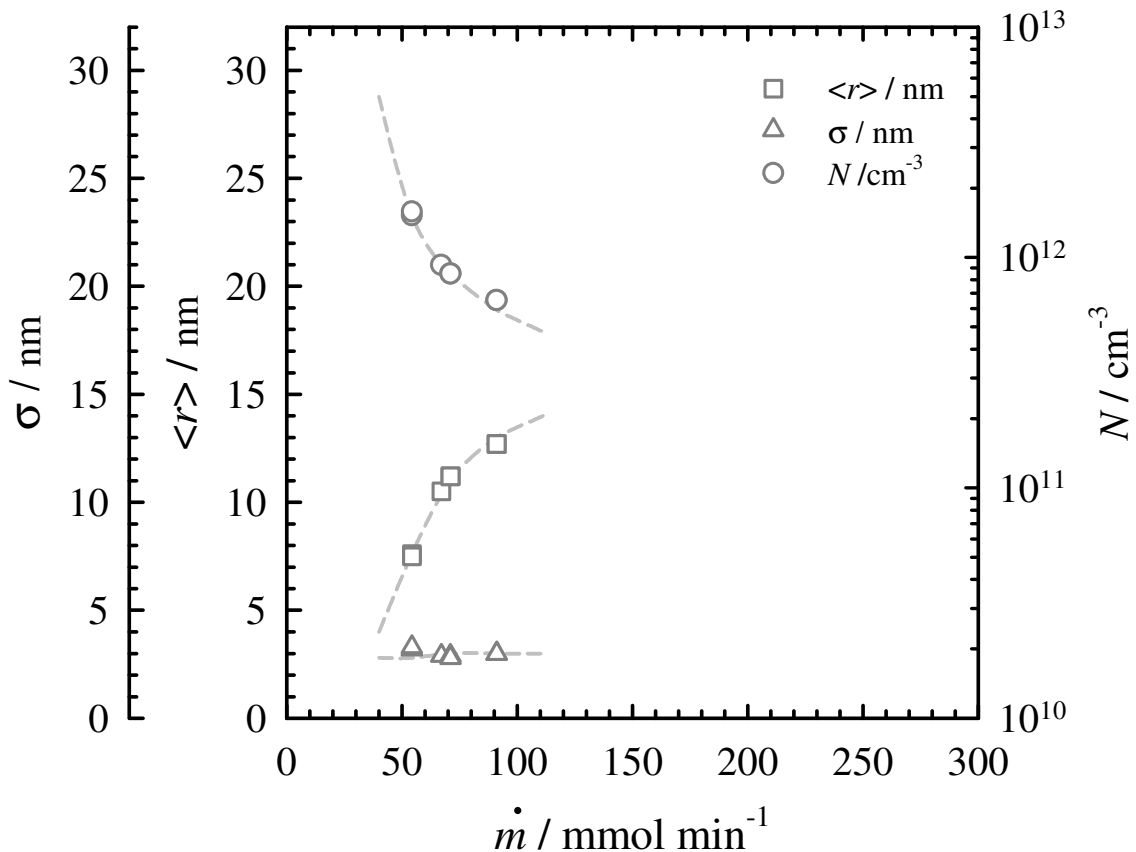


Figure 6.24: The mean radius $\langle r \rangle$ (squares), the width of the size distribution function σ (triangles) and the particle number density N (circles) as a function of the flow rate for n -decane at $T_0=35^\circ\text{C}$. The carrier gas was N_2 for all of the experiments. The SAXS spectra were analyzed assuming a *Gaussian* distribution of droplets with a diffuse interface. The dashed lines are intended to guide the reader's eye.

As noted for the n -alcohols, the change in particle number density with the n -alkane flow rate (Figure 6.21 – Figure 6.24) can be understood by recognizing that decreasing the condensable flow rate shifts nucleation to lower condensable partial pressures, lower temperatures and higher supersaturations. High supersaturations, in turn, means a stronger driving force for the nucleation process, and thus, a larger particle production rate $\int J(S,T)dt$. Thereto, the downstream condensation entails small values for the negative expansion rate $-\dot{p}/p_0$. Small values for the negative expansion rate correspond to a large characteristic time $\Delta t_{J_{\max}}$ (Figure 6.17). Low temperatures and low vapor phase concentrations both act to decrease the impingement rate of monomer onto the growing droplets. Thus, vapor phase depletion slows down and the time interval to quench nucleation increases. Increasing the characteristic time (in both cases) yields higher particle number

densities as long as the nucleation rate does not decrease significantly.

For the *n*-alkanes, the particle number density N is quite insensitive to changes in the plenum temperature T_0 (Figure 6.25). At $T_0 = 15^\circ\text{C}$ and an *n*-octane flow rate of $133.6 \text{ mmol min}^{-1}$ in N_2 , for example, a particle number density $N = 2.05 \cdot 10^{11} \text{ cm}^{-3}$ is measured, while at $T_0 = 25^\circ\text{C}$ and a flow rate of $136.8 \text{ mmol min}^{-1}$ a particle number density of $N = 2.1 \cdot 10^{11} \text{ cm}^{-3}$ is obtained, a difference of only a few percent. However, a dependency of the particle number density on the carrier gases can be observed. In Figure 6.25 the difference in slope for *n*-alkane runs in N_2 (high flow rates; empty and grey symbols) and in Ar (low flow rates; dark symbols) can be seen. Interestingly for all substances a good agreement in particle number densities N at $\sim 70 \text{ mmol min}^{-1}$ is observed, i.e. for *n*-heptane in Ar the particle number density is $N = 8 \cdot 10^{11} \text{ cm}^{-3}$, for *n*-octane in N_2 $N = 6 \cdot 10^{11} \text{ cm}^{-3}$, for *n*-nonane both in N_2 and Ar $N = 6.5 \cdot 10^{11} \text{ cm}^{-3}$, and for *n*-decane in N_2 $N = 9 \cdot 10^{11} \text{ cm}^{-3}$. Comparing the slopes of the measurements in N_2 and Ar, it can be noticed that at low flow rates the discrepancy between both sets of data can be as large as half an order of magnitude. To account for differences between the *n*-alkane flow rates used for SAXS and those used for the thermodynamic measurements, correlations for the particle number density N of each *n*-alkane in N_2 and Ar are developed, separately as a function of \dot{m} . Since there are no Small Angle X-ray Scattering measurements for *n*-octane in Ar and *n*-heptane in N_2 the mean interpolation function of *n*-nonane and *n*-heptane in Ar, and *n*-octane and *n*-nonane in N_2 is used to estimate the value for the particle number density N for *n*-octane in Ar and *n*-heptane in N_2 , respectively. For clarity reasons the particle number density for *n*-decane is omitted in Figure 6.25.

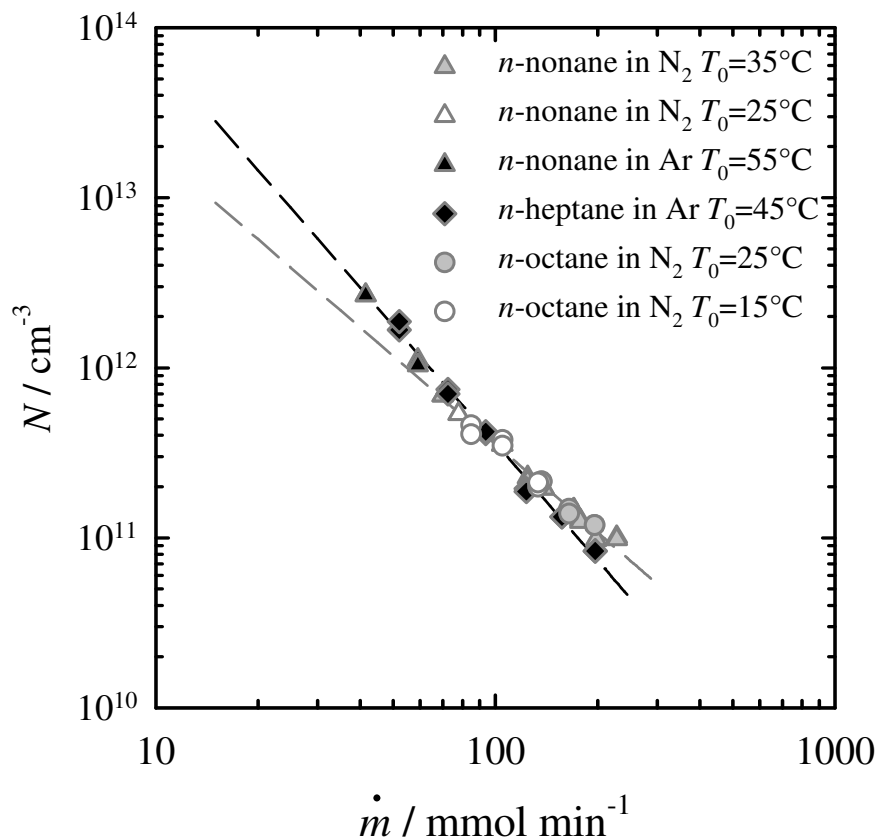


Figure 6.25: The particle number density as a function of molar flow rate for n -heptane in Argon at $T_0=45^\circ\text{C}$ (black diamonds), n -octane in N_2 at $T_0=15^\circ\text{C}$ (white circles) and $T_0=25^\circ\text{C}$ (grey circles), and n -nonane in N_2 at $T_0=25^\circ\text{C}$ (white triangles), $T_0=35^\circ\text{C}$ (grey triangles), and n -nonane in Ar at $T_0=55^\circ\text{C}$ (black triangles). A linear fit to the data in Ar (black dashed line) shows that the particle number density increases more rapidly with decreasing flow rate than for measurements in N_2 (grey dashed line). To estimate the particle number densities for the pressure trace measurements of n -octane in Ar a fit function for the combined data set of n -nonane and n -heptane in Ar is used.

The nucleation rates are calculated by combining the data from the pressure trace measurements and the Small Angle X-ray Scattering experiments using equation (1.1). For these experiments, the expansion rates of nozzles C (pressure trace measurements) and C2 (Small Angle X-ray Scattering) is close enough that it was not necessary to correct the particle number density N for differences in the opening angle (Figure 6.18).

Not only because of a nozzle with a large opening angle, and because of switching between nitrogen and argon as carrier gas, i.e. investigating the nucleation rate over a wide temperature regime $150 < T / \text{K} < 215$, but more importantly, because of the strong temperature dependency of the equilibrium vapor pressure of the n -alkanes⁸⁴ it is possible to

⁸⁴ Katz, 1970.

conduct measurements over several orders of magnitude of supersaturation $10^3 < S < 3 \cdot 10^7$ and nucleation rates $5 \cdot 10^{15} < J / \text{cm}^{-3} \text{s}^{-1} < 2 \cdot 10^{18}$. The measured nucleation rates $J(S, T)$, are summarized in Table 8.5. In Figure 6.26 the nucleation rate J is plotted vs. the supersaturation S corresponding to the maximum nucleation rate. Various systematic trends can be observed: Similar to previous H_2O and D_2O measurements⁸⁵ (and Figure 6.10) the nucleation rate increases with increasing supersaturation, or also with decreasing nucleation temperature (top value Figure 6.26). Furthermore, the nucleation rate is not only sensitive to the nucleation temperature and supersaturation but also to the expansion rate \dot{p}/p_0 (bottom value Figure 6.26). Nucleation for experiments starting from lower stagnation temperatures T_0 for a given molar flow rate \dot{m} occur further upstream. Here the negative expansion rate shows high values. The negative expansion rate indicates how strong the pressure changes per unit time during the phase transition. High values for the negative expansion rate correspond to states where the meta-stable regime is being probed with a sharp decline. Consequently, states of higher nucleation rates for the relaxation are reached. This behavior is confirmed by our data: Nearly one order of magnitude higher values for the nucleation rates are found for *n*-heptane in Ar at $T_0 = 6^\circ\text{C}$ with values for the expansion rate between $-1667 < \dot{p}/p_0 / \text{s}^{-1} < -1754$, compared to measurements in Ar at a plenum temperature $T_0 = 45^\circ\text{C}$ where the expansion rate is round about 1000 s^{-1} smaller for similar flow rates \dot{m} . Also *n*-octane verifies this trend. The nucleation rates for measurements conducted in N_2 at $T_0 = 15^\circ\text{C}$ which show expansion rates between $-1000 < \dot{p}/p_0 / \text{s}^{-1} < -1213$ lie half an order of magnitude higher compared to measurements conducted in N_2 at $T_0 = 25^\circ\text{C}$ with expansion rates between $-750 < \dot{p}/p_0 / \text{s}^{-1} < -1000$ at similar flow rates \dot{m} . Also *n*-nonane follows this behavior. For decreasing plenum temperature T_0 nucleation experiments at a similar condensible flow rate show higher nucleation rates.

⁸⁵ Kim *et al.*, 2004.

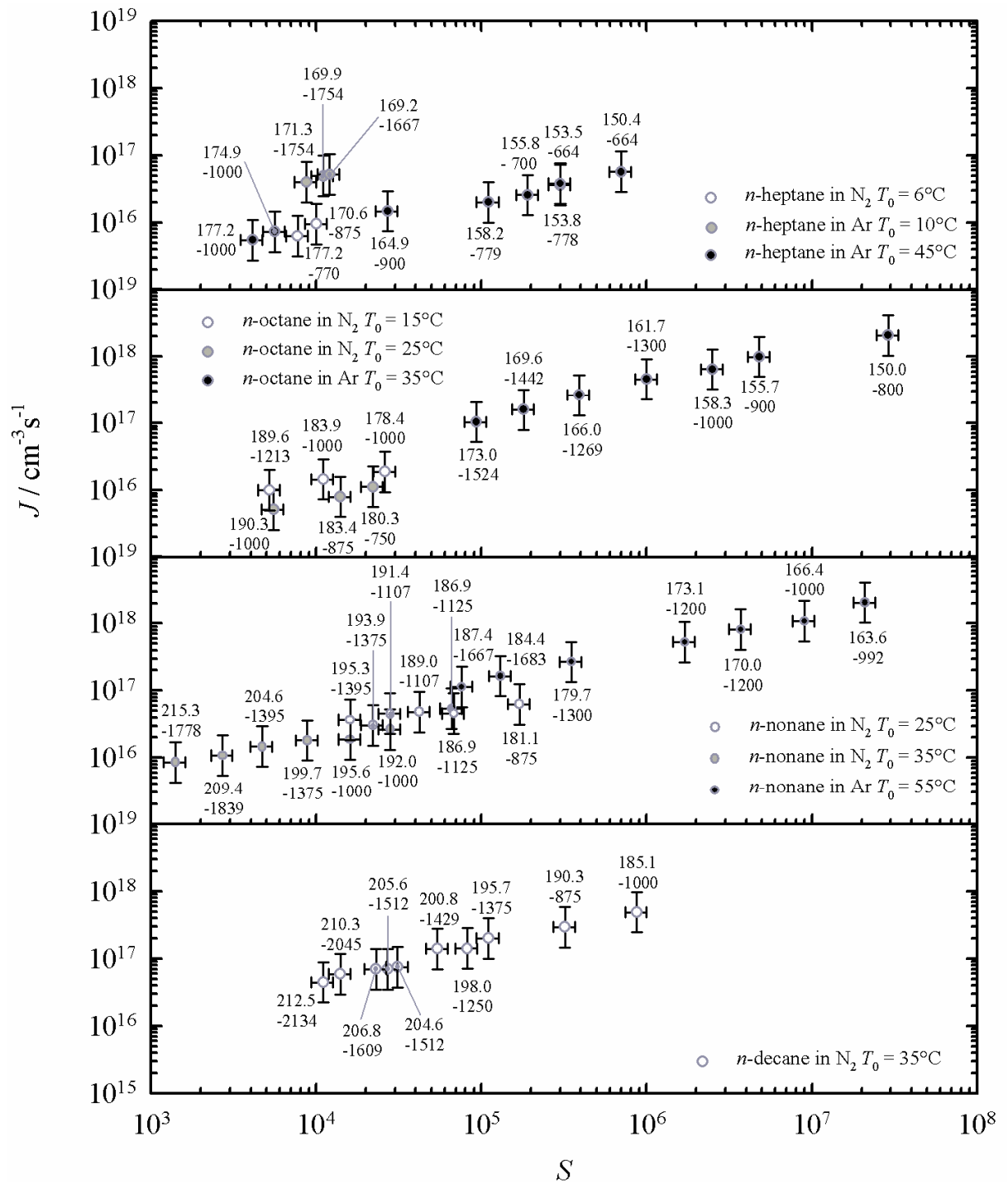


Figure 6.26: The experimental nucleation rate J vs. the supersaturation S for the homogeneous series of n -alkanes. The values for the nucleation temperature (top value) and the expansion rate (bottom value; negative value) are given.

Finally, *Hale's*⁸⁶ scaling theory is used, which enables a comparison of experimental results measured in different experimental setups, all serving different regimes of nucleation

⁸⁶ Hale, 1986; Hale, 1992.

rate, supersaturation, and temperature, to compare our results to those available in literature.⁸⁷ For this the parameter $C_0[(T_c/T)-1]^3/(\ln S)^2$ that simultaneously accounts for the temperature and supersaturation dependency in the exponent of the nucleation rate expression is plotted as a function of $-\ln(J/10^{26})$. By adjusting the parameter C_0 until the data conform to a straight line with a slope equal to 1, the effective value of Ω can be derived from C_0 by equation (6.1). Physically, Ω can be thought of as the surface entropy per molecule divided by the *Boltzmann* constant k .

It was not attempted to optimize the value of C_0 by a weighted least square fit in Figure 6.27, since it is not clear how to weight each individual set of data. To ensure comparability between the different sets of data the same expression for the equilibrium vapor pressure⁸⁸ for all sets of data has been used. Furthermore, for the *n*-nonane *Wagner* and *Strey*⁸⁹ data and for the *n*-nonane *Viisanen*, *Wagner* and *Strey*⁹⁰ data the expansion temperature T_{exp} , which was prior calculated by the *Poisson* equation (equation (2.24) with $\gamma=1.1$) has been recalculated by such means that the temperature dependency of the heat capacity⁸⁸ has been imbedded into the expression for the expansion temperature (equation (2.21)). Remarkably good agreements are found over ~ 21 orders of magnitude between the majority of the experimental results available in literature and those of this work (Figure 6.27). This is astonishing because not only do the nucleation rates differ by ~ 21 orders of magnitude, but the temperature and supersaturation regimes are often quite removed from each other, and in some cases the experimental techniques rely on very different physical phenomena. For *n*-nonane some of the data from *M. J. E. H. Muijtens*⁹¹, *C. C. M. Luitjens*⁹², and *P. Peters*⁹³ show a scatter from the behavior of the remaining literature data sets. A reason could be that these data were measured using methane as carrier gas. Due to the miscibility of *n*-nonane and methane it is no longer an ideal homogeneous system and it could be possible that also to an extent heterogeneous nucleation was measured. The discrepancies are enlarged for high initial pressure p_0 measurements. Since low pressures strive to an ideal vapor, it is evident that high pressures entail non ideal behavior in the gas phase. Furthermore, it is found that the scaling parameters $\Omega_{\text{heptane}}=2.31$, $\Omega_{\text{octane}}=2.40$,

⁸⁷ Wagner and Strey, 1984; Hung, Krasnopoler, and Katz, 1989; Muijtens, 1996; Rudek *et al.*, 1996; Luitjens, 1998; Viisanen, Wagner, and Strey, 1998; Peters, 2002.

⁸⁸ Katz, 1970.

⁸⁹ Wagner and Strey, 1984.

⁹⁰ Viisanen, Wagner, and Strey, 1998.

⁹¹ Muijtens, 1996.

⁹² Luitjens, 1998.

⁹³ Peters, 2002.

$\Omega_{\text{nonane}}=2.47$ and $\Omega_{\text{decane}}=2.55$ and the scaling factors shown by *Rusyniak* and *El-Shall*⁹⁴
 $\Omega_{\text{heptane}}=2.29$, $\Omega_{\text{octane}}=2.37$, $\Omega_{\text{nonane}}=2.44$ and $\Omega_{\text{decane}}=2.51$ agree well with each other.

⁹⁴ Rusyniak and El-Shall, 2001.

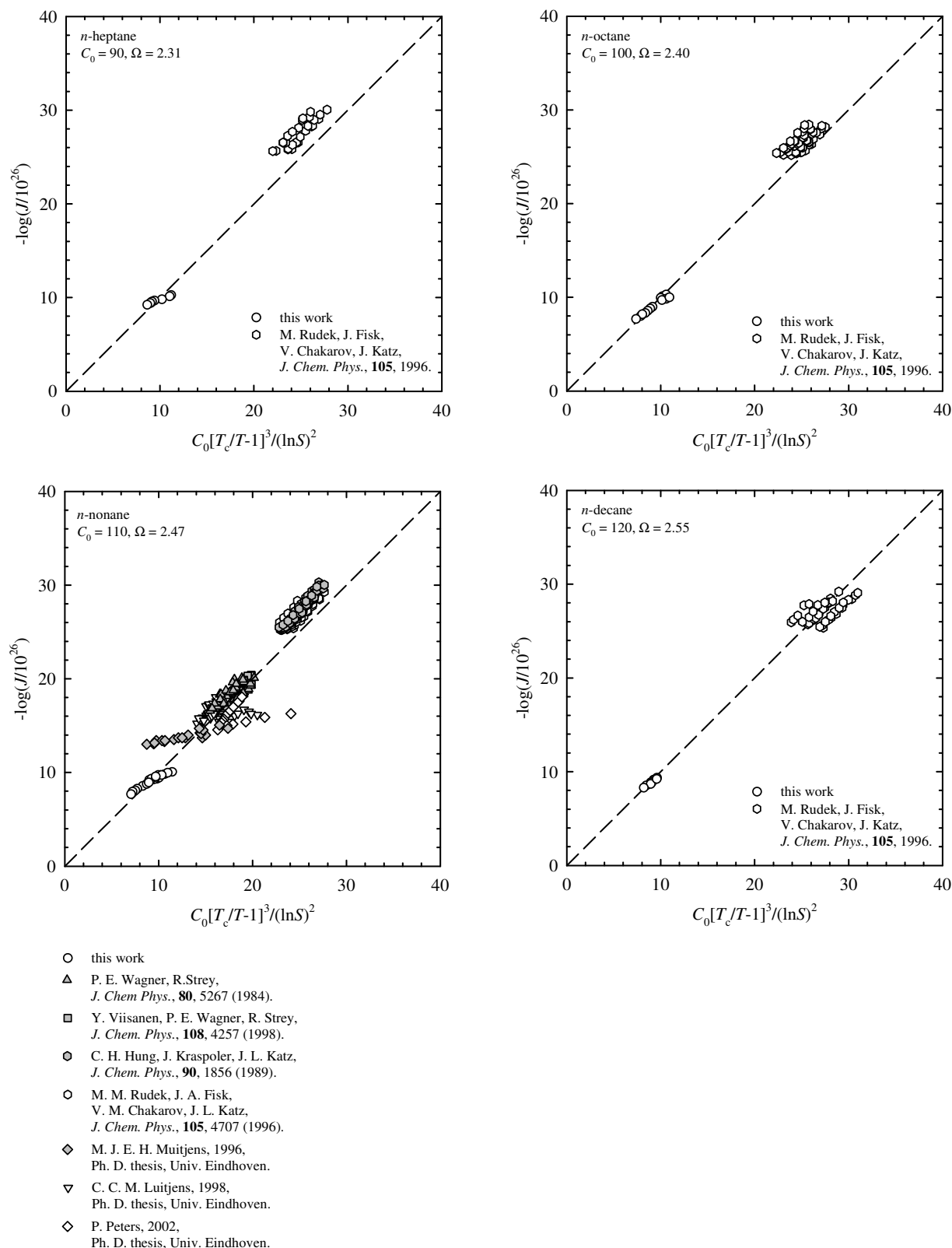


Figure 6.27: The *n*-alkane nucleation rates available in the literature are presented in a Hale plot. The expansion temperature T_{exp} , which was prior calculated by the Poisson equation (equation (2.24)) has been recalculated by such means that the temperature dependency of the heat capacity has been imbedded into the equation for the expansion temperature (equation (2.21)) for the *n*-nonane data by Wagner and Strey and the *n*-nonane data by Viisanen, Wagner and Strey.

7 Summary and Outlook

7.1 Summary

In most first-order phase transitions nucleation is the first step towards the formation of a new phase. Understanding the phenomenon of nucleation is of great interest in many fields of science, technology, and industrial processes. Although many efforts have been undertaken to clarify the nucleation process by several groups with various experimental devices all serving different regimes of nucleation rate, supersaturation, and temperature, the nucleation process is not fully understood up to date. In this work the nucleation behavior of n -alcohols and n -alkanes is investigated in a supersonic Laval nozzle by conducting two sets of experiments under identical conditions. First, static pressure measurements are carried out to determine the condensible partial pressure $p_{J_{\max}}$, the temperature $T_{J_{\max}}$, the supersaturation $S_{J_{\max}}$, the characteristic time $\Delta t_{J_{\max}}$, and the expansion rate \dot{p}/p_0 for the n -alkanes. For the n -alcohols these experiments have been carried out recently.⁹⁵ The pressure measurements build the basis for the second set of experiments, the first pioneering Small Angle X-ray Scattering experiments of aerosols in a supersonic nozzle, which give the mean radius $\langle r \rangle$, the width of the size distribution σ , and the particle number density N of the aerosols. Combining the results from the pressure trace measurements and the SAXS experiments reveals information on the nucleation rate $J = N / \Delta t_{J_{\max}}$ during supersonic nozzle expansion. Additionally, by analyzing the variation of the mean radius $\langle r \rangle$ and the width of the size distribution σ with the molar flow rate of condensible deepens the knowledge of nano-aerosol growth during supersonic nozzle expansion.

For the n -alkane pressure trace measurements the temperature dependency of the constant pressure heat capacity has been imbedded for the first time into the data analysis technique. Nucleation temperatures are found in the range of $207 \leq T / \text{K} \leq 249$ for the n -alcohols⁹⁵ and $143 \leq T / \text{K} \leq 215$ for the n -alkanes. Further, the characteristic times

⁹⁵ Gharibeh *et al.*, 2005.

$\Delta t_{J_{\max}}$ which are in the range of $6 \leq \Delta t_{J_{\max}} / \mu\text{s} \leq 22$ for the *n*-alcohols⁹⁶ and $13 \leq \Delta t_{J_{\max}} / \mu\text{s} \leq 34$ for the *n*-alkanes are determined. For the first time, it is recognized that the characteristic time $\Delta t_{J_{\max}}$ is sensitive to the expansion rate (Figure 6.17).

Under identical conditions as for the pressure measurements, e.g. the stagnation temperature T_0 , stagnation pressure p_0 , carrier gas, and condensible flow rate \dot{m} , SAXS experiments have been carried out. Particle number densities in the range of $1 \cdot 10^{12} < N / \text{cm}^{-3} < 5 \cdot 10^{12}$ and $1 \cdot 10^{11} < N / \text{cm}^{-3} < 3 \cdot 10^{12}$ for the *n*-alcohols and *n*-alkanes are found, respectively. The nucleation rate is then calculated by combining the data from the pressure trace measurements and the SAXS experiments. This leads to values in the range of $1 \cdot 10^{17} < J / \text{cm}^{-3} \text{s}^{-1} < 5 \cdot 10^{17}$ for the *n*-alcohols (Figure 6.10). For the *n*-alkanes nucleation rates in the range $5 \cdot 10^{15} < J / \text{cm}^{-3} \text{s}^{-1} < 2 \cdot 10^{18}$ are determined (Figure 6.26). The nucleation rate increases for both substance classes as the supersaturation increases and the temperature decreases. Furthermore, for the first time it is shown that the nucleation rate is also sensitive to the expansion rate $-\dot{p}/p_0$ during supersonic nozzle expansion. Finally, when comparing the nucleation rates of this work to those available in literature⁹⁷ a good agreement is found over ~ 21 orders of magnitude and the scaling parameters agree well with those shown by *Rusyniak and El-Shall*⁹⁸ and *Brus et al.*⁹⁹

Mean radii for the *n*-alcohols in the range of $4 < \langle r \rangle / \text{nm} < 10$ and for the *n*-alkanes in the range of $5 < \langle r \rangle / \text{nm} < 31$ are found. Additionally, a systematic variation of the size distribution parameters, e.g. the mean radius $\langle r \rangle$, the width of the size distribution σ , and the particle number density N , with the condensible flow rate \dot{m} are observed for the *n*-alcohols (Figure 6.3 - Figure 6.5) and the *n*-alkanes (Figure 6.21 - Figure 6.24): The mean radius $\langle r \rangle$ increases rapidly with the condensible flow rate \dot{m} . This is expected because the concentration of the condensible vapor is directly proportional to the condensible flow rate \dot{m} . For the *n*-alcohols the length of time available for growth, governed by varying the condensible flow rate \dot{m} or the plenum temperature T_0 , which leads to a shift of the maximum nucleation position, plays a minor role compared to the *n*-alkanes, where discon-

⁹⁶ Gharibeh *et al.*, 2005.

⁹⁷ Wagner and Strey, 1984; Kacker and Heist, 1985; Strey, Wagner, and Schmeling, 1986; Hung, Krasnopoler, and Katz, 1989; Viisanen and Strey, 1994; Strey, Viisanen, and Wagner, 1995; Hraby, Viisanen, and Strey, 1996; Muijtens, 1996; Rudek *et al.*, 1996; Luijten, Baas, and van Dongen, 1997; Luijtens, 1998; Viisanen, Wagner, and Strey, 1998; Zdimal and Smolik, 1998; Rudek *et al.*, 1999; Anisimov *et al.*, 2000; Graßmann and Peters, 2000; Lihavainen, Viisanen, and Kulmala, 2001b; Graßmann and Peters, 2002; Peters, 2002; Schmitt and Doster, 2002; Iland *et al.*, 2004b; Brus *et al.*, 2005; Brus, Zdimal, and Stratmann, 2006.

⁹⁸ Rusyniak and El-Shall, 2001.

⁹⁹ Brus, Zdimal, and Stratmann, 2006.

tinuities in the mean radius as a function of the flow rate \dot{m} can be observed for different plenum temperatures T_0 (Figure 6.22 - Figure 6.23). The width of the size distribution σ for the n -alcohols and n -alkanes also increases, however, only on a smaller scale as the condensible flow rate is increased. In contrast to the mean radius $\langle r \rangle$ and the width of the size distribution σ the particle number density N decreases rapidly because decreasing flow rates shift nucleation further downstream to low temperatures and high supersaturations where the particle production rate $\int J(S, T) dt$ and the characteristic times $\Delta t_{J_{\max}}$ are large.

7.2 Outlook

The results of this work suggest further investigations in many directions.

First, as this work reveals the nucleation behavior during supersonic nozzle expansion experiments are a multi-dimensional challenge. An important step towards understanding the phenomenon of nucleation is to reduce the dimensionality. A nozzle with a constant expansion rate \dot{p}/p_0 at every position can reduce one dimension of the challenge, and thus, simplify the interpretation of the experiments.

Further, during the Small Angle X-ray Scattering experiments the flow rate was varied. By this variation the dimensionality of the nucleation phenomenon increases since the nucleation position $x_{J_{\max}}$, the time of flight t_{tof} from the particle formation position to the detection position, the condensible partial pressure $p_{J_{\max}}$, the temperature $T_{J_{\max}}$, the supersaturation $S_{J_{\max}}$, the expansion rate \dot{p}/p_0 , and the reservoir are not constant. A different approach would be to conduct position resolved SAXS measurements at a given flow rate. Here a deeper understanding of the growth behavior can be won as the change in the radii of the aerosols can be followed at every position and temperature in the nozzle. The results presented in this work may be a valuable landmark for such future work.

Clearly, the homologous series of n -alcohols and n -alkanes can be extended. Preliminary n -undecane in N_2 measurements at plenum temperatures of $T_0 = 45^\circ\text{C}$ and $T_0 = 55^\circ\text{C}$ were carried out by *Dirk Bergmann* in 2005 in the aerosol laboratory of The Ohio State University. Deeper analysis is in progress for these measurements.

As the nucleation rate is a strong temperature and supersaturation dependent function experiments are enhanced by measurements made over a wide range of nucleation rates, temperatures, and supersaturations. Figure 6.11 and Figure 6.27 reveal a gap in the acces-

sible experimental nucleation rates between $10^{12} < J / \text{cm}^{-3}\text{s}^{-1} < 10^{16}$. Preliminary H_2O in Argon measurements in a two valve expansion chamber during which simply an expansion was carried out (Figure 7.1) have shown that experimental nucleation rates of $J = 10^{13} \pm 10^2$ can be achieved.¹⁰⁰ Consequently, the gap in accessible nucleation rate can be reduced. In fact, the analysis of these experiments is very similar to supersonic nozzle expansion experiments, since a similar pressure profile is measured. Also here the latent heat addition due to condensation is observed by a deviation of the wet condensing flow from an isentropic argon expansion. Currently a deeper data analysis technique is being developed by *Alexandra Manka*, for which the insides of this work can be a helpful guideline.

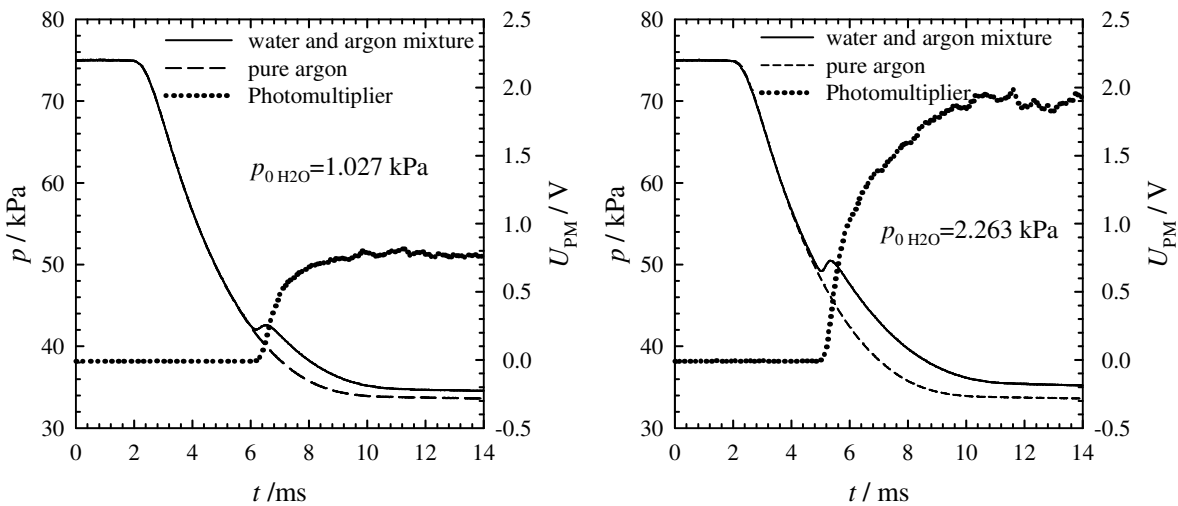


Figure 7.1: Preliminary H_2O results in the two valve expansion chamber during which simply an expansion was carried out. The solid line is the condensing pressure curve, the dashed line is the pressure for a pure argon expansion, and the light scattering signal of the photomultiplier is given by the dotted line vs. the time.

¹⁰⁰ Manka *et al.*, 2007.

Appendix

A.1 Chemicals

The condensible materials studied were *n*-propanol (99.5%, Sigma-Aldrich Co.), *n*-butanol (99.5%, Sigma-Aldrich Co.) and *n*-pentanol (99.5% Sigma-Aldrich Co.). The *n*-alcohols were not further purified. The *n*-pentanol used for the SAXS experiments was not from the lot distributed as part of the Workshop on *Nucleation Experiments – State of the Art and Future Developments* (Lot No. K21223075518, Merck, Germany). The carrier gas was nitrogen.

The thermo-physical properties of interest for the *n*-alcohols are summarized in Table 8.1. In our earlier work, we used the thermo-physical parameters given in Table 1 of *Schmeling and Strey*¹⁰¹ to evaluate the equilibrium vapor pressure. These parameters were derived by fitting only their experimental data to the *Dupré-Rankine* formula. Here, the parameters given in Table 2 of *Schmeling and Strey*¹⁰¹ are used because these are derived by fitting all of the available literature data, and are the expressions used by most other groups to calculate the supersaturation *S*.

The condensible materials including *n*-heptane (99+%), *n*-octane (99+%), *n*-nonane (99+%), and *n*-decane (99+%) were all purchased from Sigma-Aldrich Co. and were not further purified. Boil off from liquid nitrogen or argon Dewars provided the carrier gas. The thermo-physical properties of the *n*-alkanes are summarized in Table 8.2.

¹⁰¹ Schmeling and Strey, 1983.

A.2 *n*-Alcohol Parameters

Table 8.1: The thermo-physical properties of *n*-propanol, *n*-butanol, *n*-pentanol, and nitrogen. The properties are μ , the molecular weight; ρ_{SLD} , the scattering length density for the x-ray beam; and $p^\infty(T)$, the equilibrium vapor pressure,¹⁰² here T is given in Kelvin. The scattering length density is calculated as given in equation (4.28) and (4.29). For the scattering length density it has been accounted for, that the exit temperature of nozzle H2 is 6 K lower than that of nozzle A and a mean temperature has been used.

<i>n</i>-propanol	
$\mu / \text{g mol}^{-1}$	60.10
$\rho_{SLD} / \text{\AA}^{-2}$	$8.24 \cdot 10^{-6}$
$p^\infty(T) / \text{Pa}$	$133.322 \exp(84.7 - 8559.6/T - 9.29 \ln T)$
<i>n</i>-butanol	
$\mu / \text{g mol}^{-1}$	74.12
$\rho_{SLD} / \text{\AA}^{-2}$	$8.29 \cdot 10^{-6}$
$p^\infty(T) / \text{Pa}$	$133.322 \exp(93.6 - 9412.6/T - 10.54 \ln T)$
<i>n</i>-pentanol	
$\mu / \text{g mol}^{-1}$	88.15
$\rho_{SLD} / \text{\AA}^{-2}$	$8.31 \cdot 10^{-6}$
$p^\infty(T) / \text{Pa}$	$133.322 \exp(90.08 - 9788.4/T - 9.9 \ln T)$
nitrogen	
$\rho_{SLD} / \text{\AA}^{-2}$	$9.8 \cdot 10^{-9}$

¹⁰² Schmeling and Strey, 1983.

A.3 n-Alkane Parameters

Table 8.2: The thermo-physical properties of *n*-heptane, *n*-octane, *n*-nonane, and *n*-decane. The properties are μ , the molecular weight;¹⁰³ T_c , the critical temperature;¹⁰⁴ c_{pl} , the heat capacity of the liquid;¹⁰⁴ $c_p(T)$, the heat capacity of the vapor;¹⁰³ $p^\sigma(T)$, the equilibrium vapor pressure;¹⁰³ ρ_l , the density of the bulk liquid;¹⁰³ σ , the surface tension;¹⁰³ ΔH_{vap} , the heat of vaporization; ρ , the scattering length density for the x-ray beam, T is given in Kelvin; and R is the universal gas constant. The scattering length density is calculated as given in equation (4.28) and (4.29). For the scattering length density a mean nucleation temperature has been used.

<i>n</i>-heptane	
$\mu / \text{g mol}^{-1}$	100.206
T_c / K	540.2
p_c / MPa	2.74
$c_{pl}(\text{at } 298.15 \text{ K}) / \text{J g}^{-1} \text{ K}^{-1}$	2.25
$c_p(T) / \text{cal mol}^{-1} \text{ K}^{-1}$	$c_p = -8.49134 + 0.19666T - 1.16 \cdot 10^{-4} T^2$
$p^\sigma(T) / \text{Torr}$	$\log p_\sigma = 6.9024 - 1268.115 / (T - 56.25)$
$\rho_l / \text{g cm}^{-3}$	$\rho_l = 0.70048 - 8.476 \cdot 10^{-4} \cdot (T - 273.15) + 1.88 \cdot 10^{-7} \cdot (T - 273.15)^2 - 5.23 \cdot 10^{-9} \cdot (T - 273.15)^3$
$\sigma_{ST} / \text{N m}^{-1}$	$\sigma = (22.44 - 0.107 \cdot (T - 273.15)) / 1000$
$\Delta H_{\text{vap}} / \text{J mol}^{-1}$	$\Delta H_{\text{vap}} = R \cdot T^2 \cdot (\ln 10) \cdot 1268.115 / (T - 56.25)^2$
$\rho_{SLD} / \text{\AA}^{-2}$	8.24 $\cdot 10^{-6}$
<i>n</i>-octane	
$\mu / \text{g mol}^{-1}$	114.233
T_c / K	568.7
p_c / MPa	2.49
$c_{pl}(\text{at } 298.15 \text{ K}) / \text{J g}^{-1} \text{ K}^{-1}$	2.22
$c_p(T) / \text{cal mol}^{-1} \text{ K}^{-1}$	$c_p = 28.8144 + 0.01713T - 1.421 \cdot 10^{-4} T^2$
$p^\sigma(T) / \text{Torr}$	$\log p_\sigma = 6.92377 - 1355.126 / (T - 63.63)$
$\rho_l / \text{g cm}^{-3}$	$\rho_l = 0.71848 - 8.239 \cdot 10^{-4} \cdot (T - 273.15) + 4.459 \cdot 10^{-6} \cdot (T - 273.15)^2 - 5.293 \cdot 10^{-9} \cdot (T - 273.15)^3$
$\sigma_{ST} / \text{N m}^{-1}$	$\sigma = (23.52 - 0.09509 \cdot (T - 273.15)) / 1000$
$\Delta H_{\text{vap}} / \text{J mol}^{-1}$	$\Delta H_{\text{vap}} = R \cdot T^2 \cdot (\ln 10) \cdot 1355.126 / (T - 63.63)^2$
$\rho_{SLD} / \text{\AA}^{-2}$	8.29 $\cdot 10^{-6}$

¹⁰³ Katz, 1970.

¹⁰⁴ edited by Lide, 2003.

<i>n</i>-nonane	
$\mu / \text{g mol}^{-1}$	128.260
T_c / K	594.6
p_c / MPa	2.29
$c_{p1}(\text{at } 298.15 \text{ K}) / \text{J g}^{-1} \text{ K}^{-1}$	2.217
$c_p(T) / \text{cal mol}^{-1} \text{ K}^{-1}$	$c_p = 6.00821 + 0.16816T - 5.30 \cdot 10^{-5} \cdot T^2$
$p^\infty(T) / \text{Torr}$	$\log p_\infty = 6.93513 - 1428.811 / (T - 71.53)$
$\rho_l / \text{kg m}^{-3}$	$\rho_l = 0.7333 - 7.5 \cdot 10^{-4} \cdot (T - 273.15) + 4.55 \cdot 10^{-7} \cdot (T - 273.15)^2$
$\sigma_{ST} / \text{N m}^{-1}$	$\sigma = (24.72 - 0.09347 \cdot (T - 273.15)) / 1000$
$\Delta H_{\text{vap}} / \text{J/mol}$	$\Delta H_{\text{vap}} = R \cdot T^2 \cdot (\ln 10) \cdot 1428.811 / (T - 71.53)^2$
$\rho_{\text{SLD}} / \text{\AA}^{-2}$	8.31 · 10 ⁻⁶
<i>n</i>-decane	
$\mu / \text{g mol}^{-1}$	148.286
T_c / K	617.7
p_c / MPa	2.11
$c_{p1}(\text{at } 298.15 \text{ K}) / \text{J g}^{-1} \text{ K}^{-1}$	2.217
$c_p(T) / \text{J mol}^{-1} \text{ K}^{-1}$	$c_p = -70.37 + 1.232T - 8.646 \cdot 10^{-4} \cdot T^2 + 2.455 \cdot 10^{-7} \cdot T^3$
$p^\infty(T) / \text{Torr}$	$\log p_\infty = 4.06853 - 1495.170 / (T - 79.292)$
$\rho_l / \text{kg m}^{-3}$	$\rho_l = 60.9421 / 0.25745 \wedge (1 + (1 - T / 617.7) \wedge 0.28912)$
$\sigma_{ST} / \text{N m}^{-1}$	$\sigma = 0.02573 - 9.19 \cdot 10^{-5} \cdot (T - 273.15)$
$\Delta H_{\text{vap}} / \text{J/mol}$	$\Delta H_{\text{vap}} = R \cdot T^2 \cdot (\ln 10) \cdot 1495.170 / (T - 79.292)^2$
$\rho_{\text{SLD}} / \text{\AA}^{-2}$	8.31 · 10 ⁻⁶

A.4 *n*-Alcohol SAXS Results

Table 8.3: The results of the Small Angle X-ray Scattering experiments for *n*-propanol, *n*-butanol, and *n*-pentanol. The stagnation pressure is fixed at $p_0 = 30.2$ kPa; \dot{m} is the molar flow rate; T_0 is the stagnation temperature; “distribution” indicates which distribution function has been assumed; $\langle r \rangle$ is the mean radius; σ is the width of the distribution function, N is the particle number density; and P is the polydispersity index.

\dot{m} mmol min ⁻¹	T_0 / K	distribution	$\langle r \rangle$ / m ⁻⁹	σ / m ⁻⁹	N / 10 ¹² cm ⁻³	$P = \sigma / \langle r \rangle$
<i>n</i>-propanol						
41.10	308.15	<i>Gauss</i>	3.95	1.20	3.7	0.30
		<i>Schultz</i>	3.99	1.06	3.8	0.26
41.10	308.15	<i>Gauss</i>	3.80	1.20	4.4	0.32
		<i>Schultz</i>	3.73	1.15	4.6	0.31
58.24	308.15	<i>Gauss</i>	5.00	1.50	2.7	0.30
		<i>Schultz</i>	5.03	1.33	2.8	0.26
58.24	308.15	<i>Gauss</i>	5.00	1.60	2.5	0.32
		<i>Schultz</i>	5.01	1.35	2.8	0.27
75.71	308.15	<i>Gauss</i>	5.80	1.70	2.3	0.29
		<i>Schultz</i>	5.96	1.56	2.2	0.26
75.71	308.15	<i>Gauss</i>	6.00	1.70	2.1	0.28
		<i>Schultz</i>	6.01	1.55	2.1	0.26
69.88	318.15	<i>Gauss</i>	5.00	1.60	2.9	0.32
		<i>Schultz</i>	5.16	1.29	2.9	0.25
69.88	318.15	<i>Gauss</i>	5.20	1.40	2.9	0.27
		<i>Schultz</i>	5.14	1.34	2.9	0.26
69.88	318.15	<i>Gauss</i>	5.20	1.40	2.9	0.27
		<i>Schultz</i>	5.17	1.41	2.9	0.27
69.88	318.15	<i>Gauss</i>	5.20	1.40	2.9	0.27
		<i>Schultz</i>	5.34	1.33	2.6	0.25
100.67	318.15	<i>Gauss</i>	6.85	1.70	1.9	0.25
		<i>Schultz</i>	6.72	1.71	1.9	0.25
100.67	318.15	<i>Gauss</i>	6.70	1.60	2.1	0.24
		<i>Schultz</i>	6.73	1.68	1.9	0.25
101.16	318.15	<i>Gauss</i>	6.60	1.70	2.0	0.26
		<i>Schultz</i>	6.69	1.70	1.9	0.25
101.16	318.15	<i>Gauss</i>	6.60	1.70	2.1	0.26
		<i>Schultz</i>	6.65	1.71	1.9	0.26

\dot{m} mmol min ⁻¹	T_0 / K	distribution	$\langle r \rangle$ / m ⁻⁹	σ / m ⁻⁹	N / 10 ¹² cm ⁻³	$P = \sigma / \langle r \rangle$
139.27	318.15	<i>Gauss</i>	8.10	2.10	1.4	0.26
		<i>Schultz</i>	7.96	2.05	1.5	0.26
139.27	318.15	<i>Gauss</i>	8.10	2.10	1.4	0.26
		<i>Schultz</i>	8.13	2.05	1.4	0.25
139.77	318.15	<i>Gauss</i>	8.20	2.20	1.3	0.27
		<i>Schultz</i>	8.06	2.06	1.4	0.26
139.77	318.15	<i>Gauss</i>	8.20	2.10	1.4	0.26
		<i>Schultz</i>	8.09	2.04	1.4	0.25
70.55	323.15	<i>Gauss</i>	5.10	1.13	3.2	0.22
		<i>Schultz</i>	5.07	1.21	3.0	0.24
101.83	323.15	<i>Gauss</i>	6.40	1.60	2.3	0.25
		<i>Schultz</i>	6.45	1.63	2.1	0.25
101.83	323.15	<i>Gauss</i>	6.45	1.60	2.2	0.25
		<i>Schultz</i>	6.42	1.62	2.1	0.25
133.11	323.15	<i>Gauss</i>	7.60	2.00	1.5	0.26
		<i>Schultz</i>	7.56	1.84	1.6	0.24
133.11	323.15	<i>Gauss</i>	7.50	2.20	1.6	0.29
		<i>Schultz</i>	7.57	1.89	1.6	0.25
164.89	323.15	<i>Gauss</i>	8.40	2.30	1.4	0.27
		<i>Schultz</i>	8.39	2.11	1.4	0.25
164.89	323.15	<i>Gauss</i>	8.35	2.30	1.4	0.28
		<i>Schultz</i>	8.37	2.12	1.4	0.25
246.09	323.15	<i>Gauss</i>	10.05	2.70	1.0	0.27
		<i>Schultz</i>	10.05	2.50	1.0	0.25
246.09	323.15	<i>Gauss</i>	10.05	2.70	1.0	0.27
		<i>Schultz</i>	10.04	2.50	1.0	0.25
n-butanol						
31.17	308.15	<i>Gauss</i>	4.50	1.20	2.8	0.27
		<i>Schultz</i>	4.50	1.18	2.7	0.26
31.17	308.15	<i>Gauss</i>	4.40	1.20	3.1	0.27
		<i>Schultz</i>	4.46	1.22	2.8	0.27
32.11	323.15	<i>Gauss</i>	4.14	1.02	3.5	0.25
		<i>Schultz</i>	4.09	1.02	3.5	0.25
32.11	323.15	<i>Gauss</i>	3.64	1.37	4.2	0.28
		<i>Schultz</i>	3.82	1.11	4.4	0.29

\dot{m} mmol min ⁻¹	T_0 / K	distribution	$\langle r \rangle$ / m ⁹	σ / m ⁹	$N / 10^{12}$ cm ⁻³	$P = \sigma / \langle r \rangle$
56.26	323.15	<i>Gauss</i>	5.75	1.70	2.3	0.30
		<i>Schultz</i>	5.74	1.55	2.4	0.27
56.26	323.15	<i>Gauss</i>	5.65	1.70	2.4	0.30
		<i>Schultz</i>	5.75	1.52	2.3	0.26
82.03	323.15	<i>Gauss</i>	7.03	2.19	1.7	0.31
		<i>Schultz</i>	7.18	1.91	1.7	0.27
82.03	323.15	<i>Gauss</i>	7.20	2.00	1.7	0.28
		<i>Schultz</i>	7.25	1.89	1.7	0.26
107.93	323.15	<i>Gauss</i>	8.85	2.30	1.2	0.26
		<i>Schultz</i>	8.86	2.25	1.2	0.25
107.93	323.15	<i>Gauss</i>	8.82	2.30	1.2	0.26
		<i>Schultz</i>	8.85	2.27	1.2	0.26
n-pentanol						
20.53	318.15	<i>Gauss</i>	3.76	1.30	3.4	0.35
		<i>Schultz</i>	-	-	-	-
20.53	318.15	<i>Gauss</i>	3.78	1.27	3.3	0.34
		<i>Schultz</i>	-	-	-	-
31.76	318.15	<i>Gauss</i>	5.15	1.45	2.2	0.28
		<i>Schultz</i>	5.18	1.38	2.2	0.27
31.76	318.15	<i>Gauss</i>	4.91	1.59	2.4	0.32
		<i>Schultz</i>	5.18	1.40	2.2	0.27
24.05	333.15	<i>Gauss</i>	4.02	1.10	3.1	0.27
		<i>Schultz</i>	4.09	1.11	3.2	0.27
24.05	333.15	<i>Gauss</i>	4.02	1.10	3.1	0.27
		<i>Schultz</i>	4.09	1.02	3.2	0.25
44.36	333.15	<i>Gauss</i>	5.80	1.60	2.1	0.28
		<i>Schultz</i>	5.80	1.54	2.1	0.27
44.36	333.15	<i>Gauss</i>	5.75	1.60	2.1	0.28
		<i>Schultz</i>	5.85	1.51	2.0	0.26
69.77	333.15	<i>Gauss</i>	7.55	2.30	1.4	0.30
		<i>Schultz</i>	7.75	2.02	1.4	0.26
69.77	333.15	<i>Gauss</i>	7.59	2.20	1.4	0.29
		<i>Schultz</i>	7.64	2.00	1.4	0.26
89.73	333.15	<i>Gauss</i>	9.45	2.45	1.0	0.26
		<i>Schultz</i>	9.44	2.46	1.0	0.26
89.73	333.15	<i>Gauss</i>	9.58	2.45	1.0	0.26
		<i>Schultz</i>	9.49	2.45	1.0	0.26

A.5 n-Alcohol Nucleation Rates

Table 8.4: The combination of the data obtained from the pressure trace measurements and the Small Angle X-ray Scattering experiments of *n*-propanol, *n*-butanol, and *n*-pentanol. The stagnation pressure for the Small Angle X-ray Scattering experiments is fixed at $p_0 = 30.2$ kPa; \dot{m} is the molar flow rate; T_0 is the stagnation temperature; $p_{J_{\max}}$, $S_{J_{\max}}$, $T_{J_{\max}}$, and $\Delta t_{J_{\max}}$ are the pressure, temperature, supersaturation, and the characteristic time corresponding to the maximum nucleation rate J_{\max} (these values are from previous pressure trace measurements¹⁰⁵ and have been conducted at $p_0 = 59.6$ kPa), respectively, N_{Gaussian} , and N_{Schultz} are the particle number density assuming a *Gaussian* or a *Schultz* distribution function, respectively, $\rho_{\text{NZ}}/\rho_{\text{VV}}$ is the density ratio of the gas at the nucleation zone to the viewing volume, and J_{Gaussian} , and J_{Schultz} are the nucleation rate corresponding to N_{Gaussian} and N_{Schultz} , respectively. The values for the pressure $p_{J_{\max}}$ and temperature $T_{J_{\max}}$ corresponding to the maximum nucleation rate are identical to those reported in an earlier publication.¹⁰⁵ However, the values for the supersaturation $S_{J_{\max}}$ differ from those reported earlier¹⁰⁵ because of the use of a different equilibrium vapor pressure function.¹⁰⁶

\dot{m} mmolmin ⁻¹	T_0 / K	$T_{J_{\max}}$ K	$p_{J_{\max}}$ Pa	$S_{J_{\max}}$	$\Delta t_{J_{\max}}$ μs	N_{Gaussian} 10^{12}cm^{-3}	N_{Schultz} 10^{12}cm^{-3}	$\rho_{\text{NZ}}/\rho_{\text{VV}}$	J_{Gaussian} $10^{17}\text{cm}^{-3}\text{s}^{-1}$	J_{Schultz} $10^{17}\text{cm}^{-3}\text{s}^{-1}$
<i>n</i>-propanol										
67.7	323.15	219.73	61	35.5	12.5	2.3	2.3	1.05	1.9	2.0
93.0	323.15	224.40	90	28.3	10.0	1.8	1.8	1.10	2.0	2.0
134.4	323.15	229.99	140	21.9	9.0	1.3	1.3	1.16	1.7	1.7
167.2	323.15	233.53	183	18.7	9.4	1.1	1.1	1.20	1.4	1.4
247.9	323.15	239.64	293	15.0	8.1	0.9	0.9	1.26	1.3	1.3
67.7	318.15	219.87	62	35.4	12.0	2.3	2.3	1.10	2.1	2.1
134.3	318.15	229.81	142	22.7	10.2	1.3	1.3	1.21	1.6	1.6
22.0	308.15	207.20	19	67.5	17.6	5.5	5.7	1.04	3.3	3.4
28.6	308.15	210.51	26	55.9	14.9	4.5	4.6	1.08	3.3	3.3
33.8	308.15	212.97	32	47.9	13.2	3.9	4.0	1.11	3.3	3.4
50.7	308.15	219.10	52	32.9	12.1	2.9	2.9	1.19	2.8	2.9
67.2	308.15	223.36	74	26.6	11.4	2.3	2.3	1.24	2.5	2.5

¹⁰⁵ Gharibeh *et al.*, 2005.

¹⁰⁶ Schmeling and Strey, 1983.

\dot{m} mmolmin ⁻¹	T_0 / K	T_{Jmax} K	p_{Jmax} Pa	S_{Jmax}	Δt_{Jmax} μ s	$N_{Gaussian}$ 10 ¹² cm ⁻³	$N_{Schultz}$ 10 ¹² cm ⁻³	ρ_{NZ}/ρ_{VV}	$J_{Gaussian}$ 10 ¹⁷ cm ⁻³ s ⁻¹	$J_{Schultz}$ 10 ¹⁷ cm ⁻³ s ⁻¹
<i>n</i>-butanol										
29.1	323.15	221.63	27	66.7	11.5	3.6	3.7	1.09	3.4	3.5
38.6	323.15	226.32	38	48.5	9.4	2.8	2.8	1.14	3.4	3.4
56.5	323.15	231.75	60	37.1	8.8	1.9	2.0	1.21	2.7	2.7
70.4	323.15	235.33	79	31.0	8.6	1.6	1.6	1.25	2.3	2.3
111.7	323.15	242.47	138	22.8	6.2	1.0	1.0	1.33	2.2	2.2
11.7	308.15	210.75	10	130.1	22.0	8.5	8.7	1.09	4.2	4.3
13.1	308.15	212.84	12	111.7	16.2	7.7	7.8	1.12	5.3	5.4
17.3	308.15	217.10	17	81.9	16.3	5.9	6.0	1.17	4.2	4.3
21.9	308.15	219.79	22	71.0	11.9	4.7	4.8	1.20	4.8	4.9
28.9	308.15	224.94	32	49.4	13.1	3.7	3.7	1.28	3.6	3.6
<i>n</i>-pentanol										
24.8	333.15	228.54	22	117.5	12.9	2.6	2.4	1.09	2.2	2.1
37.1	333.15	233.91	37	89.0	12.7	1.9	1.8	1.14	1.7	1.6
49.5	333.15	238.78	52	65.3	11.4	1.5	1.4	1.20	1.5	1.5
59.0	333.15	241.86	65	55.0	11.7	1.3	1.2	1.24	1.4	1.3
73.6	333.15	245.90	86	44.1	13.9	1.1	1.0	1.28	1.0	1.0
92.8	333.15	248.93	113	40.3	11.2	0.9	0.9	1.32	1.0	1.0
12.5	318.15	222.79	12	155.9	17.2	4.4	4.2	1.16	3.0	2.8
15.0	318.15	225.48	15	128.0	15.8	3.8	3.6	1.19	2.9	2.7
18.6	318.15	228.08	20	109.2	11.7	3.2	3.1	1.22	3.4	3.2
24.6	318.15	232.53	28	81.4	11.3	2.6	2.5	1.28	2.9	2.8
31.0	318.15	236.39	38	65.4	10.5	2.1	2.1	1.33	2.7	2.6

A.6 n-Alkane Pressure Trace Measurements and Nucleation Rates

Table 8.5: The results from the pressure trace measurements for *n*-heptane, *n*-octane, *n*-nonane, and *n*-decane are summarized. The stagnation pressure for the pressure trace measurements is fixed at $p_0 = 30.2$ kPa with an exception of 11 *n*-nonane runs (values with asterisk) which were performed at $p_0 = 59.6$ kPa in 2003 at the Worcester Polytechnic Institute with an experimental setup described in *Gharibeh et al.*¹⁰⁷ The column “carrier gas” indicates which carrier gas is used; \dot{m} is the molar flow rate; y is the vapor fraction of the condensible species; T_0 is the stagnation temperature, $p_{J_{\max}}$, $T_{J_{\max}}$, $S_{J_{\max}}$, and $\Delta t_{J_{\max}}$ are the pressure, temperature, supersaturation, and the characteristic time corresponding to the maximum nucleation rate J_{\max} ; $d(p/p_0)/dt$ is the expansion rate; $\rho_{\text{NZ}}/\rho_{\text{VV}}$ is the density ratio of the gas at the nucleation zone to the viewing volume. The particle number density N and the nucleation rate J is obtained by combining the data from the pressure trace measurements and the Small Angle X-ray Scattering experiments (Table 8.6). The stagnation pressure for the Small Angle X-ray Scattering experiments is fixed at $p_0 = 30.2$ kPa. For the Small Angle X-ray Scattering experiments a *Gaussian* distribution of particles was assumed.

carrier gas	\dot{m} mmol min ⁻¹	y	T_0 K	$p_{J_{\max}}$ Pa	$T_{J_{\max}}$ K	$S_{J_{\max}}$	\dot{p}/p_0 s ⁻¹	$\Delta t_{J_{\max}}$ 10 ⁵ s	N /cm ⁻³	$\rho_{\text{NZ}}/\rho_{\text{VV}}$	J /cm ⁻³ s ⁻¹
<i>n</i>-heptane											
N ₂	152.5	0.0161	279.39	76.72	170.06	1.00·10 ⁴	-875	2.02	1.72·10 ¹¹	1.1	9.52·10 ¹⁵
N ₂	185.2	0.0197	279.42	96.93	172.30	7.70·10 ³	-770	2.10	1.24·10 ¹¹	1.1	6.28·10 ¹⁵
Ar	88.4	0.0106	283.15	80.67	169.86	1.10·10 ⁴	-1754	1.26	4.79·10 ¹¹	1.3	4.95·10 ¹⁶
Ar	96.2	0.0116	283.15	88.01	171.30	8.70·10 ³	-1754	1.27	3.95·10 ¹¹	1.3	3.99·10 ¹⁶
Ar	84.9	0.0102	283.15	75.56	169.19	1.20·10 ⁴	-1667	1.27	5.26·10 ¹¹	1.3	5.19·10 ¹⁶
Ar	195.4	0.0252	318.13	142.76	177.19	4.10·10 ³	-1000	1.65	7.8·10 ¹⁰	1.2	5.45·10 ¹⁵
Ar	166.3	0.0214	318.15	121.09	174.85	5.60·10 ³	-1000	1.80	1.1·10 ¹¹	1.2	7.27·10 ¹⁵
Ar	98.4	0.0126	318.13	60.95	164.88	2.70·10 ⁴	-900	2.85	3.8·10 ¹¹	1.1	1.47·10 ¹⁶
Ar	59.5	0.0075	318.13	29.33	153.52	3.00·10 ⁵	-664	3.44	1.2·10 ¹²	1.0	3.61·10 ¹⁶
Ar	79.1	0.0101	318.14	42.43	158.18	1.10·10 ⁵	-779	3.28	6.2·10 ¹¹	1.1	2.00·10 ¹⁶
Ar	69.5	0.0088	318.15	37.17	155.82	1.90·10 ⁵	-700	3.43	8.4·10 ¹¹	1.1	2.57·10 ¹⁶
Ar	59.4	0.0075	318.14	32.17	153.82	3.00·10 ⁵	-779	3.35	1.2·10 ¹²	1.1	3.79·10 ¹⁶
Ar	49.3	0.0062	318.13	25.14	150.38	7.00·10 ⁵	-664	3.35	1.8·10 ¹²	1.0	5.71·10 ¹⁶
Ar	39.4	0.0050	318.13	18.83	146.94	1.70·10 ⁶	-664	-	-	-	-
Ar	29.6	0.0037	318.14	13.71	143.07	5.20·10 ⁶	-664	-	-	-	-

¹⁰⁷ Gharibeh *et al.*, 2005.

carrier gas	\dot{m} mmol min ⁻¹	y	T_0 K	p_{Jmax} Pa	T_{Jmax} K	S_{Jmax}	\dot{p} / p_0 s ⁻¹	Δt_{Jmax} 10 ⁵ s	N / cm^{-3}	ρ_{N2} / ρ_{VV}	$J / \text{cm}^{-3} \text{s}^{-1}$
n-octane											
N ₂	85.2	0.0092	298.13	41.24	175.66	4.60·10 ⁴	-625				
N ₂	142.7	0.0156	298.14	76.26	183.42	1.40·10 ⁴	-875	2.53	1.9·10 ¹¹	1.0	7.97·10 ¹⁵
N ₂	204.7	0.0227	298.12	124.26	190.34	5.50·10 ³	-1000	2.29	1.1·10 ¹¹	1.1	5.14·10 ¹⁵
N ₂	115.8	0.0126	298.12	59.44	180.28	2.20·10 ⁴	-750	2.50	2.7·10 ¹¹	1.0	1.13·10 ¹⁶
N ₂	112.0	0.0119	287.99	65.77	183.85	1.10·10 ⁴	-1000	2.30	2.9·10 ¹¹	1.2	1.45·10 ¹⁶
N ₂	84.2	0.0089	288.02	45.43	178.41	2.60·10 ⁴	-1000	2.70	4.6·10 ¹¹	1.1	1.89·10 ¹⁶
N ₂	154.4	0.0164	288.03	101.86	189.61	5.20·10 ³	-1213	2.07	1.7·10 ¹¹	1.2	1.00·10 ¹⁶
N ₂	59.4	0.0063	288.01	29.94	172.60	7.30·10 ⁴	-875	-			-
N ₂	46.6	0.0049	288.04	20.78	168.18	1.70·10 ⁵	-625	-			-
Ar	53.4	0.0067	308.12	42.68	173.03	9.30·10 ⁴	-1524	1.89	1.5·10 ¹²	1.3	1.04·10 ¹⁷
Ar	44.3	0.0055	308.14	33.19	169.64	1.80·10 ⁵	-1442	1.92	2.3·10 ¹²	1.3	1.58·10 ¹⁷
Ar	35.3	0.0044	308.15	25.10	165.98	3.90·10 ⁵	-1269	1.95	4.0·10 ¹²	1.3	2.64·10 ¹⁷
Ar	26.3	0.0033	308.14	17.01	161.70	1.00·10 ⁶	-1300	2.24	8.2·10 ¹²	1.2	4.56·10 ¹⁷
Ar	17.0	0.0021	308.15	10.38	155.73	4.80·10 ⁶	-900	2.87	2.4·10 ¹³	1.2	9.94·10 ¹⁷
Ar	8.5	0.0011	308.14	4.20	144.99	1.70·10 ⁸	-664	-			-
Ar	21.1	0.0026	308.11	13.33	158.25	2.50·10 ⁶	-1000	2.66	1.4·10 ¹³	1.2	6.46·10 ¹⁷
Ar	12.3	0.0015	308.13	6.65	150.01	2.90·10 ⁷	-800	2.91	5.3·10 ¹³	1.1	2.08·10 ¹⁸
n-nonane											
N ₂ *	60.7	0.0033	298.10	38.59	191.39	2.80·10 ⁴	-1107	2.27	8.5·10 ¹¹	1.2	4.54·10 ¹⁶
N ₂ *	45.8	0.0025	298.11	27.27	186.35	6.60·10 ⁴	-1125	2.92	1.4·10 ¹²	1.2	5.41·10 ¹⁶
N ₂ *	76.0	0.0041	298.11	52.83	195.33	1.60·10 ⁴	-1395	1.97	5.7·10 ¹¹	1.3	3.68·10 ¹⁶
N ₂ *	38.0	0.0021	298.14	18.29	181.20	1.70·10 ⁵	-875	3.22	1.9·10 ¹²	1.1	6.27·10 ¹⁶
N ₂ *	53.9	0.0029	298.14	33.36	189.03	4.20·10 ⁴	-1107	2.54	1.0·10 ¹²	1.2	4.83·10 ¹⁶
N ₂ *	91.1	0.0051	308.12	55.97	195.60	1.60·10 ⁴	-1000	2.58	4.2·10 ¹¹	1.2	1.88·10 ¹⁶
N ₂ *	136.8	0.0076	308.11	99.37	204.63	4.70·10 ³	-1395	1.81	2.1·10 ¹¹	1.3	1.47·10 ¹⁶
N ₂ *	226.7	0.0124	308.11	186.53	215.34	1.40·10 ³	-1778	1.43	8.7·10 ¹⁰	1.4	8.58·10 ¹⁵
N ₂ *	172.6	0.0095	308.12	134.72	209.42	2.70·10 ³	-1839	1.72	1.4·10 ¹¹	1.3	1.08·10 ¹⁶
N ₂ *	107.3	0.0060	308.13	72.05	199.71	8.80·10 ³	-1375	2.11	3.2·10 ¹¹	1.2	1.82·10 ¹⁶
N ₂ *	70.9	0.0040	308.11	44.25	191.99	2.80·10 ⁴	-1000	2.74	6.5·10 ¹¹	1.1	2.65·10 ¹⁶
N ₂	37.5	0.0041	298.11	19.85	180.10	2.50·10 ⁵	-1000	-			-
N ₂	53.3	0.0058	298.15	31.81	186.85	6.80·10 ⁴	-1125	2.46	1.1·10 ¹²	1.1	4.57·10 ¹⁶
N ₂	75.6	0.0084	298.13	53.01	193.88	2.20·10 ⁴	-1375	2.23	5.8·10 ¹¹	1.2	3.05·10 ¹⁶
Ar	32.1	0.0041	328.10	25.12	179.74	3.50·10 ⁵	-1300	2.53	5.2·10 ¹²	1.3	2.68·10 ¹⁷
Ar	24.3	0.0031	328.16	16.56	173.07	1.70·10 ⁶	-1200	2.47	1.1·10 ¹³	1.2	5.32·10 ¹⁷
Ar	18.9	0.0024	328.12	12.95	169.96	3.70·10 ⁶	-1200	3.02	2.0·10 ¹³	1.2	8.17·10 ¹⁷
Ar	16.2	0.0021	328.14	10.55	166.84	9.00·10 ⁶	-1000	3.32	3.0·10 ¹³	1.2	1.08·10 ¹⁸
Ar	40.0	0.0052	328.16	32.91	184.42	1.30·10 ⁵	-1683	2.38	2.9·10 ¹²	1.3	1.65·10 ¹⁷
Ar	48.2	0.0063	328.17	40.21	187.35	7.60·10 ⁴	-1667	2.17	1.8·10 ¹²	1.4	1.14·10 ¹⁷
Ar	12.4	0.0016	328.12	7.27	163.59	2.10·10 ⁷	-992	3.39	6.0·10 ¹³	1.2	2.05·10 ¹⁸

carrier	\dot{m}		T_0	$p_{J_{\max}}$	$T_{J_{\max}}$		\dot{p} / p_0	$\Delta t_{J_{\max}}$			
gas	mmol min ⁻¹	y	K	Pa	K	$S_{J_{\max}}$	s ⁻¹	10 ⁵ s	N / cm^{-3}	ρ_{N_2} / ρ_{N_2}	$J / \text{cm}^{-3}\text{s}^{-1}$
n-decane											
N ₂	59.5	0.0067	308.14	42.36	204.59	3.10·10 ⁴	-1512	2.12	1.3·10 ¹²	1.3	7.47·10 ¹⁶
N ₂	61.7	0.0069	308.16	46.26	205.63	2.70·10 ⁴	-1512	2.15	1.2·10 ¹²	1.3	6.98·10 ¹⁶
N ₂	64.8	0.0073	308.12	50.18	206.76	2.30·10 ⁴	-1609	2.01	1.0·10 ¹²	1.3	6.96·10 ¹⁶
N ₂	36.9	0.0041	308.11	24.20	197.97	8.20·10 ⁴	-1250	2.33	2.8·10 ¹²	1.2	1.42·10 ¹⁷
N ₂	44.2	0.0049	308.15	31.03	200.76	5.40·10 ⁴	-1428	1.83	2.0·10 ¹²	1.3	1.40·10 ¹⁷
N ₂	22.8	0.0025	308.15	12.83	190.33	3.20·10 ⁵	-875	2.73	6.2·10 ¹²	1.3	2.94·10 ¹⁷
N ₂	29.5	0.0033	308.14	18.63	195.74	1.10·10 ⁵	-1375	2.37	4.0·10 ¹²	1.2	2.01·10 ¹⁷
N ₂	16.3	0.0018	308.15	7.63	185.14	8.70·10 ⁵	-1000	2.73	1.1·10 ¹³	1.3	4.91·10 ¹⁷
N ₂	95.7	0.0106	308.11	76.99	212.51	1.10·10 ⁴	-2134	1.75	5.6·10 ¹¹	1.4	4.44·10 ¹⁶
N ₂	79.0	0.0088	308.12	63.87	210.34	1.40·10 ⁴	-2045	1.79	7.8·10 ¹¹	1.4	5.89·10 ¹⁶

A.7 n-Alkane SAXS Measurements

Table 8.6: The results of the Small Angle X-ray Scattering experiments for *n*-heptane, *n*-octane, *n*-nonane, and *n*-decane are summarized. The stagnation pressure is fixed at $p_0 = 30.2$ kPa; \dot{m} is the molar flow rate, T_0 is the stagnation temperature; $\langle r \rangle$ is the mean radius; σ is the width of the distribution function; N is the particle number density; P is the polydispersity index; t_D , the thickness of the diffuse interface; ϕ_{SAXS} , the volume fraction of the condensed matter; “carrier gas” indicates which carrier gas was used, and t_{tof} is the time of flight from the nucleation position to the detection position $x = 7$ cm. For all fits a *Gaussian* distribution of particles was assumed.

\dot{m} mmol min ⁻¹	T_0 K	$\langle r \rangle$ m ⁻⁹	σ m ⁻⁹	N 10 ¹¹ cm ⁻³	$P = \sigma/\langle r \rangle$	t_D m ⁻⁹	ϕ_{SAXS}	carrier gas	t_{tof} μs
<i>n</i>-heptane									
52.09	318.15	5.5	3.00	16.7	0.55	0.2	2.50·10 ⁻⁶	Ar	16.0
52.09	318.15	5.3	3.01	18.7	0.57	0.1	2.50·10 ⁻⁶	Ar	16.0
72.55	318.15	9.8	2.20	7.5	0.22	0.1	6.30·10 ⁻⁶	Ar	27.9
72.55	318.15	10.0	2.40	7.0	0.24	0.1	6.30·10 ⁻⁶	Ar	27.9
93.61	318.15	13.0	2.90	4.1	0.22	0.1	8.10·10 ⁻⁶	Ar	37.0
93.61	318.15	12.9	2.90	4.2	0.22	0.1	8.10·10 ⁻⁶	Ar	37.0
123.25	318.15	19.0	3.50	1.9	0.18	0.1	1.20·10 ⁻⁵	Ar	46.9
123.25	318.15	19.0	3.60	1.9	0.19	0.1	1.15·10 ⁻⁵	Ar	46.9
157.18	318.15	23.0	4.20	1.3	0.18	0.1	1.45·10 ⁻⁵	Ar	55.7
157.18	318.15	23.0	4.15	1.3	0.18	0.1	1.45·10 ⁻⁵	Ar	55.7
196.60	318.15	28.0	5.00	8.4	0.18	0.1	1.65·10 ⁻⁵	Ar	63.7
196.60	318.15	28.0	5.10	8.4E	0.18	0.1	1.65·10 ⁻⁵	Ar	63.7
<i>n</i>-octane									
84.83	288.15	7.3	2.90	4.6	0.40	0.1	1.60·10 ⁻⁶	N ₂	20.4
84.83	288.15	7.6	2.75	4.1	0.36	0.1	1.60·10 ⁻⁶	N ₂	22.5
105.05	288.15	11.4	3.60	3.8	0.32	0.1	5.00·10 ⁻⁶	N ₂	43.0
105.05	288.15	11.3	3.60	3.5	0.32	0.1	4.50·10 ⁻⁶	N ₂	42.6
133.59	288.15	16.8	4.00	2.0	0.24	0.1	8.50·10 ⁻⁶	N ₂	62.6
133.59	288.15	16.8	3.90	2.1	0.23	0.1	9.00·10 ⁻⁶	N ₂	62.6
136.83	298.15	9.4	4.65	2.1	0.49	0.1	1.60·10 ⁻⁶	N ₂	13.3
136.83	298.15	9.8	4.00	2.1	0.41	0.1	1.80·10 ⁻⁶	N ₂	13.3

\dot{m} mmol min ⁻¹	T_0 K	$\langle r \rangle$ m ⁹	σ m ⁹	N 10 ¹¹ cm ⁻³	$P = \sigma/\langle r \rangle$	t_D m ⁹	ϕ_{SAXS}	carrier gas	t_{tof} μs
164.93	298.15	14.2	5.00	1.5	0.35	0.1	3.80 $\cdot 10^{-6}$	N ₂	21.2
164.93	298.15	14.5	5.00	1.4	0.34	0.1	3.80 $\cdot 10^{-6}$	N ₂	21.2
196.09	298.15	19.0	5.20	1.2	0.27	0.1	7.30 $\cdot 10^{-6}$	N ₂	28.6
196.09	298.15	19.0	5.00	1.2	0.26	0.1	7.30 $\cdot 10^{-6}$	N ₂	28.6
n-nonane									
77.97	298.15	12.0	2.70	5.3	0.23	0.1	8.30 $\cdot 10^{-6}$	N ₂	60.3
77.97	298.15	12.0	2.70	5.3	0.23	0.1	8.30 $\cdot 10^{-6}$	N ₂	60.3
69.94	308.15	7.4	3.10	6.9	0.42	0.1	2.50 $\cdot 10^{-6}$	N ₂	31.6
69.94	308.15	7.4	3.10	6.9	0.42	0.1	2.50 $\cdot 10^{-6}$	N ₂	31.6
104.71	308.15	13.5	3.30	3.5	0.24	0.1	7.80 $\cdot 10^{-6}$	N ₂	51.1
104.71	308.15	13.5	3.30	3.5	0.24	0.1	7.80 $\cdot 10^{-6}$	N ₂	51.1
124.43	308.15	17.8	4.30	2.3	0.24	0.1	1.15 $\cdot 10^{-5}$	N ₂	59.5
124.43	308.15	17.9	4.30	2.1	0.24	0.1	1.10 $\cdot 10^{-5}$	N ₂	59.5
139.09	308.15	20.0	4.20	1.9	0.21	0.1	1.40 $\cdot 10^{-5}$	N ₂	64.8
139.09	308.15	20.0	4.20	1.9	0.21	0.1	1.40 $\cdot 10^{-5}$	N ₂	64.8
169.97	308.15	23.0	4.80	1.5	0.21	0.1	1.60 $\cdot 10^{-5}$	N ₂	74.5
169.97	308.15	23.0	4.80	1.5	0.21	0.1	1.60 $\cdot 10^{-5}$	N ₂	74.5
177.76	308.15	25.3	5.20	1.3	0.21	0.1	1.85 $\cdot 10^{-5}$	N ₂	76.7
177.76	308.15	25.5	5.20	1.2	0.20	0.1	1.85 $\cdot 10^{-5}$	N ₂	76.7
198.19	308.15	28.9	5.80	1.0	0.20	0.1	2.10 $\cdot 10^{-5}$	N ₂	81.9
198.19	308.15	29.0	5.90	1.0	0.20	0.1	2.15 $\cdot 10^{-5}$	N ₂	81.9
227.74	308.15	30.2	6.10	1.0	0.20	0.1	2.50 $\cdot 10^{-5}$	N ₂	88.7
227.74	308.15	30.5	6.20	1.0	0.20	0.1	2.50 $\cdot 10^{-5}$	N ₂	88.7
41.48	328.15	5.5	2.90	26.8	0.53	0.1	4.00 $\cdot 10^{-6}$	Ar	90.8
41.48	328.15	5.5	3.00	26.8	0.55	0.1	4.00 $\cdot 10^{-6}$	Ar	90.8
59.18	328.15	10.0	2.90	11.1	0.29	0.1	1.00 $\cdot 10^{-5}$	Ar	102.3
59.18	328.15	10.0	3.00	10.4	0.30	0.1	9.30 $\cdot 10^{-6}$	Ar	102.3
n-decane									
54.29	308.15	7.6	3.20	15.2	0.42	0.2	2.80 $\cdot 10^{-6}$	N ₂	63.3
54.29	308.15	7.5	3.30	15.8	0.44	0.2	2.80 $\cdot 10^{-6}$	N ₂	63.3
67.00	308.15	10.5	2.90	9.3	0.28	0.2	4.50 $\cdot 10^{-6}$	N ₂	69.8

\dot{m} mmol min ⁻¹	T_0 K	$\langle r \rangle$ m ⁻⁹	σ m ⁻⁹	N 10 ¹¹ cm ⁻³	$P = \sigma / \langle r \rangle$	t_D m ⁻⁹	ϕ_{SAXS}	carrier gas	t_{tof} μs
71.01	308.15	11.2	2.90	8.5	0.26	0.2	5.00·10 ⁻⁶	N ₂	71.6
71.01	308.15	11.2	2.80	8.5	0.25	0.2	5.00·10 ⁻⁶	N ₂	71.6
91.04	308.15	12.7	3.00	6.5	0.24	0.2	5.60·10 ⁻⁶	N ₂	79.2
91.04	308.15	12.7	3.00	6.5	0.24	0.2	5.60·10 ⁻⁶	N ₂	79.2

References

- Allard, E. F. and J. L. Kassner, *J Chem Phys* **42** (4), 1401 (1965).
- Anisimov, M. P., P. K. Hopke, S. D. Shandakov, and I. I. Shvets, *J Chem Phys* **113** (5), 1971 (2000).
- Anisimov, M. P., J. A. Koropchak, A. G. Nasibulin, and L. V. Timoshina, *J Chem Phys* **109** (22), 10004 (1998).
- Atkins, P. W., *Physical Chemistry*, 6th edition, (Oxford University Press, Oxford, 1998).
- Becker, R. and W. Döring, *Ann. Phys.* **24**, 719 (1935).
- Biet, T., *Experimente zur homogenen Keimbildung - Nukleation und Wachstum von n-Pentanol*, Diplom-Arbeit, Universität zu Köln, 1998.
- Blanton, T. N., T. C. Huang, H. Toraya, C. R. Hubbard, S. B. Robie, D. Louer, H. E. Göbel, R. Gilles, and T. Raferty, *J. Powder Diffraction Study* **10** (2), 91 (1995).
- Brus, D., A. P. Hyvarinen, V. Zdimal, and H. Lihavainen, *J Chem Phys* **122** (21) (2005).
- Brus, D., V. Zdimal, and F. Stratmann, *J Chem Phys* **124** (16), 164306 (2006).
- edited by Lide, D. R., *Handbook of Chemistry and Physics*, 84th edition, (CRC, Boston, 2003).
- Farkas, L., *Z. Phys. Chem. (Leipzig)* **125**, 236 (1927).
- Gharibeh, M., Y. Kim, U. Dierregsweiler, B. E. Wyslouzil, D. Ghosh, and R. Strey, *J Chem Phys* **122** (9), 094512 (2005).
- Graßmann, A. and F. Peters, *J Chem Phys* **113** (16), 6774 (2000).
- Graßmann, A. and F. Peters, *J Chem Phys* **116** (17), 7617 (2002).
- Hale, B. N., *Phys. Rev. A* **33** (6), 4156 (1986).
- Hale, B. N., *Metallurgical Transactions A* **23A**, 1863 (1992).
- Heath, C. H., K. Streletzky, B. E. Wyslouzil, J. Wölk, and R. Strey, *J Chem Phys* **117** (13), 6176 (2002).

- Heath, C. H., K. A. Strelitzky, B. E. Wyslouzil, J. Wölk, and R. Strey, *J Chem Phys* **118** (12), 5465 (2003).
- Heist, R. H. and H. H. He, *J. Phys. Chem. Ref. Data* **23** (5), 781 (1994).
- Heist, R. H. and H. Reiss, *J Chem Phys* **59** (2), 665 (1973).
- Hruby, J., Y. Viisanen, and R. Strey, *J. Chem. Phys.* **104** (13), 5181 (1996).
- Huang, T. C., H. Toraya, T. N. Blanton, and Y. Wu, *Journal of Applied Crystallography* **26**, 180 (1993).
- Hung, C. H., M. J. Krasnopoler, and J. L. Katz, *J Chem Phys* **90** (3), 1856 (1989).
- Iland, K., *Experimente zur homogenen Keimbildung von Argon und Stickstoff*, Ph.D. Thesis, Universität zu Köln, 2004a.
- Iland, K., J. Wedekind, J. Wölk, P. E. Wagner, and R. Strey, *J Chem Phys* **121** (24), 12259 (2004b).
- Kacker, A. and R. H. Heist, *J Chem Phys* **82** (6), 2734 (1985).
- Katz, J. L., *J Chem Phys* **52** (9), 4733 (1970).
- Khan, A., C. H. Heath, U. M. Dieregswiler, B. E. Wyslouzil, and R. Strey, *J Chem Phys* **119** (6), 3138 (2003).
- Kim, Y. J., B. E. Wyslouzil, G. Wilemski, J. Wölk, and R. Strey, *J. Phys. Chem. A* **108** (20), 4365 (2004).
- Kotlarchyk, M. and S. H. Chen, *J Chem Phys* **79** (5), 2461 (1983).
- Laaksonen, A., V. Talanquer, and D. W. Oxtoby, *Annu. Rev. Phys. Chem.* **46**, 489 (1995).
- Lihavainen, H. and Y. Viisanen, *J. Phys. Chem. B* **105**, 11619 (2001a).
- Lihavainen, H., Y. Viisanen, and M. Kulmala, *J Chem Phys* **114** (22), 10031 (2001b).
- Looijmans, K. N. H. and M. E. H. van Dongen, *Experiments in Fluids* **23** (1), 54 (1997).
- Luijten, C. C. M., O. D. E. Baas, and M. E. H. van Dongen, *J Chem Phys* **106** (10), 4152 (1997).
- Luijtens, C. C. M., *Nucleation and droplet growth at high pressure*, Ph.D. Thesis, Technische Universiteit Eindhoven, 1998.

- Manka, A., D. Bergmann, D. Ghosh, J. Wölk, and R. Strey, presented at the 17th International Conference on Nucleation and Atmospheric Aerosols, Galway, Ireland, 2007 (unpublished).
- Megens, M., C. van Katz, M., P. Bösecke, and W. L. Vos, *Langmuir* **13** (23), 6120 (1997).
- Mortimer, R. G., *Physical Chemistry*, 2th edition, (Academic Press, San Diego, 2000).
- Muitjens, M. J. E. H., *Homogeneous condensation in a vapor/gas mixture at high pressures in an expansion cloud chamber*, Ph.D. Thesis, Technische Universiteit Eindhoven, 1996.
- Paci, P., Y. Zvinevich, S. Tanimura, B. E. Wyslouzil, M. Zahniser, J. Shorter, D. Nelson, and B. McManus, *J Chem Phys* **121** (20), 9964 (2004).
- Peters, F., *J Chem Phys* **77** (9), 4788 (1982).
- Peters, F., *Experiments in Fluids* **1** (3), 143 (1983).
- Peters, F. and B. Paikert, *J Chem Phys* **91** (9), 5672 (1989).
- Peters, P., *Nucleation and Condensation in gas-vapor mixtures of alkanes and water*, Ph.D. Thesis, Technische Universiteit Eindhoven, 2002.
- Reguera, D. and H. Reiss, *J Phys Chem B* **108** (51), 19831 (2004a).
- Reguera, D. and H. Reiss, *Phys Rev Lett* **93** (16), 165701 (2004b).
- Rudek, M. M., J. A. Fisk, V. M. Chakarov, and J. L. Katz, *J Chem Phys* **105** (11), 4707 (1996).
- Rudek, M. M., J. L. Katz, I. V. Vidensky, V. Zdímal, and J. Smolík, *J Chem Phys* **111** (8), 3623 (1999).
- Rusyniak, M. and M. S. El-Shall, *J. Phys. Chem. B* **105** (47), 11873 (2001).
- Schmeling, T. and R. Strey, *Ber. Bunsenges. Phys. Chem.* **87**, 871 (1983).
- Schmitt, J. L. and G. J. Doster, *J Chem Phys* **116** (5), 1976 (2002).
- Seifert, S., R. E. Winans, D. M. Tiede, and P. Thiyagarajan, *Journal of Applied Crystallography* **33** (1), 782 (2000).
- Shapiro, A. H., *Vol. 1: The dynamics and thermodynamics of compressible fluid flow*, (Ronald, New York, 1953).

- Smolík, J. and P. E. Wagner, in *Nucleation and Atmospheric Aerosols*, edited by P. E. Wagner (Pergamon, Oxford, 1996), pp. 58.
- Streletzky, K. A., Y. Zvinevich, B. E. Wyslouzil, and R. Strey, *J Chem Phys* **116** (10), 4058 (2002).
- Strey, R., *Microstruktur von Mikroemulsionen*, Georg-August-Universität zu Göttingen, 1992.
- Strey, R. and T. Schmeling, *Ber. Bunsenges. Phys. Chem.* **87**, 324 (1983).
- Strey, R., Y. Viisanen, and P. E. Wagner, *J Chem Phys* **103** (10), 4333 (1995).
- Strey, R., P. E. Wagner, and T. Schmeling, *J Chem Phys* **84** (4), 2325 (1986).
- Strey, R., P. E. Wagner, and Y. Viisanen, *J. Phys. Chem.* **98** (32), 7748 (1994).
- Tanimura, S., B. E. Wyslouzil, M. S. Zahniser, J. H. Shorter, D. D. Nelson, and J. B. McManus, *J Chem Phys* **127** (accepted for publication) (2007).
- Tanimura, S., Y. Zvinevich, and B. E. Wyslouzil, *J Chem Phys* **122** (19) (2005).
- Viisanen, Y. and R. Strey, *J Chem Phys* **101** (9), 7835 (1994).
- Viisanen, Y., P. E. Wagner, and R. Strey, *J Chem Phys* **108** (10), 4257 (1998).
- Volmer, M. and A. Weber, *Z. Phys. Chem. (Leipzig)* **119**, 227 (1926).
- Wagner, P. E., *J. Colloid Interface Sci.* **105**, 456 (1985).
- Wagner, P. E. and R. Strey, *J. Phys. Chem.* **85** (18), 2694 (1981).
- Wagner, P. E. and R. Strey, *J Chem Phys* **80** (10), 5266 (1984).
- Wedler, G., *Lehrbuch der Physikalischen Chemie*, 4. Auflage, (Wiley-VCH, Weinheim, 1997).
- Gasdynamics*, edited by Wegener, P. P. (Marcel Dekker, New York, 1966).
- Witte, D. W. and E. K. Tatum, *Computer Code for Determination of Thermally Perfect Gas Properties*, (National Aeronautics and Space Administration, Hampton, 1994).
- Wölk, J. and R. Strey, *J. Phys. Chem. B* **105** (47), 11683 (2001).

Wyslouzil, B. E., C. H. Heath, J. L. Cheung, and G. Wilemski, *J Chem Phys* **113** (17), 7317 (2000a).

Wyslouzil, B. E., R. Strey, and G. Wilemski, *PCCP* **accepted for publication** (2007).

Wyslouzil, B. E., G. Wilemski, M. G. Beals, and M. B. Frish, *Physics of Fluids* **6** (8), 2845 (1994).

Wyslouzil, B. E., G. Wilemski, J. L. Cheung, R. Strey, and J. Barker, *Phys. Rev. E* **60** (4), 4330 (1999).

Wyslouzil, B. E., G. Wilemski, and R. Strey, *Abstracts of Papers of the American Chemical Society* **220**, U164 (2000b).

Zdimal, V. and J. Smolik, *Atmospheric Research* **46** (3-4), 391 (1998).

Acknowledgements

First, I would like to thank Prof. Dr. Reinhard Strey for giving me the absolute freedom in my research and merely setting the fundamental boundaries. Your excellent and honest advice during discussions has catapulted my PhD thesis a number of times. I specially thank you for intensive discussions concerning the SAXS data and your ideas concerning the expansion rate. Giving me the possibility to visit the Ohio State University numerous times and welcoming me back with open arms has enriched my experience.

My sincere gratitude also goes to Prof. Dr. Barbara E. Wyslouzil, in whose laboratory I have conducted all of the experiments. Thanks for taking such good care of me each time I visited you. I have profited from your constant readiness for discussions. Thanks for coming Saturdays to the office and working with me on our future publications. These drafts were a valuable landmark for this thesis. Furthermore, thanks for not forgetting to take me to the Argonne National Laboratories. It was a great experience and essential for this work.

It is safe to recognize that without the useful discussions with Prof. Dr. Barbara E. Wyslouzil and Prof. Dr. Reinhard Strey this work would not be the least bit how it is now. Also, their trust in my presentation skills has enabled me to visit numerous conferences.

I would like to thank PD Dr. Thomas Kraska for reviewing this work and Prof. Dr. U. Ruschewitz for taking over the chairman position during my defence.

I also thank Dr. Judith Wölk without whom I would have never visited the Ohio State University. I have not only learned a lot from your scientific knowledge but have also profited from your social and soft skills.

Dr. Shinobu Tanimura has helped me a number of times during programming problems with FORTRAN. Additionally, without you it would have been a much more complicated task to imbed the temperature dependency of the constant pressure heat capacity. Finally, I must also mention the long measurement nights at Argonne National Laboratories. Thanks!

Dear Ma. Sci. Hartawan Laksmono I must thank you for the electronical support in your Lab. You have imbedded the automatic electronical acquisition of the mass flow controllers. Without this no one would have conducted any measurements at OSU. Further, thanks for the good TEAM work (Together All Achieve More) at Argonne. I wish you all the best for your remaining PhD research.

Dear Dr. Jan Wedekind, it was good to have such a clever and refreshing older “student” from whom I have definitely learned a lot of presentation skills. But also discussions with such a skeptical and calm person were a positive experience for me.

My very special thanks goes to Dirk Bergmann, my helping hand, who has helped me carry out more than 100 pressure trace measurements. Thanks for getting used to my working hours and also working over night. I am positive without your help I would have never been able to measure so many experiments. Furthermore, I must also thank you for helping me fit a number of SAXS data. I hope you also learned a lot while working with me. Good luck for your future research.

I must also thank Alex Manka and Dirk Bergmann for testing my new experimental idea of conducting only an expansion with the two valve expansion chamber.¹⁰⁸ It is unique that these experiments directly worked out to be so promising. Further, I am very proud, that all of us are going to present the work at the 17th ICNAA. I wish both of you all the best for your Diploma thesis.

Here I must also thank the mechanical workshop under the guidance of Mr. H. Metzner, especially Mr. T. Michaelis. The mechanical Workshop has repaired the the two valve chamber a number of times.

I must also thank Mr. W. Röhl for electronical support. He has renewed the entire electronical data acquisition after a computer crash.

I would also like to thank Dr. David Reguera with whom I had the chance to discuss my work several times. I have not only learned a lot concerning physics from you, but most importantly to first quietly listen and then talk. My visit in Barcelona was a good experience for this work. Furthermore, I had a great time with you and Dr. Jan Wedekind. I am already planning to visit Barcelona again, and maybe I will eat some “alien like fish” with you next time.

I must also thank Dipl. Chem. Regina Schwering for proof-reading this work. I guess it was a very hard and tiring job. Furthermore, you were also a good person to explain my research problems to, even though you only listened.

¹⁰⁸ Manka *et al.*, 2007.

Erklärung (Statement)

Ich versichere, dass ich die von mir vorgelegte Dissertation selbstständig angefertigt, die benutzten Quellen und Hilfsmittel vollständig angegeben und die Stellen der Arbeit – einschließlich Tabellen, Karten und Abbildungen – die anderen Werken im Wortlaut oder dem Sinn nach entnommen sind, in jedem Einzelfall als Entlehnung kenntlich gemacht habe; dass diese Dissertation noch keiner anderen Fakultät oder Universität zur Prüfung vorgelegen hat; dass sie – abgesehen von unten angegebenen Teilpublikationen - noch nicht veröffentlicht worden ist sowie, dass ich eine solche Veröffentlichung vor Abschluss des Promotionsverfahrens nicht vornehmen werde. Die Bestimmungen dieser Promotionsordnung sind mir bekannt. Die von mir vorgelegte Dissertation ist von Prof. Dr. Reinhard Strey betreut worden.

Köln, den 21. August 2007

David Ghosh

Teilpublikationen:

Gharibeh, M., Kim, Y., Dieregsweiler, U., Wyslouzil, U., Ghosh, D., Strey, R., „Homogeneous nucleation of *n*-propanol, *n*-butanol, and *n*-pentanol in a supersonic nozzle“, J. Chem. Phys., **122** (9), 094512, 2005.

Ghosh, D., Bergmann, D., Wölk, J., Strey, R., Tanimura, S., Wyslouzil, B. E., “Homogeneous nucleation of the homologous series of *n*-alkanes” Conference Proceedings of FEDSM2006 ASME, Joint U.S. – European Fluids Engineering Summer Meeting, Miami, FL, Order No. I750DV, ISBN 0-7918-3783-1.

Ghosh, D., Strey, R., Wyslouzil, B. E., “Using Small Angle X-ray Scattering to measure homogeneous nucleation rates of *n*-propanol in a supersonic nozzle”, Conference Proceedings of 17th International Conference on Nucleation and Atmospheric Aerosols, Edited by Colin D. O’Dowd and Paul E. Wagner, 2007 Springer Verlag, ISBN 978-1-40206474-6.

Bergmann, D., Ghosh, D., Wölk, J., Strey, R., Tanimura, S., Wyslouzil, B. E., “Homogeneous nucleation of a homologous series of *n*-alkanes in a supersonic nozzle”, Conference Proceedings of 17th International Conference on Nucleation and Atmospheric Aerosols, Edited by Colin D. O’Dowd and Paul E. Wagner, 2007 Springer Verlag, ISBN 978-1-40206474-6.

Manka, A., Bergmann, D., Ghosh, D., Wölk, J., Strey, R., „Preliminary results on homogeneous nucleation of water: A novel measurement technique using the two-valve expansion chamber“, Conference Proceedings of 17th International Conference on Nucleation and Atmospheric Aerosols, Edited by Colin D. O’Dowd and Paul E. Wagner, 2007 Springer Verlag, ISBN 978-1-40206474-6.

Lebenslauf (Curriculum vitae)

David Ghosh	name
01.08.1979	date of birth
New Delhi, India	place of birth
Single, no children	marital status

academic carrier

PhD under Prof. Strey, Institut für Physikalische Chemie, Universität zu Köln	since 01/2005
diploma thesis under Prof. Strey, Universität zu Köln “Nucleation of <i>n</i> -nonane and the heat of association in the methanol vapor phase”	04/2004 – 12/2004
diplom chemistry, Universität zu Köln	04/2000 – 04/2004

overseas research experience

Prof. Wyslouzil, Department of Chemical Engineering, Ohio State University, U.S.	04/2007
--	---------

Prof. Reguera, Departament de Física Fonamental, Universitat de Barcelona, Spain	09/2006
Argonne National Laboratories, Chicago, U.S.	11/2005 – 12/2005
Prof. Wyslouzil, The Ohio State Univer- sity, U.S.	01/1005 – 08/2005
Prof. Wyslouzil, Department of Chemi- cal Engineering, Worcester Polytechnic Institute, U.S.	07/2003 – 10/2003

school

high school, Gymnasium Köln Porz, Abitur	1997 - 2000
primary school, German School New Delhi, India	1986 - 1996

conferences

oral and poster presentation, 17 th Interna- tional Conference on Nucleation and At- mospheric Aerosols, Galway, Ireland	07/2006
---	---------

-
- | | |
|---|---------|
| oral presentation, American Society of Mechanical Engineering, Joint U.S. – European Fluids Engineering Summer Meeting, Miami, U.S. | 08/2007 |
| guest lecture, Cleveland State University, U.S. | 11/2005 |
| oral presentation, American Association for Aerosol Research, Austin, U.S. | 10/2005 |
| poster presentation, Bunsentagung, Frankfurt am Main | 05/2005 |
| authorship, American Association for Aerosol Research, Atlanta, U.S. | 10/2004 |